Modeling calcium-dependent synaptic plasticity and its role in sleep-dependent memory consolidation

Auteur : Marchal, Chloé
Promoteur(s) : Drion, Guillaume
Faculté : Faculté des Sciences appliquées
Diplôme : Master en ingénieur civil biomédical, à finalité spécialisée
Année académique : 2020-2021
URI/URL : http://hdl.handle.net/2268.2/11513

Modeling calcium-dependent synaptic plasticity and its role in sleep-dependent memory consolidation

Master thesis realized with the aim of obtaining the degree of Master in Biomedical Engineering

Chloé Marchal

Supervisor:
G. Drion

Jury members:
C. Phillips
P. Sacré
V. Seutin

Department president:
D. Ruffoni

UNIVERSITY OF LIÈGE
FACULTY OF APPLIED SCIENCES
ACADEMIC YEAR 2020 - 2021

Abstract

Synaptic plasticity refers to the changes in connection strength between two neurons. It has been shown that calcium has a great role in synaptic plasticity. Indeed, it allows, once it binds to a protein called calmodulin, the activation of cascades involved in numerous signalling pathways. The key element is that low levels of calcium concentration in the post-synaptic neuron trigger the activation of protein phosphatases in the post-synaptic neuron, leading to a decrease of the connection strength between the two neurons. On the contrary, higher levels of calcium activate protein kinases, which leads to the increase of synaptic strength.

It has been shown that a single neuron can encounter different firing rates during the sleep and the awake states. Those rhythms directly have an impact on the synaptic weight between the neurons. Moreover, recent evidence shows that spindle oscillations encountered during sleep influence the calcium levels in the post-synaptic spine that trigger synaptic plasticity changes.

There exists a large number of synaptic plasticity rules. In particular, this thesis focuses on calcium-induced synaptic plasticity. However, the little number of calcium-based models do not take into account the calcium dynamics in much detail. Indeed, to reproduce protocols and obtain results that are consistent with experimental data, a great number of simplifications are often considered.

A review of the existing calcium-based models is made in order to categorize those models in a systematic way: 'How do they implement the calcium flow into the neuron?', 'What is the equation governing synaptic plasticity depending on the calcium concentration?', *etc*.

The thesis focuses on the calcium-dependent synaptic plasticity model implemented by Graupner et al. (2016). This model has made simplifications to implement the calcium dynamics while being consistent with data obtained experimentally. The contribution of this thesis is first to integrate this abstract model into a conductance-based model which allows switching from a tonic pattern to a bursting pattern, encountered during the switch to the sleep state. This allows observing what are the consequences of this switch on the calcium-dependent synaptic plasticity.

The second main contribution of the thesis is to integrate a more detailed calcium dynamics into the abstract calcium dynamics model from Graupner et al. (2016).

The key message is the fact that integrating a detailed calcium dynamics into an abstract one represents a major challenge to tackle because of the large number of assumptions that have been made to construct this abstract model. This leads to the prospect that starting from a more physiological calcium dynamics then integrating a calcium-dependent synaptic plasticity rule to this model may be a more suitable way of doing.

Acknowledgements

This Master's thesis was my first experience as a long-term project. I would certainly not have been able to complete this work without the support and assistance from people I would like to sincerely thank.

Firstly, I would like to express my gratitude to my supervisor, Professor Guillaume Drion, for providing me with the opportunity to work on such an interesting topic. I am highly thankful for his availability and his guidance during the entire year.

I would also like to give a huge thanks to Kathleen for her wise advice throughout the year. She was always available to answer my questions and my concerns.

Thereafter, I would like to thank Caroline and Chloé. They were a great psychological support during this year, and they were always there to cheer me up.

Moreover, I am deeply grateful to my family and friends for always have supported me during this project but also all along my studies.

Finally, I would like to thank the members of the jury for taking the time to read this thesis.

Liège, June 9th, 2021

Chloé Marchal

Contents

Chapter 1

Introduction

1.1 Motivations

The brain is the most complex organ of the human body. The functional unit of the brain is the *neuron*. There are more than 80 billions neurons in the brain for a healthy person. Those cells are able to communicate with each other thanks to the transfer of action potentials. Those action potentials are generated by the exchange of ions through the neuron membrane which leads to the creation of an ionic current. The transmitted information is actually contained in the temporal pattern of those action potentials.

The connection between two neurons is called a synapse and this connection can be strengthened or weakened. This refers to *synaptic plasticity*. Recent evidence shows that Ca^{2+} ions have a great role in the induction and maintenance of synaptic plasticity. Indeed, the flow of Ca^{2+} ions into the post-synaptic neurons triggers different successive biochemical processes that can lead to a change of structural properties of the post-synaptic neuron. The main source of Ca^{2+} ions is the *N-methyl-D-aspartate* receptor, located at the membrane of the post-synaptic neuron. There exist other sources, such as *voltage-dependent calcium channels* and intracellular storage.

There exist mathematical models that implement the synaptic plasticity induced by the calcium dynamics. However, the number of models that consider the calcium dynamics in its entirety is scarce. Indeed, for now, in most of the calcium-induced synaptic plasticity models, lots of assumptions have been made.

This thesis gathers the main calcium-based models that can be found in the literature. Then, it investigates how it is possible to integrate a full calcium dynamics into a simplified one and presents the challenges that are encountered when doing so.

1.2 Structure

This thesis is divided into three main parts.

Part I introduces the biological background needed to understand how to model synaptic plasticity induced by calcium concentration elevation in the post-synaptic neuron.

Firstly, the thesis begins with a general description of the neuron, the plasma membrane and its modeling thanks to the Huxley-Hodgkin model. This model represents the basics of the conductance-based models of the neuron.

Secondly, the thesis explains what happens during sleep, in particular at the level of a single neuron. Indeed, during sleep, the firing mode of the neurons changes. Moreover, the neurons become synchronized to exchange information in a more efficient way.

Thirdly, the phenomenon of synaptic plasticity is explained in details, especially the role of calcium (Section 4.3). Indeed, it has a huge role in synaptic plasticity since it allows the triggering of protein kinases and/or phosphatases, depending on its concentration level in the post-synaptic spine.

Part II focuses on the calcium-based synaptic plasticity modeling.

On the one hand, different calcium-based models are described in details (see Chapter 5). All of them consider that potentiation, *i.e.* an increase in the synaptic strength, occurs when the Ca^{2+} levels are high. For intermediate Ca^{2+} concentration elevation, it is considered that there is depression, *i.e.* a decrease in the synaptic weight.

On the other hand, the model from Graupner et al. (2016) is adapted to take into account the physiological aspects of the synaptic plasticity due to calcium concentration transients in the post-synaptic spine (see Chapter 6).

Part III summarizes the different steps of the methodology followed in this thesis and draws conclusions about the challenges to integrate a detailed biophysical calcium dynamics into a simple and abstract plasticity model. It also presents some possible paths to follow to tackle those challenges.

Part I

Background

Chapter 2

Elements of neurophysiology and neuronal modeling

2.1 The neuron

A neuron is an excitable cell that constitutes the functional unit of the nervous system. Excitability refers to the ability of a cell to respond to stimuli thanks to the generation of electrical signals, called *action potentials*.

The Figure 2.1.A presents the typical structure of the neuron. A neuron is divided into 3 parts (Vandewalle and Leprince, 2019):

- The cellular body, also called the *perikaryon* or the *soma*, which contains the nucleus, the cytoplasm and cytoplasmic organelles;

- A certain amount of dendrites originating from the cell body. Since the dendrites can extend for hundreds of μm and branch multiple times, it is possible to use the term *dendritic tree* to define the widespread dendritic arborization;

- A unique axon that originates from the soma and can extend for long distances. The axon is terminated by a set of synapses.

The connection between two neurons is called a *synapse*. The neuron transmitting the signal is the pre-synaptic neuron and the one receiving the signal is the post-synaptic neuron.

Neurons are responsible for the signal processing of the information. The signal coming from other neurons is collected in the dendrites of the post-synaptic neuron and is integrated into its soma. An action potential, also called a spike, is generated in the soma to be propagated through the axon. Once this electrical signal arrives at the synapses, it can either be directly transmitted to the neurons which synapses are connected (for an electrical synapse) or trigger the release of neurotransmitters contained in synaptic vesicles that will be transmitted to the neighbouring neurons (chemical synapse). There exist different types of neurons, each type releases and is sensitive to certain types of neurotransmitters.(Geris and Dauby, 2019)

The transmission of action potentials allows the information transmission between neurons. The information is actually contained in the firing pattern of those action potentials. The general shape of an action potential is presented in Figure 2.1.B and a detailed explanation about the generation of action potentials is given in the Appendix section (see A.1).

Neurotransmitters A neurotransmitter is released by the pre-synaptic neuron and acts as a ligand to specific receptors located on the membrane of the post-synaptic neuron. Depending on the type of receptor and the type of the post-synaptic neuron, the effects of the neurotransmitter will be different. There exist different types of neurotransmitters: acetylcholine, serotonin, dopamine, glutamate, histamine, GABA, *etc.* The type of neurotransmitters released by the neuron defines the neuron itself. For example, a neuron that produces and releases dopamine is called a dopaminergic neuron. However,
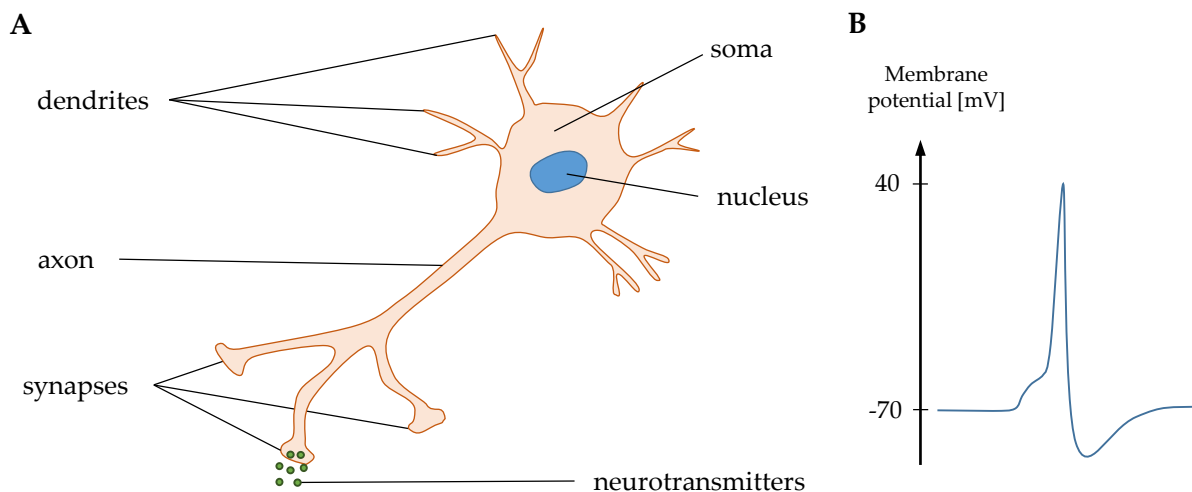
Figure 2.1 – A. The general structure of the neuron. It is composed of the soma, *i.e.* the body cell, the nucleus, dendrites (also called dendritic processes) and synapses. From the synapses, the neuron can release neurotransmitters to transmit an electrical signal to other neurons. **B.** General shape of an action potential (AP). The resting membrane potential is equal to $\simeq -70mV$ and the maximum membrane potential attained during the AP is $\simeq 40mV$. The information between neurons is transmitted thanks to those APs. Adapted from (Coutisse, 2018)

a neuron rarely has only one type of neurotransmitters. It is for example possible that a neuron releases one different neurotransmitter at each synapse.

The neurotransmitter binds to the specific receptor located at the membrane of the post-synaptic neuron. This bounding induces conformational changes that allow the opening of the channel, leading to the ions flow inside/outside the cell. For example, in the peripherical nervous system, acetylcholine is released in the neuro-muscular junction when a nerve impulse arrives at a motor neuron. Acetylcholine then binds to a receptor at the membrane of the muscle fibre (*i.e.* the post-synaptic neuron). This binding allows the K^+ ions to enter in the post-synaptic neuron, causing a muscle contraction (Bear Mark (2007), Berry (2019)).

It is important to know that the neurotransmitters are not produced in the axon but in the synapses. The neurotransmitters are stored in synaptic vesicles that are constantly recycled and/or refilled with new neurotransmitters. The neurotransmitters are contained in the synaptic vesicles with a certain quantum, *i.e.* a fixed quantity of neurotransmitters per vesicle. When there is no action potential, it is possible to have a spontaneous release of neurotransmitters and this explains why it is possible to observe a certain noise of the membrane potential. When there is at least one action potential, the speed of release of neurotransmitters increases and there is a simultaneous release of tens of neurotransmitters quanta (Vandewalle and Leprince, 2019).

Neurotransmitters activity is sometimes controlled by *neuromodulation*. Neuromodulators are a subset of neurotransmitters that can act together with neurotransmitters to enhance receptor responses. Unlike neurotransmitters, neuromodulation does not necessarily carry the signal of inhibition or excitation from one neuron to the other. Neuromodulation rather changes the properties of synaptic receptors or synapses themselves and the neuronal transmission is modified (Khetrapal, 2021).

2.2 The plasma membrane

2.2.1 Physiology of the plasma membrane

The cell membrane allows the separation of the inside of the cell (*i.e.* the cytoplasm) and the extracellular environment. A simple schema of the plasma membrane structure is presented in Figure 2.2. This plasma membrane is composed of lipids, proteins and sugars. The phospholipids are arranged in a double layer, which makes the membrane impermeable. Only non-polar small molecules can pass

through the membrane. Proteins are embedded between the phospholipid layers and are selectively permeable to specific ions and larger molecules.
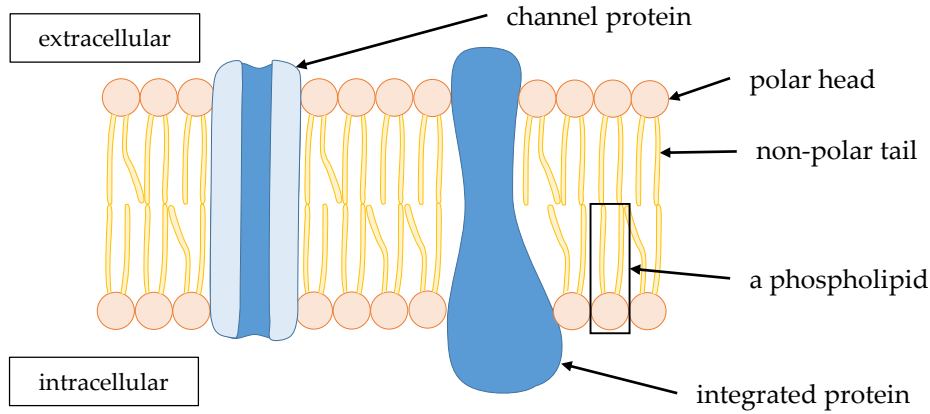
Figure 2.2 – Schema of a bilayer of phospholipids with proteins embedded in it. A phospholipid has a polar head and a non-polar tail, which makes the membrane impermeable to ions and charged molecules. The ions, charged and big molecules can pass through the membrane only thanks to the protein channels. Adapted from (Geris and Dauby, 2019)

The electrical mechanism of the cell is based on the transfer and storage of charges, carried by ions, such as sodium (Na^+), potassium (K^+), chlorine (Cl^-) and calcium (Ca^{2+}) ions. Since the phospholipids are arranged such that the membrane is impermeable, the ions cannot go through it and have to pass through the membrane proteins. Those proteins can provide a passive transfer (*i.e.* ion channels) or an active transfer (*i.e.* active transporters). Ion channels are membrane proteins that, depending on their electro-chemical gradient, can let ions pass through it passively. Those ion channels define the permeability of the cell membrane that allows the regulation of ions flow into the cell.

Active transporters need energy for the transfer of ions and/or molecules. Indeed, unlike ion channels which let the ions pass according to their electro-chemical gradient, the ions and/or the molecules are transferred against their electro-chemical gradient so it is needed to provide energy to such transporters. The needed chemical energy is in the form of ATP.

Because of this distribution of ions around the cell but also the fact that the membrane is selectively permeable to ions, there exists a difference of potential between the inside and the outside of the cell, called *membrane potential V_m*, *i.e.* $V_m = V_{in} - V_{out}$. The signal transmission between neurons is due to action potential propagation. Those action potentials are due to sudden changes in V_m, which are themselves due to the channels permeability variation. For more details about how an action potential is generated, see Section A.1.

For each ionic channel, it is possible to define a *reversal potential*, also called the *Nernst potential*. It corresponds to the membrane potential at which there is no ion flow. In other words, it is the membrane potential at which the voltage driving force counterbalances exactly the chemical driving force which is due to the asymmetric concentration distribution of the ion. This reversal potential is given by Nernst's law:

$$V_{Nernst} = \frac{RT}{zF} \ln \frac{[ion]_{out}}{[ion]_{in}} \tag{2.1}$$

Where R is the gas constant, T the temperature in Kelvin, F the Faraday's law and finally z the ion valence.

The resting membrane potential is equal to -70 mV and is defined by the relative ionic concentrations and permeability of the corresponding ionic channels at equilibrium:

$$V_m = \frac{RT}{F} \ln \left(\frac{P_{Na^+} [Na^+]_{out} + P_{K^+} [K^+]_{out} + P_{Cl^-} [Cl^-]_{in}}{P_{Na^+} [Na^+]_{in} + P_{K^+} [K^+]_{in} + P_{Cl^-} [Cl^-]_{out}} \right) \tag{2.2}$$

The equation (2.2) is defined from Nernst's equation and is called the *Goldman-Hodgkin-Katz* (GHK) equation. The ionic concentrations of the ions Na^+, K^+ and Cl^- with their reversal potential are given in Table A.1.

2.2.2 Electrical Model

It is possible to use an electrical model to represent the cell membrane. We can first consider that since the bilayer of phospholipids is impermeable to ions, it only allows the accumulation of charges inside and/or inside the cell. We can summarize this electrical behaviour of the membrane capacitance by a constant capacity C_m. This way, changes in the distribution of the ions across the membrane capacitance can be considered as a capacitive current I_C:

$$I_C = C_m \frac{dV_m}{dt} \tag{2.3}$$

Secondly, we can consider that each ion channel is selective for only one ion at a time. If we consider a given amount of open ion channels for a given ion i, we can describe this electrical behaviour as a variable conductance g_i for each ion i. This way, for each ion, it is possible to define an ionic current $I_{ion,i}$. Following Ohm's law, $I_{ion,i}$ can be defined as:

$$I_{ion,i} = g_i(V_m - V_{ion,i}) \tag{2.4}$$

Where $V_{ion,i}$ is the reversal potential of the ion i (also called the *Nernst* potential, *i.e.* the membrane potential at which there is no flow of the ion. $(V_m - V_{ion,i})$ represents the fact that more V_m is far from $V_{ion,i}$, more the electrochemical force will be strong and the ionic current $I_{ion,i}$ will thus be high.

This way, as can be seen in Figure 2.3, the cell membrane can be represented as a simple RC circuit, with a capacitance C_m and a variable conductance g_{ion}. By the application of Kirchhoff's law, we get

$$C_m \dot{V}_m = -\sum_{i=1}^{n} g_i (V_m - V_{ion,i}) + I_{app} \tag{2.5}$$

Where $\dot{V}_m$ is the variation of membrane potential per unit of time and I_{app} is the applied current representing the external stimulations.
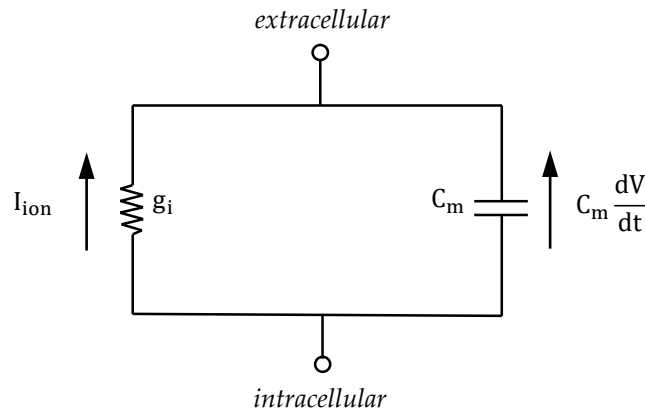
Figure 2.3 – The cell membrane can be modeled by a simple electrical model. The accumulation of charges inside/outside the cell resulting from the fact that the membrane is not permeable is equivalent to a capacity C_m. The changes on the ionic concentration distributions accross the membrane can be represented by a current I_{ion} (Geris and Dauby, 2019).

2.2.3 Hodgkin-Huxley model

Alan Lloyd Hodgkin and Andrew Fielding Huxley were the first ones to describe mathematically the membrane potential behaviour of an excitable cell. They conducted experiments on the axons of a

giant squid because those are large excitable cells. They observed that two specific ions allow the generation of action potentials: sodium (Na^+) and potassium (K^+) ions. The membrane of the giant squid axon can thus be represented with the electrical model presented in Figure 2.4.
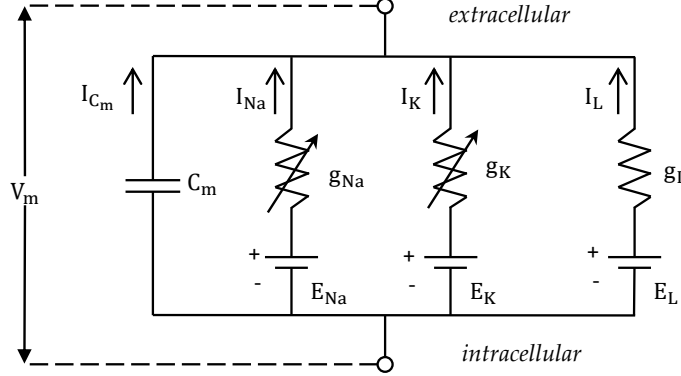
Figure 2.4 – Electrical model of the axon membrane of the giant squid. This model takes into account the ions K^+ and Na^+ that are necessary to generate an action potential. The g_l conductance takes into account non specific leak currents, *e.g.* from recording electrodes (Geris and Dauby, 2019).

Based on this simplified model, it is possible to write the circuit equation from the Kirchhoff's law ($\sum i = 0$):

$$C_m \frac{dV_m}{dt} = -I_{Na} - I_K - I_L + Iapp \tag{2.6}$$

Taking into account the equation (2.5), we can rewrite (2.6) as:

$$C_m \frac{dV_m}{dt} = g_{Na}(V_m - V_{Na}) - g_K(V_m - V_K) - g_L(V_m - V_L) + I_{app} \tag{2.7}$$

Hodgkin and Huxley experimentally observed that the conductance values g_{Na} and g_K were time and voltage-dependent.

The complete Hodgkin and Huxley model is given by:

$$
\begin{aligned}
C_m \dot{V}_m &= -\bar{g}_{Na} m^3 h \left(V_m - V_{Na}\right) - \bar{g}_K n^4 \left(V_m - V_K\right) - I_{leak} + I_{app} \\
\tau_m \dot{m} &= -\left(m - m_\infty\right) \\
\tau_h \dot{h} &= -\left(h - h_\infty\right) \\
\tau_n \dot{n} &= -\left(n - n_\infty\right)
\end{aligned}
\tag{2.8}
$$

Where $I_{leak} = g_{leak}(V_m - V_{leak})$, $m(V_m, t)$ and $h(V_m, t)$ are the sodium activation and inactivation variables for the sodium and $n(V_m, t)$ is the activation variable of the potassium. During the membrane depolarization, $m(V_m, t)$ is activated while $h(V_m, t)$ is inactivated. The detailed method to compute the differential equations from eq. (2.8) is presented in Section A.3.

This model given in eq. (2.8) can be extended with other ionic currents, *e.g* the Ca^{2+} current which allows adding a calcium dynamics to the model to get some bursting patterns. This complete model gives the basics of the conductance-based models that will be explained later (Geris and Dauby, 2019).

A simple example of a simulation of the Huxley-Hodgkin (HH) model is presented in Figure 2.5. It shows the response of the HH model to a step current I_{app}. On the bottom graph, one can observe that the $m(t)$ variable (*i.e.* the sodium activation variable) increases rapidly where the membrane becomes depolarized. In contrast, the sodium inactivation variable, $h(t)$ decreases (with a slower time scale) when the membrane is depolarized. With a similar time scale as $h(t)$, the potassium activation variable, $n(t)$, increases with depolarization and decreases once the membrane becomes hyperpolarized.

9
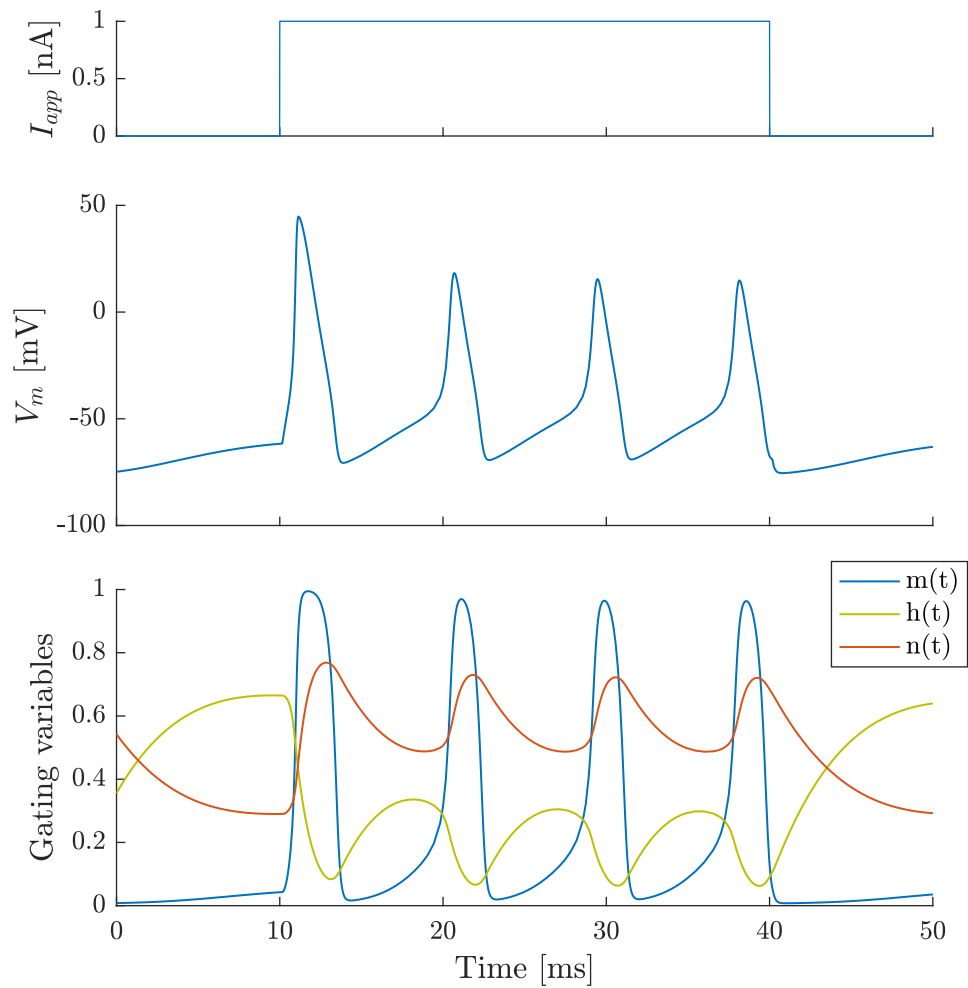
Figure 2.5 – Temporal simulation of the Huxley-Hodgkin model: evolution of the membrane potential (middle) and the gating variables (bottom). A depolarizing current is applied between 10 and 40 ms (top).

Chapter 3

Sleep and state switches

Motivation: link between sleep and memory

Sleep is a behavioural state in which consciousness is decreased, sensory activity is relatively inhibited and muscle activity is reduced. It is also accompanied by reduced responsiveness to external stimuli and happens at regular intervals and is controlled homeostatically, *i.e.* a sleep deprivation will necessarily be followed by a prolonged period of sleep. (Golbert et al., 2017)

Prolonged deprivation of sleep is dangerous for humans, it can lead to impairment of memory and cognitive capacities, and in the worst case to mood swings and hallucinations (Vandewalle and Leprince, 2019).

Recent studies have described sleep as a brain state which optimizes memory consolidation, in contrast to the awake state which optimizes memory encoding. Moreover, recent studies have shown that spindles, which are a particular component of sleep characterized by brief episodes of waxing-and-waning field potential with a frequency range of 9–15 Hz, have several important roles in sleep quality, learning and memory. One important role of those spindles is linked with neuronal development. Indeed, sleep spindles have been observed in babies' brains from 24 weeks of gestation, which indicates that spindle activity may be a factor supporting neuronal development (Astori et al., 2013). Sleep quality is also believed to be supported by spindles since those allow raising the stimulation threshold: studies have shown that during non-REM sleep, people need stronger acoustic perturbations to be awakened, especially during spindle activity (Yamadori, 1971).

3.1 Different rhythms and states of the brain during sleep

The activity of a region of the brain can be recorded thanks to an *electroencephalogram* (EEG). EEG cannot record the activity of a single neuron but it allows the recording of the activity of a set of neurons in the thalamus and/or the cortex. This EEG signal allows defining the different rhythms of the brain activity encountered during sleep (Vandewalle and Leprince, 2019).

It is important to understand that those variations in the rhythms are due to the change in the firing pattern of the action potentials delivered by the neurons themselves. Indeed, the neurons change their firing pattern depending on the brain state. To zoom to the level of a single neuron and record its activity, it is needed to conduct intracellular and extracellular recordings. The Figure 3.1 shows the firing patterns of a *single lateral geniculate neuron* (LGN) and the resulting signal observed in an EEG.

As depicted in Figure 3.1, the low amplitude and high-frequency signal that is observed in the EEG during the awake state is actually due to a tonic firing of the thalamocortical neurons. We have a train of action potentials. During this firing mode, the neurons transmit information to the cortex that is correlated with the spike trains that encode external stimuli. During the non-REM sleep state, the EEG shows an oscillatory behaviour, *i.e.* characterized by high amplitude and low-frequency signal. This signal is due to a synchronization of the neurons exhibiting a **burst** of action potentials followed by silence from all the neurons (McCormick and Bal, 1997).
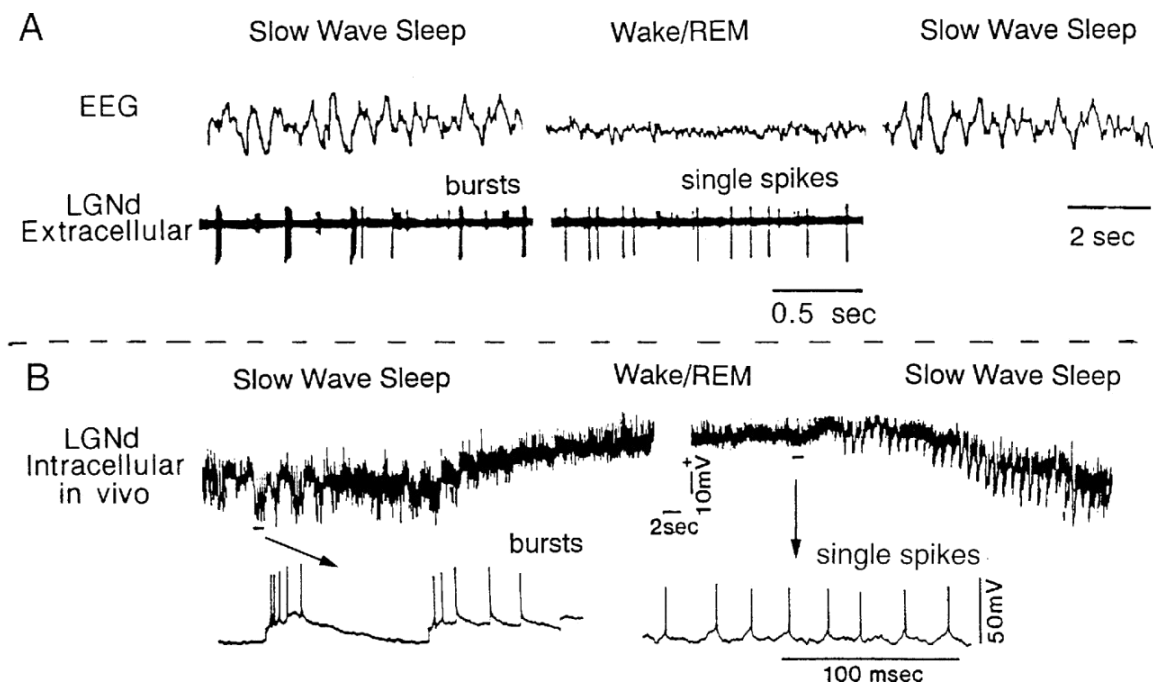
Figure 3.1 – Comparison between the EEG signal for a group of lateral geniculate relay neurons (LGN) and the signal at the level of a single neuron and comparison of activity between the awake state and the asleep state. **A.** During the slow-wave sleep, the neurons encounter a bursting pattern, which results in a slow wave in the EEG signal. In awake sleep, the neurons are firing single spikes, which results in low amplitude, high-frequency signal. **B.** Intracellular recordings in vivo during these awake/asleep states transitions. Those indicate that they are due to a depolarization of the membrane by 10–20 mV (McCormick and Bal, 1997).

Sleep is divided into two main parts: REM sleep (*Rapid Eye Movement*) and non-REM sleep. REM sleep refers to a state of the brain in which there is no muscle activity at all but brain activity is the same as the awake state (Vandewalle and Leprince, 2019).

During non-REM sleep, there exist different rhythms of brain activity that can be observed on an EEG.

Indeed, thanks to EEG, it is possible to detect the different rhythms corresponding to the different states of the brain: from the awake state to the sleep state, it is possible to observe a progressive change from a low amplitude and high-frequency signal to high amplitude and low-frequency signal. The different stages and the corresponding EEG rhythms can be seen in Figure 3.2.

The different sleep stages are:

- **Stage I** refers to the state in which people feel "drowsy". It is possible to observe on the EEG that the signal amplitude increases slightly while the frequency decreases.

- **Stage II** of sleep refers to the state of light sleep, where the frequency continues to decrease while the amplitude increases. In this signal are embedded sleep spindles, which are periodic bursts of activity (with a higher frequency of 10-12Hz).

- **Stage III** is a state of moderate deep sleep, where the EEG signal amplitude continues to increase and the frequency to decrease while sleep spindles are gradually disappearing.

- **Stage IV** represents the slow-wave sleep (SWS), with a very low frequency (0.5-2Hz). It is called deep sleep because it is the state for which it is the most difficult to awaken people.

Those four stages refer to the non-REM sleep. REM-sleep is also the stage in which dreams occur. As can be seen in Figure 3.2, the stage of REM-sleep has an EEG signal which is similar to what is observed during the awake state.
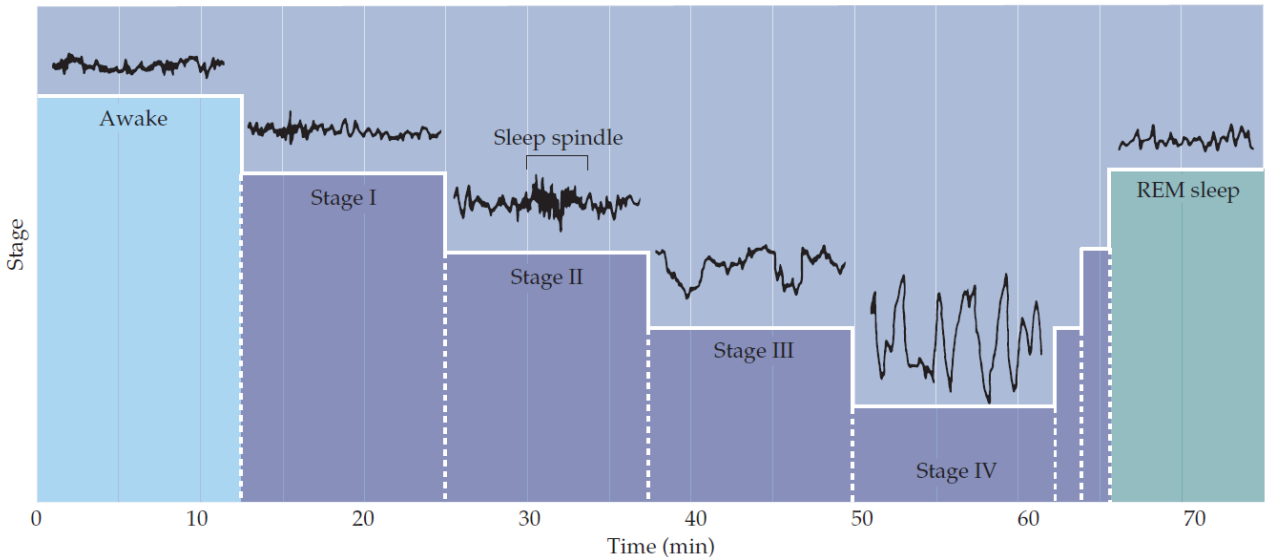
Figure 3.2 – Sleep stages. Transition from the awake state to deep sleep stage (stage IV) is characterized by a frequency decrease and an amplitude increase of the EEG signal. The EEG signal during the REM-sleep is similar to the awake state. (Bear Mark, 2007)

3.2 Switch

3.2.1 Role of the thalamus for the switch

The thalamus is an important structure of the brain. It is situated in the middle of the brain. It is a cluster of nuclei and it has a bilateral structure, *i.e.* it has a nuclei cluster in each hemisphere of the brain. It has a role of information relay with the neocortex, which is a part of the cortex implied in higher-order brain functions such as sensory perception, cognition, generation of motor commands, spatial reasoning, language, *etc.* Indeed, this part of the brain is responsible for the information relay from sensory inputs (except for olfaction) to the cortex. The thalamus thus receives the information from external inputs and sends them to the cortex. The thalamus is constituted of different nuclei, which contains the relay neurons between the thalamus and the cortex. Each nucleus of the thalamus is related to different sensory pathways. For example, the anterior nuclei receive information from the limbic system, which gives to those nuclei functions and influence upon emotional states, such as attention, alertness and memory acquisition. The relay neurons between the thalamus and the cortex can either be excitatory or inhibitory. However, only the reticular nucleus contains inhibitory neurons. All the other nuclei contain excitatory neurons. (Sendic, 2021)

Thalamus is also responsible for the switch between the awake and asleep states. It contains a nucleus called the reticular nucleus implied in the switch from the awake to the sleeping state. This nucleus contains only inhibitory neurons. It is also the only thalamic nucleus that does not project to the cortex, it can only receive inputs from it. This thalamic nucleus is also different from the other ones since it surrounds the other nuclei. During the switch, the reticular nucleus is activated by acetylcholine coming from cholinergic neurons contained in the brainstem and the cortex, more precisely in the pons-midbrain junction. This region from the brain stem is called the *reticular activating system* since it allows activating the reticular nuclei. After the activation of the inhibitory neurons from those reticular nuclei, they allow the inhibition of thalamocortical neurons. Those thalamocortical neurons are depolarized, which allow them to encounter a bursting pattern and this results in a slow wave signal in the EEG. Those excitatory/inhibitory interactions form a thalamocortical feedback loop, shown in Figure 3.3 (Bear Mark (2007), Steriade et al. (1993)).

During the switch to the awake state, the reticular nucleus is progressively inhibited by the ventrolateral preoptic nucleus (*VLPO*) of the hypothalamus. Since this reticular nucleus inhibits thalamocortical neuron activity, this activity is not inhibited anymore. Those neurons thus retrieve a tonic

firing pattern. It is then possible to observe a switch from a slow-wave signal to a low amplitude and high-frequency signal on the EEG (Vandewalle and Leprince, 2019).
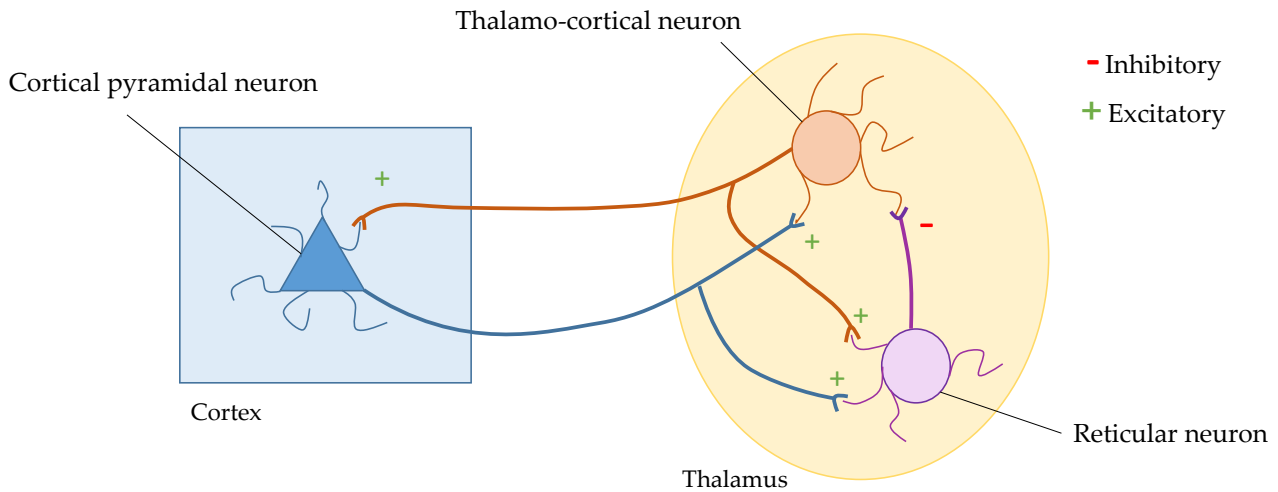
Figure 3.3 – Thalamo-cortical feedback loop. The diagram shows the interconnection between the pyramidal neurons from the cortex, the reticular neurons from the thalamus and the thalamo-cortical neurons. The reticular neurons are inhibitory. Adapted from Bear Mark (2007).

Endogenous bursting It has been shown that there exists an additional ionic current, called *T-type calcium current*, which allows thalamocortical neurons to encounter a bursting fire pattern. This calcium current is also called low-threshold (because the thalamocortical neuron has to be hyperpolarized) or transient calcium current and is often identified in the literature as I_T or I_{CaT}. This Ca^{2+} current is activated around -65 mV and inactivated after several tens of milliseconds. During this activation, a burst of action potentials (with Na^+ and K^+ ions) occurs (McCormick and Bal (1997), Coutisse (2018), Leresche and Lambert (2017)).

For more details about how this current allows the generation of a burst of action potentials, see Section A.4.

Even if the intrinsic bursting capability has been shown for thalamic neurons, there still exists no consensus in the literature about the fact that the pyramidal neurons from the cortex also have those T-type ionic channels. However, according to Franceschetti et al. (1995), the cortical neurons have this intrinsic bursting capability thanks to other currents than the T-type calcium current.

According to experimental data, those currents concern the persistent sodium current, $I_{Na(p)}$ (Fleidervish et al., 1996), the depolarization activated potassium current, I_{DK} and the calcium-activated potassium current, I_{KCa} which seems to be present in inhibitory neurons (Destexhe et al., 1996). For example, I_{KCa} participates in the switch to the bursting mode of the neuron thanks to the flow of K^+ ions into the cell, increasing its membrane potential and thus allowing the generation of a burst of APs.

Similar to T-type calcium channels, there exists other voltage-gated calcium channels (VGCCs) implied in neuronal functions. Those are the L-, N-, P-/Q- and R-type calcium channels. The main difference with the T-type channel is the fact that those VGCCs are high voltage-activated channels, *i.e.* activated with a strong depolarization (Lipscombe et al. (2004), Helton et al. (2005), Triggle (2006)).

Chapter 4

Synaptic plasticity

Synaptic plasticity refers to the activity-dependent modifications of the strength or the efficacy of synaptic transmission at preexisting synapses. Synaptic plasticity has a key role in memory encoding and consolidation. An impairment in the synaptic plasticity functioning can cause serious neuropsychiatric disorders (Heidelberger et al., 2014).

Synaptic strength can be measured by different parameters. It can be measured by

- The amplitude of the *Excitatory PostSynaptic Potential* (EPSP) of the post-synaptic neuron;

- The probability of neurotransmitters release;

- The number of synapses;

- The number of receptors recruited at the membrane of the post-synaptic neuron. Those receptors are *amino-3-hydroxy-5-methyl-4-isoxazolepropionic acid* (AMPA) receptors.

There exist two main types of synaptic plasticity: potentiation, also called facilitation, *i.e.* an increase in the synaptic strength, and depression, *i.e.* decrease in the synaptic strength.

Synaptic plasticity can have different time scales and this will affect differently the strength of the synapse. Short-term synaptic plasticity lasts for milliseconds to several minutes while long-term synaptic plasticity refers to changes in the synaptic strength that last for at least 90 minutes and can last for a lifetime. A summary of the different synaptic plasticity time scales and the resulting changes is presented in Figure 4.1.

4.1   Short-term synaptic plasticity

Short-term plasticity has crucial roles in short-term adaptations to sensory inputs, transient changes in behavioural states, and short-lasting forms of memory (Heidelberger et al., 2014).

In this case, an increase of the synaptic strength is due to an accumulation of calcium in the pre-synaptic neuron resulting from a train of action potentials in this pre-synaptic neuron. Indeed, if the action potentials are temporally close to each other, the calcium released from the first one does not have the time to leave the synaptic spine. The calcium from the first action potential contributes to the accumulation of calcium added with the second action potential. This increase of pre-synaptic calcium concentration induces biochemical changes that trigger changes in the probabilities of neurotransmitter release in the synaptic space (Vandewalle and Leprince, 2019).

A short-term depression often follows short-term facilitation. Indeed, the short-term facilitation allows increasing the release of the neurotransmitters from the vesicles contained in the pre-synaptic neuron. This pool of available neurotransmitter vesicles is progressively depleted as the pre-synaptic neuron is firing (Golbert et al., 2017).

The main function of short-term synaptic plasticity is the filtering of information transferred between neurons. Indeed, a synapse with a low probability of neurotransmitter release will play the role of a high-pass filter since this synapse will only facilitate the information transfer if the frequency
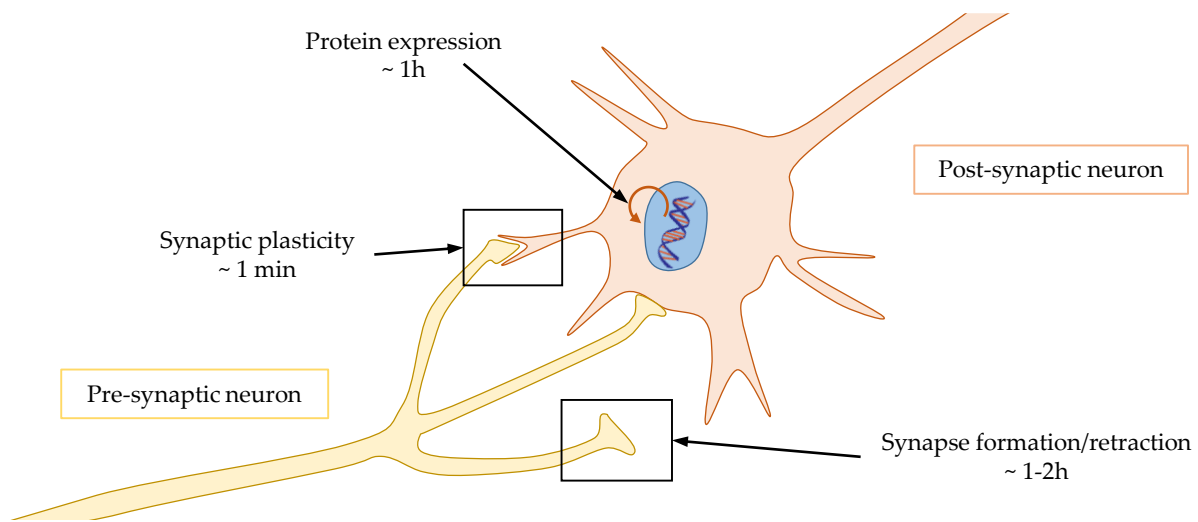
Figure 4.1 – Schematic of the different synaptic plasticity time scales. For a small time scale (ms - min), synaptic plasticity induces changes in the probability of neurotransmitters release. At a larger time scale (minutes to hours), synaptic plasticity induces changes in the structure of the synapse for the pre-synaptic neuron: creation of new synapses, expansion/retraction of existing synapses, *etc.* It also induces changes in the structure of the dendritic spine, the number of receptors at the membrane of the post-synaptic neuron (via the expression of proteins or the intracellular release of AMPARs), *etc.* Adapted from (Graupner, 2020)

of action potentials is high. In the same way, a synapse with a high probability of neurotransmitter release will act as a low-pass filter, *i.e.* the information can be easily transmitted (Bear Mark, 2007).

4.2   Long-term synaptic plasticity

Long-term synaptic plasticity has prolonged effects on the synaptic strength and the effects themselves are also different from short-term plasticity.

Long-term potentiation (LTP) refers to a long-lasting augmentation in the synaptic strength. It is possible to distinguish two types of LTP, depending on the time scale of the synaptic strength increasing. On the one hand, there is the 'early' LTP (E-LTP), which lasts for about 90 minutes, in which the modifications of the synaptic strength induce a change in the receptors efficacy (*i.e.* the channel conductance). On the other hand, there is the 'late' LTP (L-LTP), which effects can last for a lifetime and can induce changes in the structure of the synapse (number and trafficking of receptors, creation of new synapses, *etc.*) thanks to an expression of genes that leads to *de novo* protein production. This way, the synaptic strength can be assessed by the number of receptors at the membrane of the post-synaptic neuron. (Vandewalle and Leprince, 2019)

However, Makino H. (2009) suggested that the increase in the number of *a-amino-3-hydroxy-5-methyl-4-isoxazolepropionic acid* (AMPA) receptors at the post-synaptic membrane can be done via their release via an intracellular pool of synaptic vesicles containing those AMPARs. He suggested that during LTP, the vesicles release the AMPARs contained in those (by exocytosis) in order to have a certain quantity of intracellular AMPARs ready to be diffused to the dendritic surface. In other words, the release of AMPARs from intracellular vesicles does not directly contribute to LTP but it is possible that the AMPARs that incorporate onto the dendritic surface originate from this release. This way, the production of new proteins is not necessarily needed to have an increased number of AMPARs at the post-synaptic membrane.

Long-term depression refers to the decrease of the synaptic strength in the long term. It allows counterbalancing the effects of LTP but it has also a great role in learning and encoding. For example, the cerebellum, which has a major role in motor control, contains lots of inhibitory synapses so the

inhibition of those connections because of LTD leads to activation of the neurons that were connected to those inhibitory synapses (Vandewalle and Leprince, 2019).

Long-term synaptic plasticity is induced by calcium influx that originates from the activation of *N-methyl-D-aspartate* (NMDA) receptors. This Ca^{2+} influx triggers different mechanisms that imply kinases and phosphatases. This will be explained in the next section.

4.3 Role of the calcium in synaptic plasticity

As introduced in Section 4.2, the Ca^{2+} ions have a great role in the LTP/LTD induction. Those ions enter into the post-synaptic neuron by channels located on the membrane. Once they have entered the neuron, they have the ability to trigger different biochemical pathways to induce LTP/LTD (Vandewalle and Leprince, 2019).

Calcium ions enter the post-synaptic neuron thanks to NMDARs and only those receptors are permeable to Ca^{2+} ions. Those are often colocalized on the post-synaptic neuron membrane with AMPARs (cf. Figure 4.2.A). Those two types of receptors are glutamate receptors, meaning that they need the binding of glutamate to trigger their activation. In addition to this glutamate binding to be activated, NMDARs have a Mg^{2+} blockage that can be removed only if the neuron membrane is sufficiently depolarized. Once this blockade is removed, ions (Ca^{2+}, Na^+, K^+) can pass through it and enter the post-synaptic neuron (cf. Figure 4.2.B).

NMDARs and AMPARs activities are often linked. AMPARs are permeable to monovalent cations, *i.e.* Na^+ and K^+ ions. When glutamate binds to those receptors, they get activated and there is thus an ionic influx into the post-synaptic neuron, leading to a progressive depolarization of the membrane. Once there is enough depolarization of the post-synaptic membrane thanks to the Na^+ influx, the blockade of Mg^{2+} on NMDARs is removed and Ca^{2+} can now enter into the post-synaptic neuron (Golbert et al., 2017).

NMDARs are often considered as the unique source of calcium but there exist other sources, such as *voltage-dependent calcium channels* (VDCCs), also called *voltage-gated calcium channels* (VGCCs), and intracellular storage. Ca^{2+} ions can indeed enter into the post-synaptic neuron by VDCCs, those channels are open if the membrane potential exceeds a certain value. In the literature, VDCCs are sometimes abbreviated as Ca_V.

NMDARs are also considered as a *coincidence detector* between the pre- and post-synaptic spikes. Indeed, the NMDARs are activated only if the pre-synaptic stimulation is followed by a post-synaptic spike. In this case, the pre-synaptic stimulation allows the binding of glutamate to the NMDARs and the post-synaptic spike allows the removal of the Mg^{2+} blockade from the receptors, leading to synaptic plasticity. On the contrary, if there is only a pre-synaptic spike, the Mg^{2+} blockage is not removed. If there is only a post-synaptic spike, glutamate is not bound to the NMDARs and they thus remain inactivated (Graupner, 2020).

A drawing summarizing the different steps of the LTP induction and the ways this LTP can be expressed is presented in Figure 4.2.

Signaling pathways triggered by calcium influx

Once calcium gets inside the post-synaptic neuron thanks to NMDARs, it can trigger different signalling pathways, depending on the calcium level in the postsynaptic neuron (Golbert et al., 2017). A schematic of the different cascade pathways to induce LTP or LTD is presented in Figure 4.3. A high level of calcium concentration will trigger a cascade of kinases (Figure 4.3.A) while a lower level of calcium concentration will trigger a cascade of phosphatases and prevent the activation of the kinases (Figure 4.3.B).

In the dendritic spine, the first step is the binding of calcium with *calmodulin* (CaM), which is an abbreviation for **cal**cium-**modul**ated prote**in**. Calmodulin is a calcium-binding protein involved
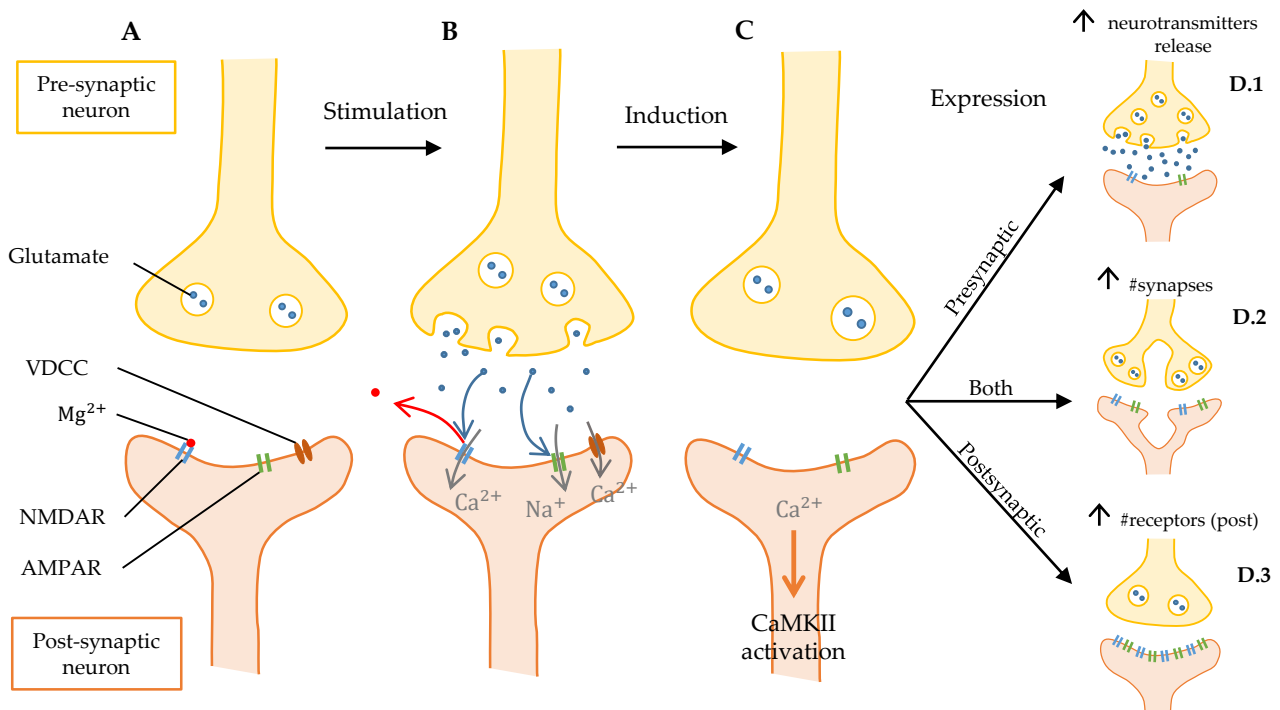
Figure 4.2 – Molecular mechanism of LTP. **A.** The pre-synaptic neuron (yellow) is ready to release the neurotransmitters (glutamate) contained in synaptic vesicles once it receives a stimulus. The post-synaptic neuron (orange) contains NMDARs, AMPARs and VDCCs. The NMDARs are blocked are by the Mg^{2+} and no ions can pass through them. **B.** When the pre-synaptic neuron is stimulated, glutamate is released from synaptic vesicles and binds to AMPARs and NMDARs, which activates those receptors. The activation of NMDARs leads to the influx of Na^+ ions into the post-synaptic neuron, which leads to the depolarization of the post-synaptic neuron. This removes the Mg^{2+} blockage on NMDARs and Ca^{2+} ions can enter the post-synaptic neuron. **C.** Ca^{2+} ions trigger the activation of CaMKII. **D.** LTP has different forms of expression: an increase in the neurotransmitters release from the pre-synaptic neuron (**D.1**), an increase of the synaptic surface between the neurons (**D.2**) and an increase in the number of post-synaptic receptors (**D.3**). Adapted from (Vandewalle and Leprince, 2019).
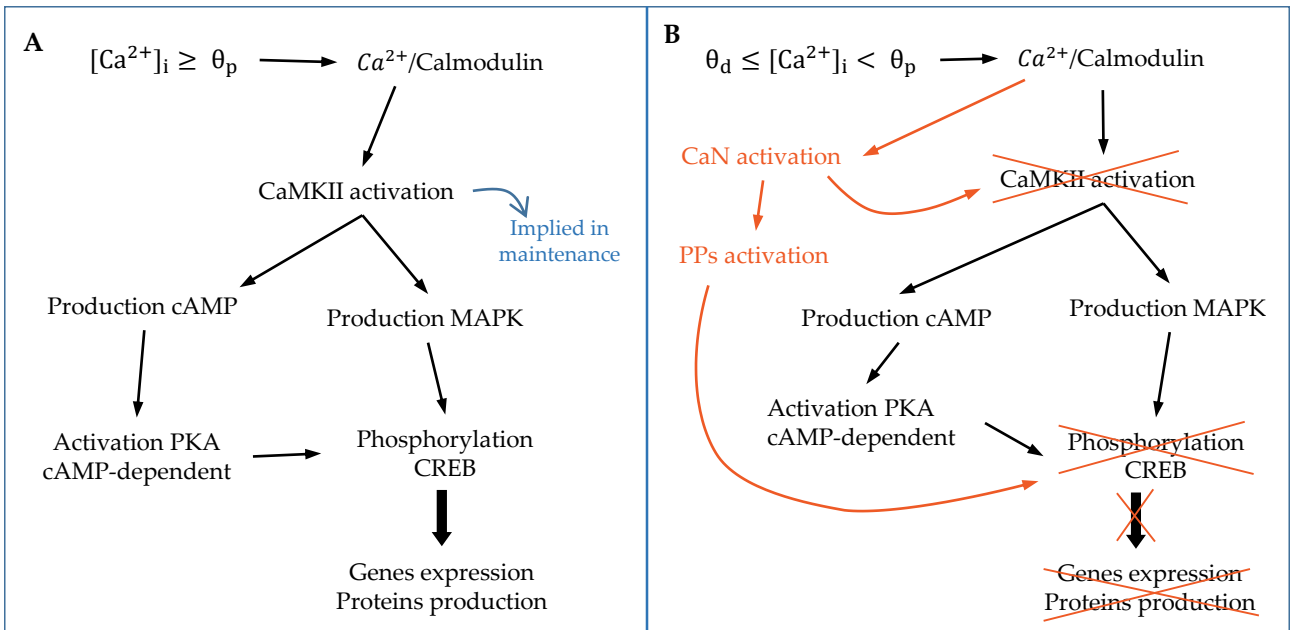
Figure 4.3 – Cascade pathways of LTP and LTD induction. θ_p is the threshold to exceed to get a potentiation and θ_d is the depression threshold. **A.** LTP induction. High levels of calcium concentration ($[\text{Ca}^{2+}]_i \geq \theta_p$) allow the activation of the CaMKII which finally results in the CREB protein phosphorylation. This phosphorylation leads to genes expression and proteins production. CaMKII also has the ability of autophosphorylation so this protein kinase also has a role of synaptic plasticity maintenance. **B.** LTD induction. Lower levels of calcium ($\theta_d \leq [\text{Ca}^{2+}]_i < \theta_p$) activate the calcineurin phosphatase (CaN) which, in turn, activates protein phosphatases (PPs) and prevents the CREB phosphorylation. Inspired from (Vandewalle and Leprince (2019), Golbert et al. (2017)).

in many calcium-mediated processes. Calmodulin is a protein that acts as a calcium level sensor and relays information to calcium-sensitive enzymes, ion channels, and other proteins. The binding of Ca^{2+} to CaM thus allows its activation, which in turn allows the activation of different protein kinases or phosphatases (Shuchismita Dutta, 2003). A schematic showing the binding of the Ca/calmodulin complex to CaMKII and the phosphorylation steps of the CaMKII is shown in Figure 4.4.

Protein kinases and phosphatases are enzymes that allow the catalysis of the transfer of phosphate between their substrates. Even if they both allow the transfer of phosphate, they act in opposing ways. Indeed, a protein kinase catalyses the transfer of the γ-phosphate group from ATP (or GTP) to its protein substrates. A protein phosphatase allows the catalysis of the transfer of the phosphate from a phospho-protein, *i.e.* a protein on which phosphate has been previously attached, to a water molecule. Those opposing phosphate transfer reactions modulate the structure and functions of many cellular proteins (Cheng Heung-Chin (2011), Bear Mark (2007)).

For high levels of calcium (see Figure 4.3.A), the Ca^{2+}/calmodulin complex activates the *calcium/ calmodulin-dependent protein kinase II* (CaMKII), which is a protein kinase involved in many signalling cascades. The activation of CaMKII allows the production of *cyclic adenosine monophosphate* (cAMP) and the activation of *mitogen-activated protein kinase* (MAPK). Then the production of cAMP allows the activation of the *protein kinase A* (PKA). MAPK and PKA-cAMP-dependent altogether allow the phosphorylation of the *cAMP response element-binding* protein (CREB). CREB is an intracellular protein that regulates the expression of genes. The phosphorylated form of CREB is a transcriptional factor that binds to DNA CRE sequences and regulates the transcription of genes crucial for synaptic plasticity, in the short-term and long-term (Golbert et al. (2017), Bear Mark (2007)).

As a consequence, the phosphorylation of CREB protein allows the expression of genes which leads to the production of new proteins and this leads thus to long-term modifications of the synapse. In particular, those modifications concern the trafficking of AMPARs at the synapse. In the short term, there is also phosphorylation of receptors which allows enhancing their efficacy (*i.e.* higher conductance) (Vandewalle and Leprince, 2019).
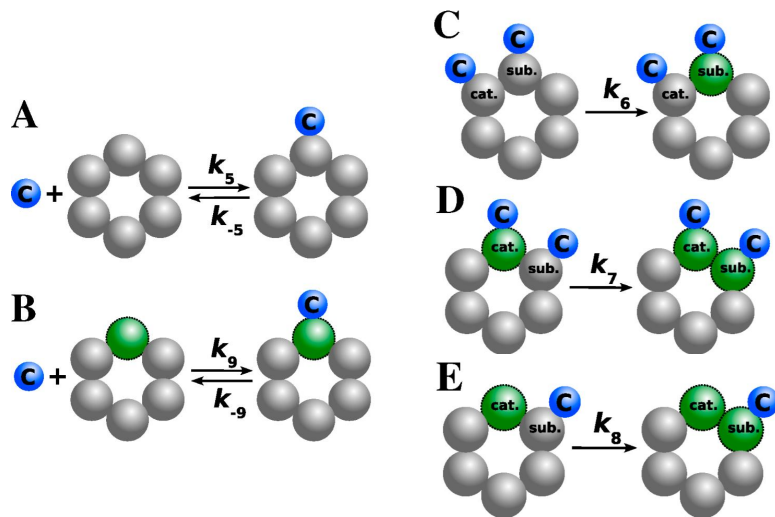
Figure 4.4 – Ca^{2+}/calmodulin binding to a CaMKII subunit (**A**, **B**) and CaMKII phosphorylation steps (**C-E**). The Ca^{2+}/calmodulin complex is represented by a blue circle and a green circle represents a phosphorylated subunit of the CaMKII. The Ca/calmodulin complex can bind either to a dephosphorylated with a dissociation constant $K_5 = k_{-5}/k_5$ (**A**) either to a phosphorylated subunit with a dissociation constant $K_9 = k_{-9}/k_9$ (**B**). There are three possible intersubunit phosphorylation steps (**C-E**). The catalytic subunit is labelled with *cat.*, the substrate one with *sub.* and unlabeled subunits are represented as dephosphorylated.

C. Initiation step: the Ca/CaM has to bind on two interacting subunits (the substrate and the catalyst) to phosphorylate the substrate subunit. The autophosphorylation rate is equal to k_6.

D. Ca/CaM binds to two interacting subunits: the phosphorylated catalyst and the substrate subunit to be phosphorylated. The autophosphorylation rate is equal to k_7.

E. The catalyst can stay phosphorylated after the dissociation of Ca/CaM from it. It allows the phosphorylation, with a rate k_8, of the substrate subunit on which the Ca/CaM complex has been bound to.

Note that the Ca/CaM complex binding and the different autophosphorylation steps are assumed to be independent of the phosphorylation states of the other CaMKII subunits (Graupner and Brunel, 2007).

Calcium influx into the post-synaptic neuron also influences the movements of AMPARs. Indeed, in a study, Borgdorff and Choquet (2002) suggested that this Ca^{2+} influx prevents the diffusion of AMPARs and thus allowed the accumulation of those receptors at the post-synaptic membrane. Moreover, recent studies showed that other AMPARs co-agonists (glycine and D-serine) are implied in the trafficking of those receptors to the membrane (Ferreira et al., 2017).

It is also important to note that CaMKII has an ability of autocatalytic activation, even without the Ca^{2+}/calmodulin complex. This means that CaMKII serves not only to LTP but also maintenance in the synaptic strength since its auto-phosphorylation can activate the different kinase proteins described above (Giese et al., 1998).

As illustrated in Figure 4.3.B, lower levels of calcium activate phosphatases instead of kinases. Indeed, the Ca^{2+}/calmodulin complex activates *calcineurin* (CaN), which is a calcium/calmodulin-dependent protein phosphatase. This is the only phosphatase activated by the Ca^{2+}/calmodulin complex and it activates other protein phosphatases (PP). This activation dephosphorylates the different kinases that were phosphorylated after their activation (for the LTP induction). Those dephosphorylations lead to the dephosphorylation of the CREB protein and this results in no gene expression for the production of new proteins. The dephosphorylation of the different proteins can trigger the endocytosis and the degradation of AMPARs. Moreover, lower levels of calcium concentration can also directly dephosphorylate the AMPARs and NDMARs present at the membrane of the dendritic spine (Golbert et al., 2017).

A summary of the different cascade pathways triggered by the binding of Ca^{2+} to calmodulin to induce LTP and LTD is presented in Figure 4.3.

4.4 Link between calcium role in plasticity and sleep

Recent studies showed that the levels of cAMP, MAPK and CREB undergo a circadian rhythm. Indeed, Luo et al. (2013) conducted experiments on mice and studied the CA1 region of the hippocampus. They reported higher levels of cAMP and MAPK activity and CREB phosphorylation during REM sleep compared to non-REM sleep and awake state.

Other studies showed that sleep deprivation can reduce the levels of phosphorylation of AMPARs. This prevents the insertion of AMPARs into the membrane of the neuron (Golbert et al., 2017).

Moreover, it has been shown that the calcium levels in neocortical dendrites were increased and synchronized with the spindle oscillations encountered in the EEG (Seibt et al., 2017).

4.5 How to model synaptic plasticity?

The synaptic plasticity between two neurons is measured by the synaptic weight variable w. As represented in Figure 4.5, there exist two main ways to model synaptic plasticity.

On one hand, the *phenomenological model*s try to use the pre- and post-synaptic spikes timing and frequency to compute the synaptic weight change Δw. The issue with this type of models is that the relationship between the neuron spikes and Δw can be very complex and represented by a black box. The model will not be very intuitive to understand.

On the other hand, the *biophysical models* take into account the biological aspect behind the synaptic plasticity changes. This type of models may be very complex if all the biological processes are considered or very simple if simplifications have been made.

As reported by Clopath (2015), the main types of synaptic plasticity models that have been implemented until now are:

- Firing-rate models: those take into account only the firing rates of the pre- and post-synaptic neurons;
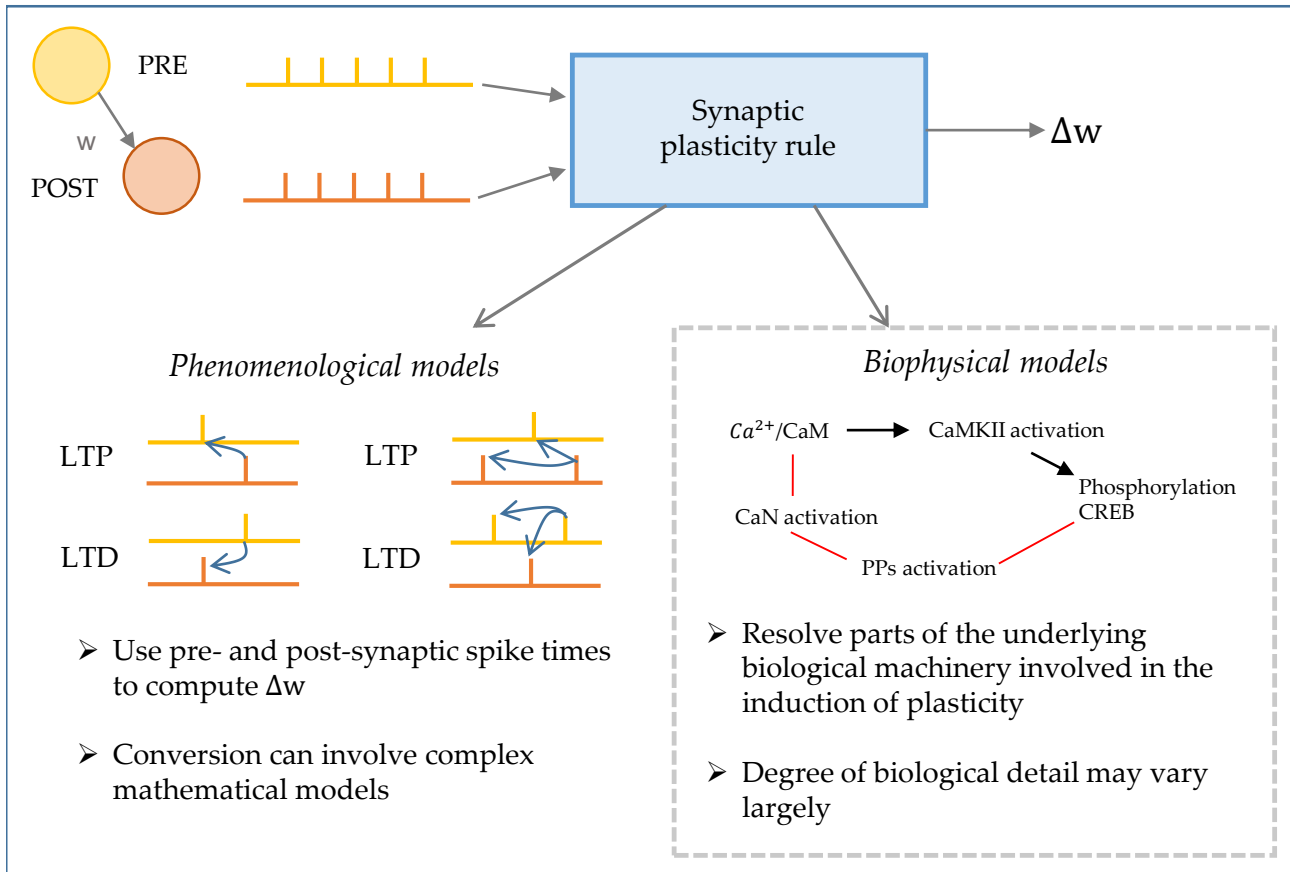
Figure 4.5 – Schematic of the different ways to describe the synaptic plasticity rule between two neurons. Adapted from Graupner (2020).

- Spike-timing dependent plasticity (STDP): those models depend on the precise timing between the pre-synaptic and post-synaptic spikes;

- Models based on the STDP and the post-synaptic voltage;

- Models based on post-synaptic receptors (AMPARs and NMDARs) dynamics;

- Models based only on the post-synaptic calcium concentration;

- Models based on the CaMKII dynamics.

In the context of this Master's thesis, it is assumed that the synaptic weight depends directly on the post-synaptic calcium concentration, *i.e.* $w = f([Ca^{2+}])$. The calcium-based models that are explained in Chapter 5 consider that the synaptic weight changes depend directly on the fact the calcium concentration levels exceed or not a potentiation and/or a depression threshold, as represented in Figure 4.6. This reflects the activation of kinases or phosphatases depending on the intracellular post-synaptic Ca^{2+} level, as explained in Section 4.3.

Finally, the calcium concentration in the post-synaptic spine is assumed to depend on the pre- and post-synaptic neurons activity, *i.e.* $[Ca^{2+}]_i = f(V_{pre}, V_{post})$.
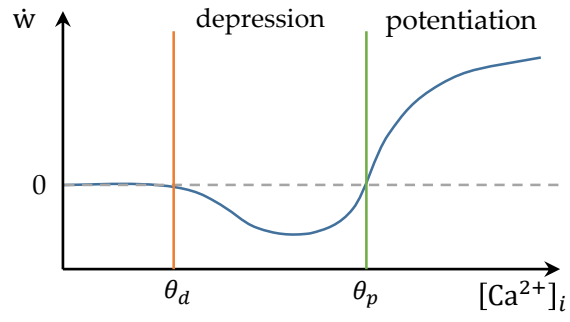
Figure 4.6 – Dependence of the intracellular calcium concentration $[Ca^{2+}]_i$ on the synaptic weight changes. θ_d is the depression threshold and θ_p is the potentiation threshold.

4.6   Summary

Synaptic plasticity

A. Neuron level

Pre-synaptic neuron(s)

Post-synaptic neuron

B. Synapse level

AMPARs

NMDARs

Ca^{2+}

VDCCs

Synaptic strength w

$[Ca^{2+}] \geq \theta_p$
$\rightarrow$ Kinases activation
$\Rightarrow$ LTP

$\theta_d \leq [Ca^{2+}] < \theta_p$
$\rightarrow$ Phosphatases activation
$\Rightarrow$ LTD

C. Synaptic plasticity

$$\frac{d[Ca^{2+}]}{dt} = f(V_{pre}, V_{post})$$

$$\frac{dw}{dt} = f([Ca^{2+}])$$

$\dot{w}$

θ_d

0

θ_p

$[Ca^{2+}]$

Sleep & wake   *(rhythm of a single neuron)*

Sleep

Wake

Due to?
➢ Intrinsic neuron properties
➢ Exogenous bursting

Part II

Modeling calcium-based synaptic plasticity

Chapter 5

Calcium-based synaptic plasticity models

5.1 Graupner and Brunel

5.1.1 Model description

In 2007, Graupner and Brunel have first developed a calcium-dependent model based on the role of the CaMKII on the LTP. Their biochemical model is based on the CaMKII autophosphorylation and dephosphorylation due to protein kinases/phosphatases cascades. In this model, they considered that the CaMKII activation has two stable states: one corresponding to a high phosphorylation level (UP) and one corresponding to a low phosphorylation level (DOWN). With this model, Graupner and Brunel succeeded to show that, starting from a resting intracellular calcium concentration, a high calcium level transient allows the system to switch from the DOWN to the UP state, similarly to LTP. On the contrary, intermediate calcium concentration transients increase the dephosphorylation activity of the CaMKII and allows the transition from the UP to the DOWN state, similarly to LTD. They showed that this can occur only if the dephosphorylation activity is triggered by lower calcium levels than phosphorylation activity. They considered that the post-synaptic calcium concentration elevation was induced by the pre- and post-synaptic spikes. This way, they could examine how different spike-timing protocols change the post-synaptic Ca^{2+} concentration and how those affect the state of the CaMKII phosphorylation.

In 2012, Graupner and Brunel have developed a simplified version of their previous model, where they considered that the synaptic plasticity based only on the post-synaptic calcium concentration levels. They considered that potentiation (LTP) and depression (LTD) are activated when post-synaptic calcium levels are above the corresponding thresholds. This model allowed Graupner and Brunel to reproduce a large number of different spike-timing-dependent plasticity curves but also to reproduce the frequency dependence. In this model, the synaptic efficacy still has two stable states at rest. In 2016, Graupner et al. simplified even more their model and they considered that the synaptic efficacy was always stable at rest, *i.e.* when the calcium concentration level is too low to trigger LTP or LTD.

5.1.2 Equations

Synaptic weight change

In their model, Graupner et al. (2016) considered a single synapse that encounters a train of pre- and post-synaptic action potentials. They considered that the synaptic weight w changes depending on the instantaneous post-synaptic calcium concentration c(t), as presented in eq. 5.1.

$$\tau_{cb}\dot{w} = \gamma_p(1-w)\Theta\left[c(t) - \theta_p\right] - \gamma_d w \Theta\left[c(t) - \theta_d\right] \tag{5.1}$$

The parameter τ_{cb} is the time constant of the synaptic efficacy changes.

The first two terms of the right-hand side represent the influence of the calcium-induced signaling cascades leading to LTP or LTD in a very simplified way:

- θ_d and θ_p denote the depression and potentiation thresholds;

- Θ denotes the Heaviside function, also called the step function, and is such that $\Theta[c(t) - \theta] = 1$ if $c(t) \geq \theta$ and $\Theta[c(t) - \theta] = 0$ if $c(t) < \theta$;

- In case of depression, $c(t) \geq \theta_d$;

- In case of potentiation, $c(t) \geq \theta_p$;

- The parameters γ_p and γ_d measure the rates of synaptic increase/decrease when potentiation and depression thresholds are exceeded.

This way, the synaptic weight will increase or decrease depending on if the calcium concentration c(t) is above the potentiation threshold θ_p or above the depression threshold θ_d.

Calcium dynamics

As shown in eq. (5.1), the synaptic weight depends directly on the calcium concentration $c(t)$. In their model, Graupner et al. (2016) have examined two variants of the post-synaptic calcium concentration dynamics.

Firstly, they considered a linear calcium dynamics they already used in a previous study (see Graupner and Brunel (2012)). The equation describing the linear post-synaptic calcium dynamics is presented in eq. (5.2). In this equation, C_{pre} and C_{post} represent the calcium transients induced by the pre- and post-synaptic action potentials. C_{pre} corresponds to the increase of post-synaptic calcium after a pre-synaptic spike (*i.e.* resulting from the calcium influx through NMDARs) and C_{post} corresponds to the increase of calcium concentration triggered by a post-synaptic spike resulting from VDCCs activation. This way, eq. (5.2) simply implements the sum of the pre- and post-synaptic spike contributions on the total calcium concentration. τ_{Ca} is the calcium time constant, *i.e.* the rate at which the calcium concentration decays over time, and D is the delay for the pre-synaptic spike to impact the post-synaptic calcium concentration. In other words, D describes the slow rise time of the NMDAR-mediated calcium influx. t_i and t_j are the time steps at which the pre- and post-synaptic spikes occur. They set the resting calcium concentration to 0 and they used dimensionless calcium concentrations. To better visualize how those parameters are implied in the calcium concentration level, see Figure 5.1.

$$c(t) = \sum_i C_{\text{pre}} \exp\left(-\frac{t - t_i - D}{\tau_{Ca}}\right) + \sum_j C_{\text{post}} \exp\left(-\frac{t - t_j}{\tau_{\text{Ca}}}\right) \tag{5.2}$$

It is possible to describe the evolution of C_{pre} and C_{post} individually. Indeed, the pre-synaptic spike induces calcium transients as presented in eq. (5.3), where τ_{Ca} is the calcium decay time constant, C_{pre} the calcium transient induced by the pre-synaptic spike and D is the delay between pre-synaptic spike and the induced calcium transient, as introduced in the linear dynamics. t_i represent the time steps at which the pre-synaptic spikes occur.

$$\dot{c}_{\text{pre}}(t) = -c_{\text{pre}}/\tau_{Ca} + C_{\text{pre}} \sum_i \delta(t - t_i - D) \tag{5.3}$$

The calcium transient C_{post} induced by the post-synaptic spike is given in eq. (5.4), where t_j corresponds to the time steps at which the post-synaptic spikes occur.

$$\dot{c}_{\text{post}}(t) = -c_{\text{post}}/\tau_{Ca} + C_{\text{post}} \sum_j \delta(t - t_j) \tag{5.4}$$

The total post-synaptic calcium concentration is thus defined by the sum of the pre- and post-synaptic calcium transients:

$$c(t) = c_{pre}(t) + c_{post}(t) \tag{5.5}$$
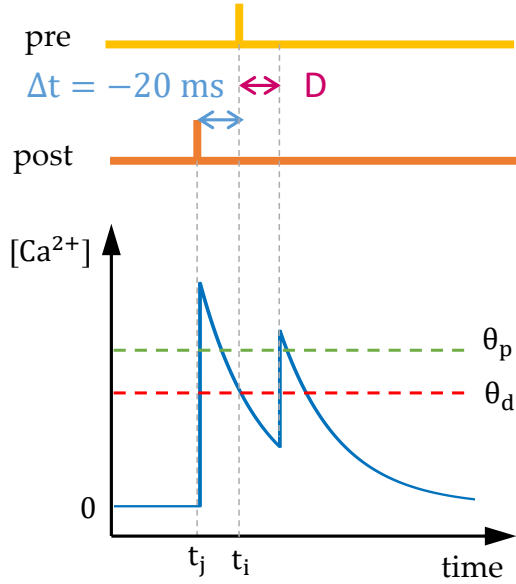
Figure 5.1 – Evolution of the total post-synaptic calcium concentration due to a post-synaptic spike followed by a pre-synaptic spike. The time course of the two spikes is represented at the top: the pre-synaptic spike occurs at time t_i and the post-synaptic one at t_j. The delay between the two spikes corresponds to $\Delta t = -20ms$ ($\Delta t > 0$ for a pre-post stimulation and $\Delta t < 0$ for a post-pre stimulation). The variable D reflects the time for the pre-synaptic spike to affect the total calcium concentration. The dotted lines represent the concentration thresholds to induce a potentiation (green line) and a depression (red line). Adapted from (Graupner and Brunel, 2012).

Secondly, they also considered a non-linear version of calcium dynamics representing the summation of the non-linear calcium concentration transients occurring when the post-synaptic spike happens after the pre-synaptic one. This non-linear summation represents the non-linear part of the calcium current induced by NMDARs. This current is triggered when there is a coincident occurrence of the post-synaptic depolarization and the pre-synaptic activation.

This non-linear version of the calcium dynamics leads to the adaptation of eq. (5.4) with the introduction of a supplementary term ξ:

$$\dot{c}_{\text{post}}(t) = -c_{\text{post}}/\tau_{Ca} + C_{\text{post}} \sum_{j} \delta(t - t_j) + \xi \sum_{j} \delta(t - t_j) c_{\text{pre}} \tag{5.6}$$

When the pre-synaptic activation and the post-synaptic depolarization occur at the same time, ξ increases the NMDA-mediated current. In other words, ξ defines the calcium concentration transient evoked after a post-synaptic spike if it is preceded by a pre-synaptic spike. It is defined by the following equation, where n is a non-linearity factor used to normalize the calcium transients to the expected value:

$$\xi = \frac{n(C_{\text{post}} + C_{\text{pre}}) - C_{\text{post}}}{C_{\text{pre}}} - 1 \tag{5.7}$$

For the non-linear version, Graupner used a value $n = 2$ and $n = 1$ for the linear version. For the sake of simplicity, it is possible to directly consider the equations from the non-linear calcium dynamics and replace the value of n to 1 to consider the linear version of the calcium dynamics.

The total post-synaptic calcium concentration is thus defined by the sum of the pre- and post-synaptic calcium transients:

$$c(t) = c_{pre}(t) + c_{post}(t) \tag{5.8}$$

The parameters of the model were determined by fitting the model to experimental plasticity data obtained from synapses between layer V neurons in the rat visual cortex (Sjöström et al., 2001) and are presented in Table 5.1. To get the parameter values of the calcium-based model, Graupner et al. (2016) reproduced the experimental protocol from Sjöström et al. (2001). It consists in presenting at a given frequency spike-pairs with a fixed Δt between the pre- and post-synaptic spikes.

A simple simulation of the pre-synaptic and post-synaptic evoked calcium transients with the corresponding synaptic weight evolution is given in Figure 6.3. In this Master's thesis, only the linear calcium dynamics has been simulated, the non-linear one leading to numerical issues because of the presence of Dirac functions.

Moreover, it was possible to reproduce the synaptic weight changes depending on the firing rate of both the pre- and post-synaptic spikes (see Section 6.1).

Parameter	Unit	Linear calcium dynamics	Non-linear calcium dynamics
τ_{Ca}	ms	22.27212	18.93044
C_{pre}		0.88410	0.86467
C_{post}		1.62138	2.30815
θ_d		1	1
θ_p		2.009289	4.9978
γ_d		137.7586	111.82515
γ_p		597.76129	894.23695
τ_{cb}	s	520.76129	707.02258
D	ms	9.53709	10
n		1	2

Table 5.1 – Parameters of the calcium-based model used to fit experimental plasticity data (Sjöström et al., 2001). Table from (Graupner et al., 2016).

5.2   Shouval, 2002

Shouval et al. (2002) have constructed a model to describe the calcium concentration levels depending only on NMDARs activity.

Equations describing the model

The model is based on a minimal set of assumptions that give the different equations governing the model. They know there are other sources of calcium influx into the post-synaptic neuron but they wanted to show that based on this minimal set of assumptions, they could qualitatively reproduce the different induction protocols.

Assumption 1: the calcium control hypothesis.   Shouval and his team assumed that calcium was the primary source of synaptic plasticity. This way, different levels of calcium concentrations will trigger different forms of synaptic plasticity. This hypothesis can be formulated as:

$$\dot{W}_j = \eta \Omega \left([Ca]_j\right) \tag{5.9}$$

Where W_j is the synaptic strength of the synapse j, η is the learning rate and $[Ca]_j$ is the calcium level of the synapse j. Ω represents the dependence of the synaptic weight W_j on threshold values for the calcium concentration. The variation of Ω and η depending on the calcium concentration levels is shown in Figure 5.2.

They added a decay term to the equation (5.9) in order to stabilize the synaptic growth without imposing a saturation value. Indeed, for a sustained elevated level of calcium, the equation 5.9 would lead to an indefinite increase/decrease of the synaptic weight. They got the following equation:

$$\dot{W}_j = \eta \left([Ca]_j\right) \left(\Omega \left([Ca]_j\right) - W_j\right) \tag{5.10}$$

In eq. (5.10), they also assumed that the learning rate η is calcium-dependent and increases monotonically with calcium concentration levels. This allows avoiding oscillations and the fact that the synaptic weight can converge directly back to its initial value when calcium levels go back to their basal values. The term η is equal to the inverse of the learning time τ. η is a dynamical variable that allows avoiding the cancellation of the synaptic growth if a calcium concentration excess above θ_p (potentiation) is followed by a calcium concentration between θ_d and θ_p (depression).

The equations describing the evolution of τ and η are the following:

$$\eta([Ca]_j) = \frac{1}{\tau([Ca]_j)} \tag{5.11}$$

$$\tau([Ca]_j) = P_1 + \frac{P_2}{P_3 + [Ca]_j P_4} \tag{5.12}$$
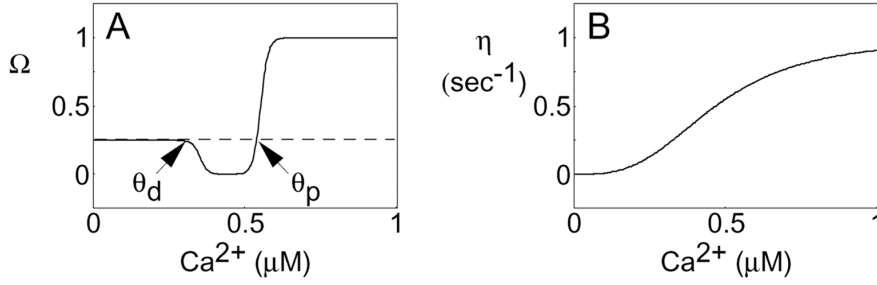
Figure 5.2 – Illustration of the calcium control hypothesis. **A.** The $\Omega([Ca^{2+}])$ function: when $[Ca]_j < \theta_d$, the synaptic weight is unchanged, when $\theta_d < [Ca]_j < \theta_p$, the synaptic weight is decreased (*i.e.* depressed) and when $[Ca]_j > \theta_p$, the synaptic weight is increased (*i.e.* potentiated). **B.** Evolution of the learning rate $\eta([Ca^{2+}])$ (Shouval et al., 2002).

With $P_1 = 1s$, $P_2 = 0.1s$, $P_3 = P_2 \cdot 10^{-4}$, $P_4 = 3$. The function $\eta([Ca]_j)$ thus describes a sigmoid.

The equation (5.13) describes the evolution of $\Omega([Ca]_j)$ depending on the intracellular calcium concentration level.

$$\Omega([Ca]_j) = 0.25 + \frac{1}{1 + exp(-\beta_2([Ca]_j - \alpha_2))} - 0.25\frac{1}{1 + exp(-\beta_1([Ca]_j - \alpha_1))} \tag{5.13}$$

Where $\alpha_1 = 0.35$, $\alpha_2 = 0.55$, $\beta_1 = 80$ a,d $\beta_2 = 80$. The initial value of w was set at 0.25. The functional form of $\Omega_w([Ca]_i)$ is presented in Figure 5.2.

This way, the eq. (5.10) defines the calcium control hypothesis and is also interesting because one can observe that the synaptic weight W converges to the value of Ω with a certain time constant τ. Depending on the calcium level, this time constant changes but also the value of Ω.

Assumption 2: NMDARs are the primary source of calcium. When the post-synaptic depolarization is paired with pre-synaptic activity, Shouval et al. have assumed that NMDARs are the primary source of calcium, even though there exist other calcium sources, such as VGCCs and intracellular storage. Moreover, this entry of calcium through NMDARs is essential for the LTP/LTD induction (cf. Section 4.3).

Equation (5.14) represents the calcium current through NMDARs:

$$I_{NMDA}(t_i) = P_0 G_{NMDA} \left[I_f \theta(t) e^{-t/\tau f} + I_s \theta(t) e^{-t/\tau_s} \right] H(V) \tag{5.14}$$

Where

- $H(V)$ represents the voltage dependence of the NMDARs (caused by the Mg^{2+} blockade). V is the post-synaptic potential;

- $P_0 = 0.5$ is the fraction of NMDARs that are closed and then opens after a pre-synaptic spike;

- G_{NMDA} is the peak value of the NMDARs conductance;

- $\theta = 0$ if $t < 0$ and $\theta = 1$ if $t \geq 0$.

The temporal dynamics represented in eq. (5.14) shows a sum of a fast ($\tau_f = 50ms$) and a slow ($\tau_s = 200ms$) exponentials.

$H(V)$ is defined such that $H(V) = B(V)(V - V_r)$, where $(V - V_r)$ expresses the driving force of the calcium influx, with V_r the reversal potential of calcium ions (see Table A.1). $B(V)$ represents the voltage-dependence of the Mg^{2+} blockade and is defined by eq. (5.15), where $[Mg]$ is the magnesium concentration.

$$B(V) = \frac{1}{1 + exp(-0.062V)\frac{[Mg]}{3.57}} \tag{5.15}$$

The calcium concentration dynamics is thus represented by eq. (5.16). Shouval chose a time constant $\tau_{Ca} = 50ms$ for the calcium concentration dynamics.

$$\frac{d[Ca(t)]}{dt} = I_{NMDA}(t) - (1/\tau_{Ca})[Ca(t)], \tag{5.16}$$

Assumption 3: Back-propagating spikes that contribute to STDP have a slow after-depolarizing tail. According to the *Spike-timing dependent plasticity* (STDP) theory, a post-synaptic spike occurring a certain time window after a pre-synaptic spike produces LTP while a post-synaptic spike that occurs before the pre-synaptic one will induce LTD. Knowing that, Shouval and his team considered that a pre-post stimulation leads to a high calcium concentration elevation (above θ_p) while a post-pre stimulation leads to a moderate calcium concentration elevation (between θ_d and θ_p).

This information about the post-synaptic spiking can be transmitted back to the synapse through a *back-propagating action potential* (BPAP). A BPAP is opposed to forward propagation, which propagates the action potential along the axon to the synapse. Here, a BPAP occurs along the axon back to the dendrites. Since Shouval considered assumption 2, *i.e.* only calcium through NMDARs could influence the synaptic plasticity, the BPAP can influence the synaptic plasticity only by modifying this calcium influx through the NMDARs. This can be done by changing the post-synaptic voltage after the binding of glutamate to receptors that are implied in the Ca^{2+} influx. However, this BPAP must have a wide after-depolarizing tail. Indeed, if the duration of the BPAP is too short, this would raise the Mg^{2+} blockage from the NMDARs for only a short period and the calcium concentration elevation would be too small and not reflect the pre-post stimulation. This way, Shouval et al. have defined a BPAP composed of a fast spike, defined by a time constant τ_f^{bs}, and a slower after-depolarizing potential (ADP), with a time constant τ_s^{bs}. They thus got the eq. (5.17) to define the BPAP temporal evolution.

$$BPAP(t) = 100 * \left[\left(I_f^{bs} \exp\left(-t/\tau_f^{bs}\right) + I_s^{bs} \exp\left(-t/\tau_s^{bs}\right) \right) \right] \tag{5.17}$$

100 represents the maximal depolarization of the BPAP, I_f^{bs} is the magnitude of the fast spike component and I_s^{bs} is the magnitude of the slow spike component. Shouval has defined the after-depolarizing potential amplitude to be coherent with experimental dendritic measures (Magee and Johnston (1997), Larkum ME (2001)). This definition of the BPAP allowed Shouval, Bear and Cooper to get a higher calcium concentration with a post-pre stimulation than a presynaptic stimulation alone. Moreover, they could get a larger calcium concentration elevation with a pre-post stimulation than a post-pre stimulation. The definition of such a BPAP allowed Shouval to get results that are consistent with experimental data.

Note that Shouval et al. did not mention how they considered those BPAPs in the equations describing their calcium-based model. However, it was explained that the post-synaptic activity depends on the amplitude of the BPAPs and the EPSPs generated by the binding of glutamate on AMPARs. They did not considered the depolarization due to currents through NMDARs. Shouval et al. thus defined the post-synaptic depolarization as the linear sum of the BPAPs and the EPSPs, *i.e.* $V(t) = BPAP(t) + EPSP(t)$, with the following equation describing the EPSP:

$$\text{EPSP}(t) = \frac{s}{norm} * \sum_i \left(\exp\left(-(t-t_i)/\tau_1^{ep}\right) - \exp\left(-(t-t_i)/\tau_2^{ep}\right) \right) \tag{5.18}$$

Where t_i are the times at which the pre-synaptic spikes occur, τ_1^{ep} and τ_2^{ep} are the time constants describing the EPSPs dynamics. The parameter s reflect the spatial summation of the experimental stimulation protocols and $norm$ is a normalization factor so that the peak of the EPSP equals to s. Since $V(t)$ is taken into account in the $H(V)$ term from eq. (5.14), it is assumed that Shouval et al. considered the BPAPs and EPSPs contribution in their calcium-dependent model thanks to this term $H(V)$.

However, Shouval noticed that only taking into account those three assumptions can lead to an unstable model. They have proposed a fourth assumption: **metaplasticity is required for the system stability**. In this paper, Shouval showed that this metaplasticity can be handled with a change in the NMDARs kinetics. In another paper (Shouval HZ, 2002), they developed a model to take into account the dynamics of the AMPARs/NMDARs depending on their phosphorylation level (due to the CaMKII activation, cf. Section 4.3).

Yeung et al. (2004) also proposed an adaptation of this model to counteract the issue of instability thanks to homeostatic regulation of intracellular calcium levels. This is done through a slow and activity-dependent regulation of the NMDAR permeability. This permeability depends on the time-varying membrane potential such that:

- If the post-synaptic membrane potential is chronically low, the NMDAR conductance increases to allow more potentiation;

- If it is persistently high, the NMDAR conductance decreases.

To summarize, this model thus allows modeling the calcium-induced synaptic plasticity. Shouval et al. (2002) have considered that the post-synaptic calcium concentration levels depend on the calcium influx through NMDARs only. Depending on the calcium concentration level, LTP or LTD can be induced and this model is able to implement both the various induction protocols and naturally occurring plasticity. However, Shouval et al. specified that this model gives a basis for NMDAR-dependent synaptic plasticity but it still has to be tuned on real experimental data.

5.3 Standage 2014

5.3.1 Model description

Their model is based on the fact that high levels of post-synaptic calcium trigger a cascade of protein kinases and lead to LTP while intermediate levels of calcium trigger a cascade of protein phosphatases, which lead to LTD. They also assumed that NMDARs allow detecting coincidence between the pre- and post-synaptic spikes.

5.3.2 Equations of calcium-based plasticity

Standage et al. (2014) considered that NMDARs activation g_{NMDA} can be characterized by the proportion of the maximum post-synaptic depolarization. It is thus modelled by the equation presented in eq. (5.19).

$$\frac{dg_{NMDA}(t)}{dt} = -\frac{g_{NMDA}(t)}{\tau_{NMDA}} + a_{NMDA} \cdot x_{NMDA}(t) \cdot (1 - g_{NMDA}(t)) \qquad (5.19)$$

Where

- τ_{NMDA} is the calcium decay time constant;

- a_{NMDA} is the receptor saturation;

- x_{NMDA} is the channel opening.

The channel opening is described by the following equation:

$$\frac{dx_{NMDA}(t)}{dt} = -\frac{x_{NMDA}(t)}{\tau_x} + \delta(t - t_{pre}^f) \qquad (5.20)$$

Where

- τ_x is the rise time;

- δ stands for the Dirac function;

- t_{pre}^f represents the time at which the pre-synaptic spike occurs.

In eq. (5.20), one can observe that the channel opening is described by an exponential with a decay constant τ_x. At each pre-synaptic spike occurring at t_{pre}^f, the channel opening is increased by 1 (thanks to the Dirac term $\delta(t - t_{pre}^f)$) and then decreases following the decay rate τ_x. Since Standage et al. (2014) considered that the NMDARs are a coincidence detector, it was assumed that the influx of Ca^{2+} ions occurs when the NMDARs activation overlaps with the back-propagating action potential (BAP or BPAP, see Assumption 3 from (Shouval et al., 2002)). This way, they considered that the BPAPs are constituted of a peak (see eq. (5.21)) and a tail (see eq. (5.22)), in such a way that $BPAP(t) = BPAP_p(t) + BPAP_t(t)$. Standage et al. (2014) also assumed that it is possible to sum the BPAPs, based on experimental evidence (Rosenkranz et al., 2009).

$$\frac{dBPAP_p(t)}{dt} = -\frac{BPAP_p(t)}{\tau_p} + \delta(t - t_{post}^f) \cdot \beta_p \cdot (1 - BPAP_p(t)) \tag{5.21}$$

$$\frac{dBPAP_t(t)}{dt} = -\frac{BPAP_t(t)}{\tau_p} + \delta(t - t_{post}^f) \cdot \beta_t \cdot (1 - BPAP_t(t)) \tag{5.22}$$

In eq. (5.21) and (5.22), the parameters are:

- τ_p is decay time constant;

- t_{post}^f is the time step at which the post-synaptic spike occurs;

- β_p is a scale factor to express the proportion the BPAP magnitude due to the BPAP peak;

- $\beta_t = 1 - \beta_p$;

- τ_t is the half-time of the BPAP.

The post-synaptic calcium concentration is given by the following equation:

$$\frac{dCa(t)}{dt} = -\frac{Ca(t)}{\tau(Ca(t))} + \psi \cdot (Ca^{\max} - Ca(t)) \cdot BAP(t) \cdot g_{NMDA}(t) \tag{5.23}$$

Where ψ is a scale factor and Ca^{max} represents a maximal value of Ca^{2+}. The main characteristics of this calcium-based model is that the Ca^{2+} time constant depends on the Ca^{2+} concentration itself. This allows to characterize the slow extrusion of high concentrations of Ca^{2+} from the dendritic spine. $\tau(Ca)$ is represented by a sigmoid function:

$$\tau(Ca) = \tau_{Ca}^0 + \frac{(T - \tau_{Ca}^0)}{(1 + \exp(-\vartheta(Ca - Ca^{\max}/2))} \tag{5.24}$$

Standage et al. (2014) assumed that synaptic plasticity was determined by LTP and LTD processes, simultaneously. Those are given in equations (5.25) and (5.26).

$$\Delta w_p = \begin{cases} Ca(t) \cdot \kappa_p \cdot (w_{\max} - w) & \text{for } Ca(t) > \Theta_p \\ 0 & \text{for } Ca(t) \leq \Theta_p \end{cases} \tag{5.25}$$

$$\Delta w_d = \begin{cases} Ca(t) \cdot \kappa_d \cdot w & \text{for } Ca(t) > \Theta_d \\ 0 & \text{for } Ca(t) \leq \Theta_d \end{cases} \tag{5.26}$$

Where

- κ_p is the potentiation learning rate;

- κ_d is the depression learning rate;

- w_{max} is the maximal synaptic weight value and is set to $w_{max} = 2$. The initial weight value is set to 1;

- Θ_p and Θ_d are the Ca^{2+} potentiation and depression thresholds, respectively.

They integrated this calcium-based synaptic plasticity into a network model. However, this will not be covered in the context of this thesis.

5.4 Honnuraiah (2013) and Anirudhan (2015)

In 2013, Honnuraiah and Narayanan developed a calcium-based plasticity rule to maintain stable synaptic plasticity. The main difference with the previous explained calcium-based models is that they considered the calcium dynamics but also the NMDARs dynamics in a more physiological way.

The equations of this calcium-based model are interesting because they did not only consider the calcium current through the NMDARs. Indeed, they also took into consideration the Na$^+$ and K$^+$ ionic currents that go through the NMDARs and thus influence the post-synaptic potential. Eq. (5.27) represents the total current through the NMDARs and depends on the individual Ca^{2+}, Na$^+$ and K$^+$ currents (shown in eq. (5.28), (5.29) and (5.30)).

$$I_{NMDA}(V,t) = I_{NMDA}^{Na}(V,t) + I_{NMDA}^{K}(V,t) + I_{NMDA}^{Ca}(V,t) \tag{5.27}$$

$$I_{NMDA}^{Na}(V,t) = \overline{P}_{NMDA} P_{Na} s(t) MgB(V) \frac{VF^2}{RT} \left(\frac{[Na]_i - [Na]_0 exp(-\frac{VF}{RT})}{1 - exp(-\frac{VF}{RT})} \right) \tag{5.28}$$

$$I_{NMDA}^{K}(V,t) = \overline{P}_{NMDA} P_{K} s(t) MgB(V) \frac{VF^2}{RT} \left(\frac{[K]_i - [K]_0 exp(-\frac{VF}{RT})}{1 - exp(-\frac{VF}{RT})} \right) \tag{5.29}$$

$$I_{NMDA}^{Ca}(V,t) = \overline{P}_{NMDA} P_{Ca} s(t) MgB(V) \frac{vF^2}{RT} \left(\frac{[Ca]_i - [Ca]_0 exp(-\frac{VF}{RT})}{1 - exp(-\frac{VF}{RT})} \right) \tag{5.30}$$

Where:

- $\overline{P}_{NMDA}$ is maximum permeability of the NMDAR;

- P_{Na}, P_K and P_{Ca} represent the relative permeabilities of the different ions. $P_{Ca} = 10.6$, $P_{Na} = 1$ and $P_K = 1$;

- $[Na]_o$, $[K]_o$ and $[Ca]_o$ are the extracellular ion concentrations and $[Na]_i$, $[K]_i$ and $[Ca]_i$ are the intracellular ion concentrations.

The intracellular calcium concentration depends on the calcium current through NMDARs and its evolution is given by eq. (5.31).

$$\frac{d[Ca]_i}{dt} = -\frac{10000 I_{NMDA}^{Ca}}{3.6 \cdot dpt \cdot F} + \frac{[Ca]_\infty - [Ca]_i}{\tau_{Ca}} \tag{5.31}$$

In eq. (5.31), the different parameters are:

- F is the Faraday's constant law;

- τ_{Ca} is the calcium decay constant;

- dpt is the depth of the cell;

- $[Ca]_\infty$ is the steady state value of the intracellular calcium concentration, $[Ca]_\infty = 100 nM$.

In the equations describing ion currents through NMDARs, Honnuraiah and Narayanan (2013) also considered the dependence of the Mg^{2+} blockade on the NMDARs current. This blockade needs sufficient depolarization from the cell to be removed. It is thus defined by the following equation:

$$MgB(V) = \frac{1}{1 + \frac{[Mg]_o exp(-0.062V)}{3.57}} \tag{5.32}$$

In eq. (5.32), the value of $[Mg]_o$ is equal to 2 mM. Still in the equations (5.28), (5.29) and (5.30), the term s(t) models the NMDAR current kinetics and is given by the following equation:

$$s(t) = a \left(exp\left(-\frac{t}{\tau_d}\right) - exp\left(-\frac{t}{\tau_r}\right) \right) \tag{5.33}$$

Where a is a normalization constant (such that $0 \leq s(t) \leq 1$), τ_d is the decay time constant and τ_r is rising time constant.

Honnuraiah and Narayanan (2013) also considered the ion currents through AMPARs. Only the K^+ and Na^+ go pass through them.

$$I_{AMPA}(V,t) = I_{AMPA}^{Na}(V,t) + I_{AMPA}^{K}(V,t) \tag{5.34}$$

$$I_{AMPA}^{Na}(V,t) = \overline{P}_{AMPAR} \; w \; P_{Na}s(t)\frac{vF^2}{RT}\left(\frac{[Na]_i - [Na]_0 exp(-\frac{VF}{RT})}{1 - exp(-\frac{VF}{RT})}\right) \tag{5.35}$$

$$I_{AMPA}^{K}(V,t) = \overline{P}_{AMPA} \; w \; P_{K}s(t)\frac{vF^2}{RT}\left(\frac{[K]_i - [K]_0 exp(-\frac{VF}{RT})}{1 - exp(-\frac{VF}{RT})}\right) \tag{5.36}$$

Where

- $\overline{P}_{AMPAR}$ is the AMPAR maximum permeability;

- P_{Na} and P_K are the relative permeabilities of the AMPARs to the Na^+ and K^+ ions, respectively. Those are considered to be equal and are set to 1 by default;

- $s(t)$ describes the AMPARs kinetics. Its equation is the same as in eq. (5.33) but the time constants are different than for NMDARs (see Honnuraiah and Narayanan (2013) for more details);

- w is the synaptic plasticity weight variable.

The synaptic weight is defined by the following equation:

$$\frac{dw}{dt} = \eta_w([Ca]_i)(\Omega([Ca]_i - w)) \tag{5.37}$$

Where $\eta_w([Ca]_i)$ is the calcium-dependent learning rate, inversely related to the calcium-dependent learning time constant $\tau_w([ca]_i)$, and Ω_w also depends on the calcium concentration level. Those calcium-dependent parameters are given in the following equations:

$$\eta_w([Ca]_i) = \frac{1}{\tau_w([Ca]_i)} \tag{5.38}$$

$$\tau_w([Ca]_i) = P_1 + \frac{P_2}{P_3 + [Ca]_i^{P_4}} \tag{5.39}$$

$$\Omega_w([Ca]_i) = 0.25 + \frac{1}{1 + exp(-\beta_2([Ca]_i - \alpha_2))} - 0.25\frac{1}{1 + exp(-\beta_1([Ca]_i - \alpha_1))} \tag{5.40}$$

The parameter values appearing in equations (5.38), (5.39) and (5.40) are the same as Shouval et al. (2002) used (see Section 5.2). Indeed, one can notice that Honnuraiah and Narayanan and Shouval et al. used the same equations to describe the dependence of η_w and Ω_w on the calcium concentration level. The functional forms of η_w and Ω_w are presented in Figure 5.2.

The model developed by Honnuraiah and Narayanan (2013) is interesting since they considered the NMDARs dynamics in a more physiological way, taking into account all the NMDAR-induced currents. They also considered the influence of the Mg^{2+} blockade on the NMDARs dynamics.

In a more recent study of synaptic plasticity stability, Anirudhan and Narayanan (2015) considered the same calcium-based equations for their calcium-induced plasticity modeling.

5.5 Olcese, 2010

Olcese et al. (2010) developed a model based on a spike timing-dependent plasticity (STDP) rule. They chose to follow the STDP rule previously implemented by Standage et al. (2007). Olcese et al. (2010) adapted this STDP, considering that the direction of the induced plasticity (potentiation or depression) depends on the calcium influx entering into the post-synaptic neuron through NMDARs. They modelled this post-synaptic calcium concentration as presented in eq. (5.41). This equation is based on Brader et al. (2007) theory.

$$\frac{\mathrm{d}[\mathrm{Ca}]}{\mathrm{d}t} = -\frac{[\mathrm{Ca}]}{\tau_{\mathrm{Ca}}} + J_{\mathrm{Ca}} \sum \delta\left(t - t_{\mathrm{i}}\right) \tag{5.41}$$

Where J_{Ca} is the contribution of each post-synaptic spike to the calcium influx (the sum runs over the spikes occurring at times t_i) and τ_{Ca} is the calcium depletion time constant. Olcese et al. considered the calcium concentration variable $[Ca]$ is a pseudo-concentration since eq. (5.41) does not describe the calcium influx through NMDARs in the most accurate way.

To implement the calcium-based plasticity rule, they considered that the synaptic plasticity depends on the intracellular calcium level and the thresholds of synaptic changes are related to J_{Ca}:

- A low level of calcium concentration triggers no plasticity;

$$[\mathrm{Ca}] \leq k_1 J_{\mathrm{Ca}} \vee [\mathrm{Ca}] > k_3 J_{\mathrm{Ca}} \Rightarrow \text{ No Plasticity} \tag{5.42}$$

- Intermediate levels of calcium trigger synaptic plasticity following the standard STDP rule;

$$k_1 J_{\mathrm{Ca}} < [\mathrm{Ca}] \leq k_2 J_{\mathrm{Ca}} \Rightarrow \mathrm{LTP} + \mathrm{LTD} \tag{5.43}$$

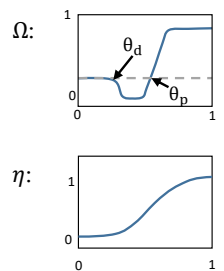- A high level of post-synaptic calcium concentration triggers only LTP.

$$k_2 J_{\mathrm{Ca}} < [\mathrm{Ca}] \leq k_3 J_{\mathrm{Ca}} \Rightarrow \mathrm{LTP} \tag{5.44}$$

They simulated this calcium-dependent STDP rule in a conductance-based model, for a circuit composed of neurons. Those neurons are modelled with each ionic current depending on the peak conductance and the activation/inactivation level of the ionic channel. Besides those ionic currents, they implemented five intrinsic currents: I_h, I_T, $I_{Na(p)}$, I_{DK} and I_{KCa}.

Note that Olcese et al. (2010) also assumed that neuromodulators can have an impact on the STDP rule. Indeed, changing the neuromodulatory milieu can trigger a switch from the awake to the sleep state, as observed by Hill and Tononi (2005) and Esser et al. (2007). To implement this influence, they considered that the neuromodulatory systems change the conductance values of both intrinsic and extrinsic channels. For example, the AMPARs and NMDARs maximum conductance is increased during the transition to the non-REM sleep state. In the same way, the T-type calcium channels conductance is assumed to be increased during the switch to the sleep state.

To summarize, this model is interesting in the sense that it follows the standard STDP rule but Olcese et al. (2010) put an additional rule on the plasticity direction based on post-synaptic calcium concentration levels.

5.6 Summary of calcium-based models

Model	Ca^{2+} source	I_{NMDA} modeling	$[Ca^{2+}]$ modeling	Definition of w	$w([Ca^{2+}])$
Graupner and Brunel, 2016	NMDARs VDCCs		Sum of exponentials	Abstract weight	$\dot{w}(c) \propto$ $(1-w)\Theta[c-\theta_p]$ $-w\Theta[c-\theta_d]$ θ_p: potentiation θ_d: depression
Shouval, 2002	NMDARs	$I_{NMDA} \propto P_0 G_{NMDA} H(V_{pre})$	$\dfrac{d[Ca]}{dt} = f(I_{NMDA}, [Ca])$	Abstract weight	$\dot{w} \propto \eta([Ca]) \cdot \Omega([Ca])$ Ω: η:
Standage, 2014	NMDARs	NMDAR activation: $\dot{g} = -\dfrac{g}{\tau} + a \cdot x \cdot (1-g)$ a: receptor saturation x: receptor opening	$\dfrac{dCa}{dt} = f(Ca, \tau_{Ca}, BAP, g)$	Abstract weight	If LTP: $\Delta w_p \begin{cases} \propto [Ca]\ if\ [Ca] > \Theta_p \\ = 0\ if\ [Ca] \leq \Theta_p \end{cases}$ If LTD: $\Delta w_d \begin{cases} \propto [Ca]\ if\ [Ca] > \Theta_d \\ = 0\ if\ [Ca] \leq \Theta_d \end{cases}$
Honnuraiah (2013) Anirudhan (2015)	NMDARs	$I_{NMDA} = I_{NMDA}^{Na} + I_{NMDA}^{K} + I_{NMDA}^{Ca}$ $I_{NMDA}^{Ca} \propto \bar{P}_{NMDA} \cdot P_{Ca} \cdot s(t) \cdot MgB(V) \cdot ([Ca]_i - [Ca]_o)$	$\dfrac{d[Ca]_i}{dt} = f\left(I_{NMDA}^{Ca}, ([Ca]_i - [Ca]_o)\right)$	Abstract weight	$\dot{w} \propto \eta([Ca]) \cdot \Omega([Ca])$ η, Ω: see Shouval 2002 for their functional form
Olcese, 2010	NMDARs	$I_{NMDA} = f(g_{NMDA}, V)$ $\dot{g}_{NMDA} = f(g_{NMDA}^{peak}, t)$	$[\dot{Ca}] = -\dfrac{[Ca]}{\tau_{Ca}} + J_{Ca}\Sigma\delta(t - t_i)$ J_{Ca}: calcium influx at NMDARs t_i: post-syn. spike timing	Nb. AMPARs	Plasticity direction depends on $[Ca^{2+}]$ levels

Table 5.2 – Summary of the different calcium-based models that are explained in Chapter 5.

Chapter 6

Adapting a calcium-based model considering physiological phenomena

6.1 Reproducing Graupner et al. (2016)

Since the parameters of the model from Graupner et al. (2016) were fitted according to experimental data, it was decided to begin by reproducing this model.

Graupner et al. model was integrated into the conductance-based model from Drion et al. (2018). Indeed, the final goal is to adapt Graupner et al. model with physiological calcium dynamics. This way, while Graupner et al. model considers a spike train which is event-based implemented, the conductance-based model allows having physiological values of the membrane potential. Moreover, during the switch to a bursting mode, the conductance-based model generates this bursting pattern. One does not need to define a particular spiking pattern, as with Graupner et al. model.

In this conductance-based model, the circuit contains three neurons, as shown in Figure 6.1.
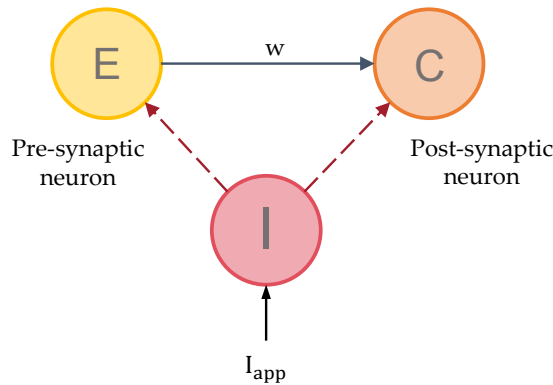
Figure 6.1 – Circuit used in the conductance-based model from Drion et al. (2018). It contains an excitatory thalamocortical neuron (E), a cortical neuron (C) and an inhibitory neuron (I) from the reticular nucleus. The excitatory neuron activity influences the cortical neuron, with a certain synaptic weight w. The inhibitory neuron can influence both the excitatory and cortical neurons. During the switch from the awake to the asleep state, a current I_{app} is applied on the inhibitory neuron.

In Drion et al. model, the equation describing the membrane potential evolution is given by

$$C_m \dot{V}_m = -I_{Na} - I_K - I_{CaT} - I_{K,Ca} - I_H - I_{\text{leak}} + I_{app} \tag{6.1}$$

Where I_{CaT} is the T-type calcium current (see Section A.4) and $I_{K,Ca}$ is the calcium-activated potassium current. The steady-state value of the activation of this calcium-activated K$^+$ current $m_{K,Ca,\infty}$ is described by the following:

$$m_{K,Ca,\infty}([Ca]) = \left(\frac{[Ca]}{[Ca] + K_d} \right)^2 \tag{6.2}$$

With the Ca^{2+} fluctuations described by:

$$\frac{d[Ca]}{dt} = -k1 \cdot I_{CaT} - k2 \cdot [Ca] \tag{6.3}$$

Figure 6.2 shows a temporal simulation of the membrane potential for the three neurons of the circuit (E, C, I). By convention, the pre-synaptic neuron is represented in yellow, the post-synaptic neuron in orange and the inhibitory neuron in pink.

In Drion et al. model, neurons from the thalamus are considered to contain T-type calcium channels so it is possible to observe in Figure 6.2 a bursting pattern from the inhibitory neuron. When neuron I is bursting, it inhibits the activity of both the E and C neurons. One can observe the role of I_{CaT} that allows the inhibitory neuron to burst when a depolarizing current is applied after 2000 ms of simulation.

Between 0 and 2000 ms of simulation, there is only an applied current at a certain frequency on both the excitatory and cortical neurons. The neurons are firing in a tonic mode.

For more information about Drion et al. model, see Section B.1.
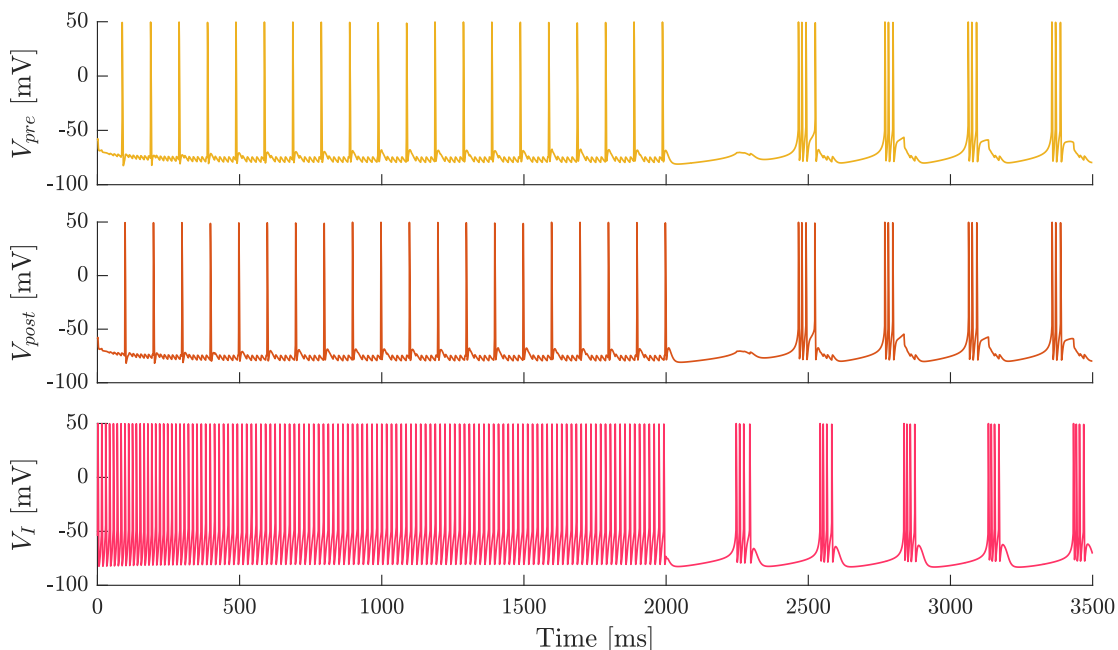
Figure 6.2 – Temporal evolution of the membrane potential for the three neurons of the ECI circuit for $\Delta t = 10ms$. The excitatory neuron is considered to be the pre-synaptic neuron and the cortical cell is the post-synaptic neuron. The frequency of stimulation in the tonic mode is 10Hz. A current is applied on the inhibitory neuron at t=2000ms, which causes a switch to a bursting mode for the three neurons.

The linear version of the calcium dynamics from (Graupner et al., 2016) was integrated into the conductance-based model. To do so, it was considered that the pre-synaptic spikes occurred when the potential of the pre-synaptic neuron (*i.e.* the neuron E) became positive. The same rule applied for spiking events from the post-synaptic neuron (C). To implement the linear version of the calcium dynamics that Graupner et al. (2016) described in their model, the parameter n appearing in equation (5.7) was set at 1. This way, $\xi = 0$ and the variation of the calcium concentration induced by the post-synaptic spike does not depend on the calcium concentration induced by the pre-synaptic spike.

Note that the non-linear version of the calcium dynamics was also implemented but it led to numerical issues. Consequently, in this thesis, the focus was made on the linear version.

The time evolution of the calcium concentration levels induced by the pre- and post-synaptic spikes is shown in Figure 6.3. It also presents the evolution of the total calcium concentration in the post-synaptic neuron and the synaptic weight evolution induced by the post-synaptic calcium level.

As explained in Section 5.1, Graupner et al. (2016) have defined a time delay D between the pre-synaptic spike and the time spent for it to impact the total Ca^{2+} concentration in the post-synaptic neuron. This parameter was considered when integrating Graupner et al. calcium-based model in the conductance-based model in such a way that the delay between the two Ca^{2+} concentration transients $delay_{pre-post} = \Delta t - D$, where Δt is the time between the pre- and post-synaptic spikes. This way, in the temporal evolution of the membrane potential for the three neurons of the circuit (Figure 6.2), one can observe that the pre-synaptic spike is followed by the post-synaptic one with a certain time delay $\Delta = 10ms$. In the temporal evolution of the calcium concentration in the post-synaptic neuron (Figure 6.3), one can observe that the Ca^{2+} concentration peaks induced by the pre- and post-synaptic spikes seem to happen almost at the same time, due to this time delay D. Indeed, since $D = 9.53709ms$, with $\Delta t = 10ms$, the Ca^{2+} transient in the post-synaptic spine induced by the pre-synaptic spike occurs only 0.46291 ms before the Ca^{2+} transient induced by the post-synaptic spike.
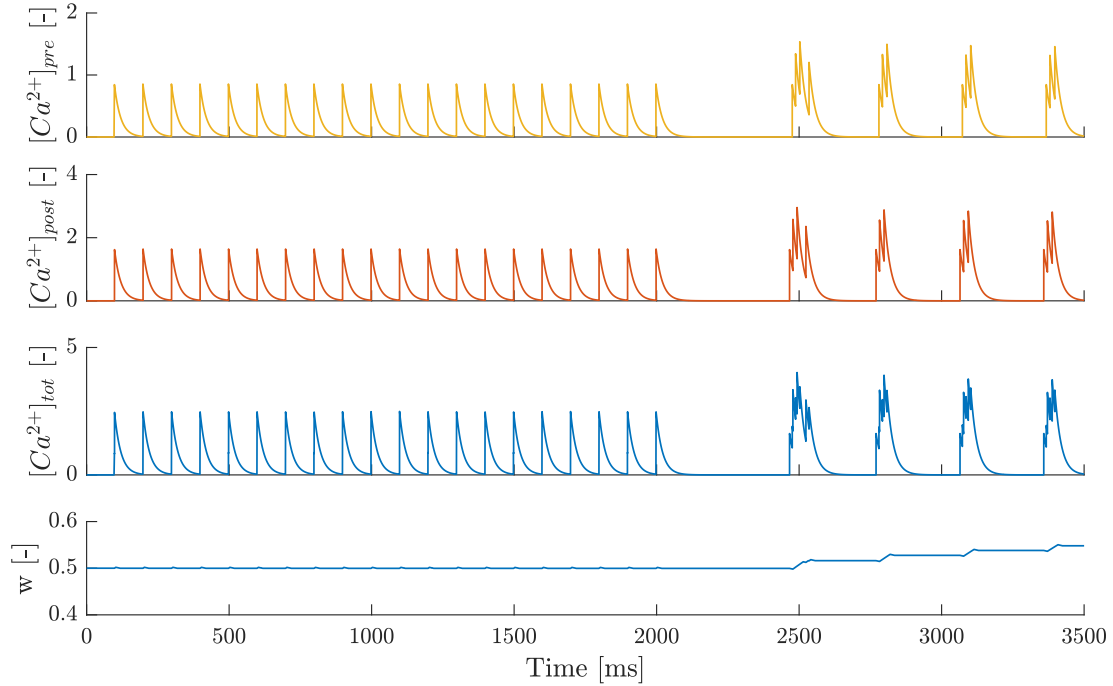
Figure 6.3 – Temporal evolution of the calcium concentration values induced by the pre- and post-synaptic spikes, C_{pre} and C_{post} respectively, the total Ca^{2+} concentration C_{tot} and the synaptic weight w, which depends on the calcium level in the post-synaptic neuron. Simulation parameters: $\Delta t = 10ms$, $f = 10Hz$ (tonic mode), tonic mode between t=0 and t=2000 ms, bursting mode between 2000 and 3000 ms.

As already explained in Section 5.1, Graupner et al. (2016) could obtain the parameter values of the calcium-based model by reproducing the protocol from Sjöström et al. (2001) to extract experimental data. It consists in presenting at a given frequency 75 spike-pairs with a fixed Δt between the pre- and post-synaptic spikes. Thanks to this protocol, Sjöström et al. observed that when the pre-synaptic spike is followed by the post-synaptic one ($\Delta t = 10ms$), it induces no changes in the synaptic weight for low frequencies but it induces LTP ($\Delta w > 0$) for higher frequencies. When the pre-synaptic spike follows the post-synaptic spike ($\Delta t = -10ms$), it induces no changes in the synaptic weight for low frequencies but it induces LTP for higher frequencies. It was possible to reproduce the evolution of the synaptic weight change depending on the firing rate of both the pre- and post-synaptic neurons, as can be seen in Figure 6.4.
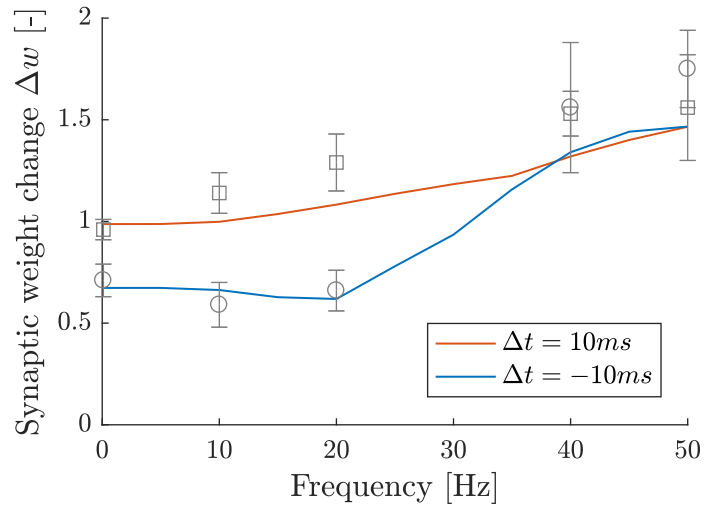
Figure 6.4 − Synaptic weight $\Delta w = w/w_0$ as function of the spike-pair presentation frequency. The pairs of synaptic spikes with $\Delta t = 10ms$ between the pre- and post-synaptic spikes is shown in red while the pairs with $\Delta t = -10ms$ (pre- after the post-synaptic spike) is shown in blue. The plot was obtained by including Graupner et al. calcium-based model into the conductance-based model from Drion et al. (2018). The experimental data from Sjöström et al. (2001) is represented in grey (square: $\Delta t = 10ms$, circle: $\Delta t = -10ms$).

6.2 Reproducing Graupner et al. (2016) with physiological calcium concentrations evolution

As a reminder, the calcium influx that drives the synaptic changes in the post-synaptic neuron originates from VDCCs and NMDARs, as shown in Figure 6.5
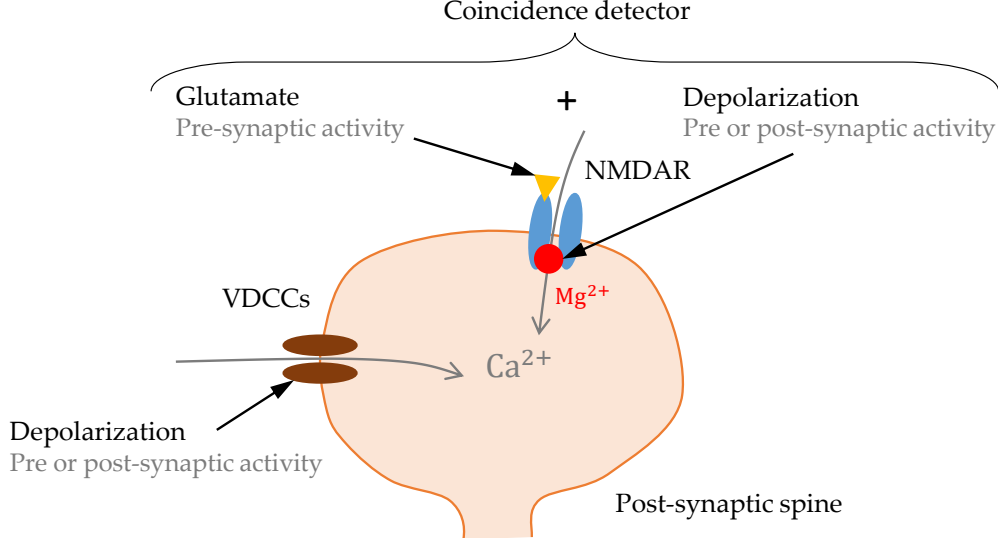
Figure 6.5 – Calcium influx into the post-synaptic neuron originates from the VDCCs and the NMDARs. The VDCCs open and let Ca^{2+} ions pass through them if the post-synaptic neuron is depolarized. The NMDARs are open if glutamate has bound to them (thanks to the pre-synaptic spike) and if the post-synaptic neuron is depolarized. Adapted from Graupner (2020).

In their model, Graupner et al. (2016) assumed that pre-synaptic (resp. post-synaptic) spikes lead to calcium influx through NMDARs (resp. VDCCs). However, the calcium concentration fluctuations modeled by Graupner et al. are represented by a single exponential decaying trace.

The contribution of this thesis is to change this trace by implementing a calcium dynamics in a more physiological way.

To do so, equations describing the calcium fluctuations through NMDARs and VDDCs are considered. Moreover, instead of having a spike timing that governs the Ca^{2+} fluctuations, the membrane potential of both the pre- and post- synaptic neurons is taken into account by integrating those equations into the conductance-based model.

Calcium fluctuations through NMDARs

The equation (5.3) from Graupner et al. (2016) describing the Ca^{2+} transient in the post-synaptic spine induced by the pre-synaptic spike is replaced by the following:

$$\frac{dc_{pre}}{dt} = \frac{1}{\tau_{Ca,NMDA}} \left(-C_{pre} + \zeta_{Ca,I_{NMDA}} I_{NMDA}^{Ca} \right) \tag{6.4}$$

Where $\tau_{Ca,NMDA}$ is the time constant of the calcium decay through NMDARs and $\zeta_{Ca,I_{NMDA}}$ is the *current-to-concentration factor*.

I_{NMDA}^{Ca} is the Ca^{2+} current through the NMDARs. This current is due to two things: the bond of glutamate on NMDARs and the depolarization of the post-synaptic neuron. It is thus described by the following equation:

$$I_{NMDA}^{Ca} = g_{NMDA} \cdot s_{NMDA}(V_{pre}) \cdot (V_{post} - V_{Ca}) \cdot MgB(V_{post}) \tag{6.5}$$

Where

- g_{NMDA} is the conductance value of the NMDAR;

- $s_{NMDA}(V_{pre})$ models the NMDAR current kinetics, which depends on the pre-synaptic potential. It reflects the dependence of the NMDAR activation to the binding of glutamate, which release by the pre-synaptic neuron was due to the pre-synaptic spike. It is described by the following equation, with $Tm(V)$ an activation function depending on the pre-synaptic potential (see eq. (B.11) in Section B.1):

$$\dot{s}_{NMDA}(V_{pre}) = 0.072 \cdot Tm(V_{pre}) \cdot (1 - s_{NMDA}) - 0.0066 \cdot s_{NMDA} \tag{6.6}$$

- V_{Ca} is the reversal potential of the Ca^{2+} ions (see Table A.1). The difference $(V_{post} - V_{Ca})$ reflects the driving force of the Ca^{2+} flow inside the post-synaptic neuron;

- $MgB(V_{post})$ describes to dependence of the Mg^{2+} blockade of the NMDARs on the post-synaptic membrane potential. It is described by the following:

$$MgB(V_{post}) = \left(1 + \frac{[Mg]_o exp(-0.062V)}{3.57}\right)^{-1} \tag{6.7}$$

The equation of $MgB(V_{post})$ is discussed in Section 6.2.1.

The influence of the NMDARs kinetics on the post-synaptic voltage V_{post} is also taken into account. Indeed, when glutamate binds to the NMDARs, it allows the flow of Na^+ ions into the post-synaptic neuron. This entry of positive ions increases the post-synaptic neuron potential, leading to the removal of the Mg^{2+} blockade. This removal allows the flow of Ca^{2+} ions into the neuron, leading to a change of V_{post} so the term $MgB(V_{post})$ also influences V_{post} itself. This phenomenon adds a new current to consider in the evolution of V_{post}:

$$C\frac{dV_{post}}{dt} = I_{app} - \sum_i I_{ion,i} - I_{NMDA_{induced}} \tag{6.8}$$

$$= I_{app} - \sum_i I_{ion,i} - (g_{NMDA} \cdot s_{NMDA}(V_{pre}) \cdot (V_{post} - V_{Ca}) \cdot MgB(V_{post})) \tag{6.9}$$

Where

- I_{app} is the applied current and $I_{ion,i}$ is the current of the ion i through the post-synaptic membrane. Eq. (6.8) corresponds to the eq. (6.1) from Drion et al. model where the influence of the NMDARs is considered with the term $I_{NMDA_{induced}}$;

- The membrane conductance C=1 $\mu F/cm^2$ (from Drion et al. conductance-based model, see Section B.1);

- $g_{NMDA} = 0.09$ is the conductance value of the NMDARs. Its value has been set according to literature (Bazhenov et al. (2002), Wei et al. (2016)) and regarding the order of magnitude of the AMPARs conductance values from the conductance-based model (see Section B.1). Indeed, it is assumed that both AMPARs and NMDARs conductance values are about the same order of magnitude. This way, a pre-synaptic spike does not necessarily generate a post-synaptic spike, it is possible to only have an EPSP.

Calcium fluctuations through by VDCCs

The calcium concentration transients induced by the post-synaptic spikes are assumed to be due to the Ca^{2+} influx through VDCCs, in particular the T-type calcium channels. Indeed, the depolarization of the post-synaptic membrane potential allows the opening of those channels and thus the flow of Ca^{2+} ions. The equation (5.4) from Graupner et al. (2016) describing those calcium transients is thus replaced by the following:

$$\frac{dc_{post}}{dt} = \frac{1}{\tau_{Ca,ICaT}}\left(-\zeta_{Ca,ICaT} \cdot I_{CaT} - C_{post}\right) \tag{6.10}$$

Where $\tau_{Ca,ICaT}$ is the time constant of the calcium decay through T-type channels, $\zeta_{Ca,ICaT}$ is the current to concentration factor for the T-type current. I_{CaT} is the T-type calcium current and is described by $I_{CaT} = \bar{g}_{Ca,T} m^3_{Ca,T} h_{Ca,T} (V_m - V_{Ca})$ (see Drion et al. model equations, Section B.1). The equation (6.10) replaces the eq. (6.3) in the conductance-based model for the post-synaptic neuron only. The Ca^{2+} fluctuations for the other neurons (E and I) are still described by eq. (6.3) from Drion et al. model.

Protocol followed to find the parameters of the physiological calcium model

Graupner et al. (2016) fitted the parameters involved in their model based on experimental data. It was thus decided to tune the parameters appearing in the physiological calcium model to fit the concentrations values that Graupner et al. had. Indeed, it seemed logical to do that since they could get very precise values of the concentration thresholds to induce potentiation or depression, implied in the computation of the synaptic weight changes.

The naive method was to tune the parameters $\tau_{Ca,ICaT}$, $\zeta_{Ca,ICaT}$, $\tau_{Ca,NMDA}$ and $\zeta_{Ca,NMDA}$ in order to get the same peak values of the concentrations as Graupner et al. (2016) on the tonic mode. The values of $\tau_{Ca,ICaT}$ and $\tau_{Ca,NMDA}$ were determined according to physiological values found in the literature (Kuo et al. (2011), Rossier (2016), Perez-Reyes (2003), Evans et al. (2012)). The other parameters were determined in order to have the same concentration peak values as Graupner et al.. Moreover, a **visual inspection** was made to verify the general shape of the calcium transients. The parameter values are given in Table 6.1.

Parameter	Unit	Value
$\tau_{Ca,ICaT}$	ms	10
$\zeta_{Ca,ICaT}$		0.16793
$\tau_{Ca,NMDA}$	ms	25
$\zeta_{Ca,NMDA}$		3.14524

Table 6.1 – Values of the parameters used in the equations describing the physiological calcium concentration evolution.
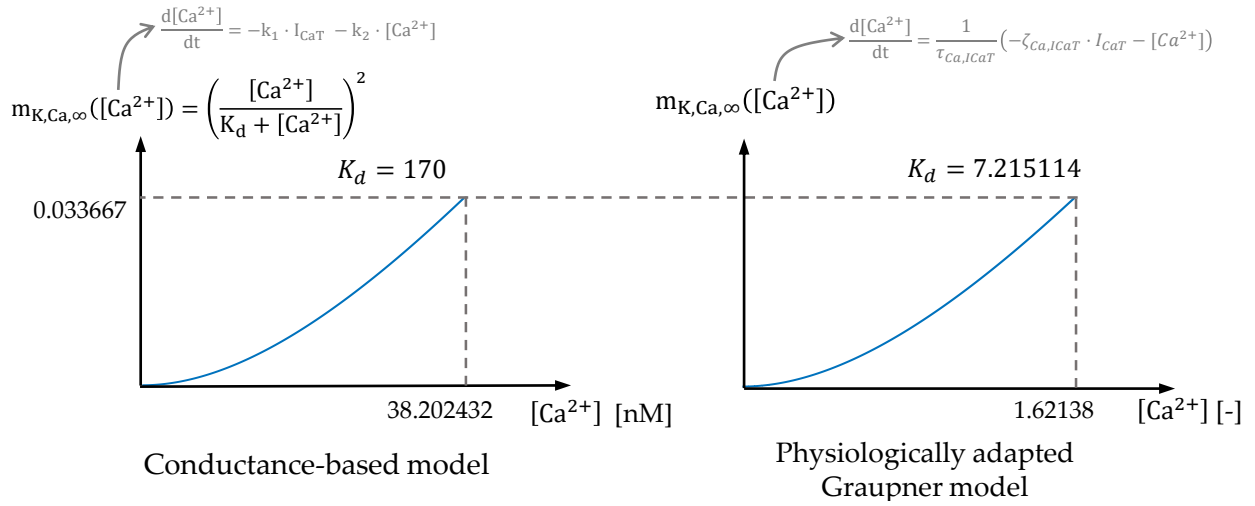
However, this led to an issue: since the concentrations were scaled with the ones from Graupner et al. (2016), they were too small for the conductance-based model. Indeed, the range of values in the model of Graupner et al. (2016) is between 0 and 1.62138 (Figure 6.6, left). In Drion et al. model, the physiological calcium concentration through the T-type Ca^{2+} channels fluctuates between 0 and 38.20243 nM (Figure 6.6, right). This way, the model has been adapted. The scaling on the concentration values was performed only on the post-synaptic neuron.
After that, it was noticed that the post-synaptic neuron could not encounter a bursting mode. This was due to the fact that the parameter K_d, which is the semi-activation factor of the calcium-activated potassium current I_{KCa} (see eq. (6.2)) was not scaled. If the calcium concentration level in the post-synaptic neuron is not high enough, it does not activate the K$^+$ current which allows the hyperpolarization of the cell, thus making the switch to the bursting mode of the neuron impossible.

This way, the K_d parameter was scaled to the correct range of concentration values and it was set at $K_d = 7.2151147$ (only for the post-synaptic neuron), as shown in Figure 6.6.

Results

A temporal simulation of this physiological model was performed, with $\Delta t = 10ms$ (time lag between the pre- and post-synaptic spikes). In Figure 6.7, the temporal evolution of the membrane potential is presented, for the three neurons involved in the circuit. One can observe that, compared to Figure 6.2, the change of the calcium equations did not change a lot the temporal course of the membrane potential. We still have bursts of action potentials from the pre-synaptic and the inhibitory neuron.

$$m_{K,Ca,\infty}([Ca^{2+}]) = \left(\frac{[Ca^{2+}]}{K_d + [Ca^{2+}]}\right)^2$$

$$\frac{d[Ca^{2+}]}{dt} = -k_1 \cdot I_{CaT} - k_2 \cdot [Ca^{2+}]$$

$K_d = 170$

0.033667

38.202432 $[Ca^{2+}]$ [nM]

Conductance-based model

$$m_{K,Ca,\infty}([Ca^{2+}])$$

$$\frac{d[Ca^{2+}]}{dt} = \frac{1}{\tau_{Ca,ICaT}}(-\zeta_{Ca,ICaT} \cdot I_{CaT} - [Ca^{2+}])$$

$K_d = 7.215114$

1.62138 $[Ca^{2+}]$ [-]

Physiologically adapted
Graupner model

Figure 6.6 – Schematic of the scaling made on the parameter K_d. The goal was to keep the same equation to describe the calcium-activated potassium channel with different ranges of concentration values.

However, the post-synaptic neuron shows a burst of action potentials that are further away one from the other.
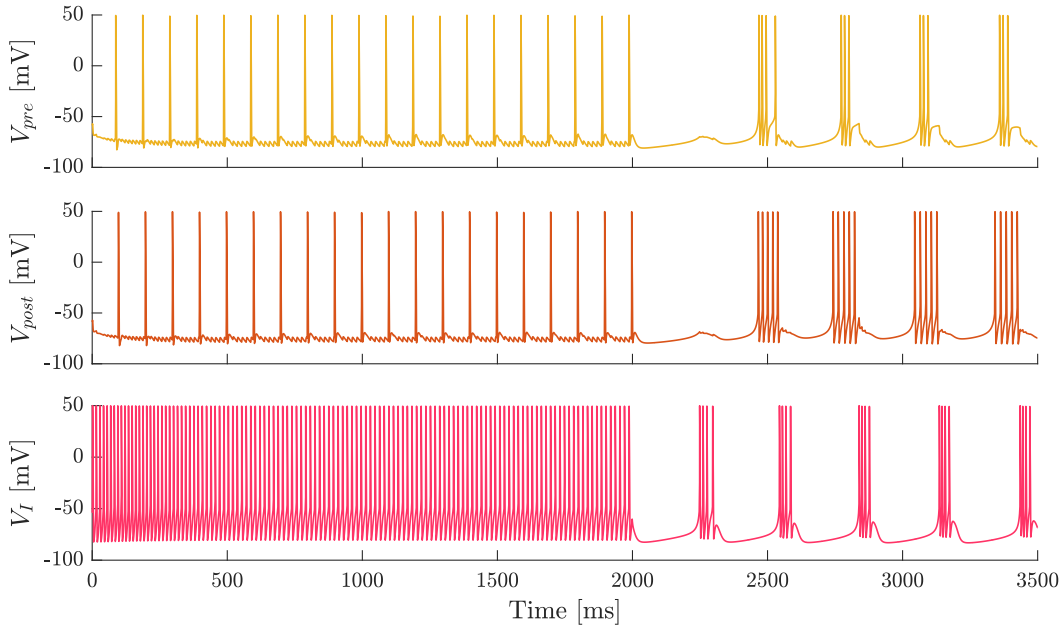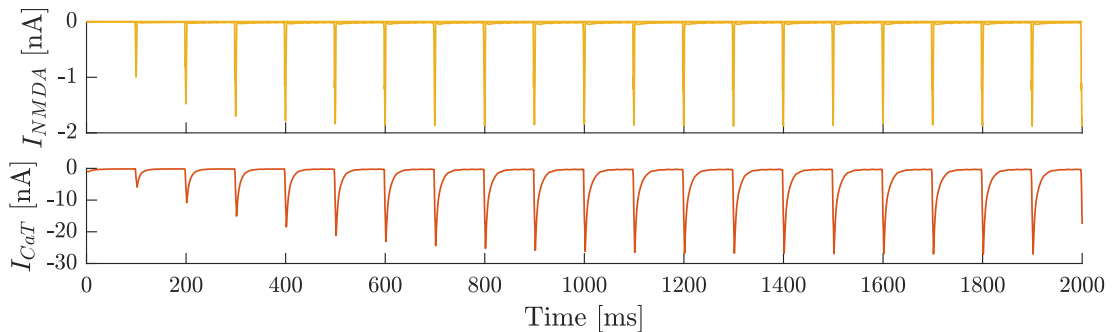

Figure 6.7 – Temporal evolution of the membrane potential for the three neurons of the ECI circuit, with $\Delta t = 10ms$, $f = 10Hz$. A current is applied on the inhibitory neuron at t=2000 ms, which causes the neurons to encounter a bursting pattern. The calcium dynamics of the post-synaptic neuron follows the physiological modeling and the parameters K_d has been scaled for this neuron only.

The temporal evolution of the calcium transients induced by the pre- and post-synaptic spikes, described in a physiological way, is presented in Figure 6.8. One can observe that the steady-state is not attained immediately for the physiological model. There is a transitory phase in the calcium evolution at the beginning of the temporal simulation where the increase of the calcium concentration peaks is progressive. Indeed, when looking at the temporal evolution of I_{CaT} and I_{NMDAR}, one can see that those currents also take some time to attain their stationary value. For I_{NMDAR}, as time goes by and the spikes follow one another, the glutamate continues to bind to the NMDARs and do have the time to be removed from all the receptors between two successive spikes. This way, as time goes by, there are more and more NMDARs activated by the binding of the glutamate. There is thus more

Ca^{2+} current passing through the NMDARs. The principle that explains the transitional phase with I_{CaT} is the same. As time goes by, the T-type Ca^{2+} channels do not have the time to close between two successive depolarizations of the post-synaptic membrane. It is due to the fact that the inactivation gate kinetics is more slower than the activation gate kinetics. For more information about the T-type Ca^{2+} channel, see Section A.4.
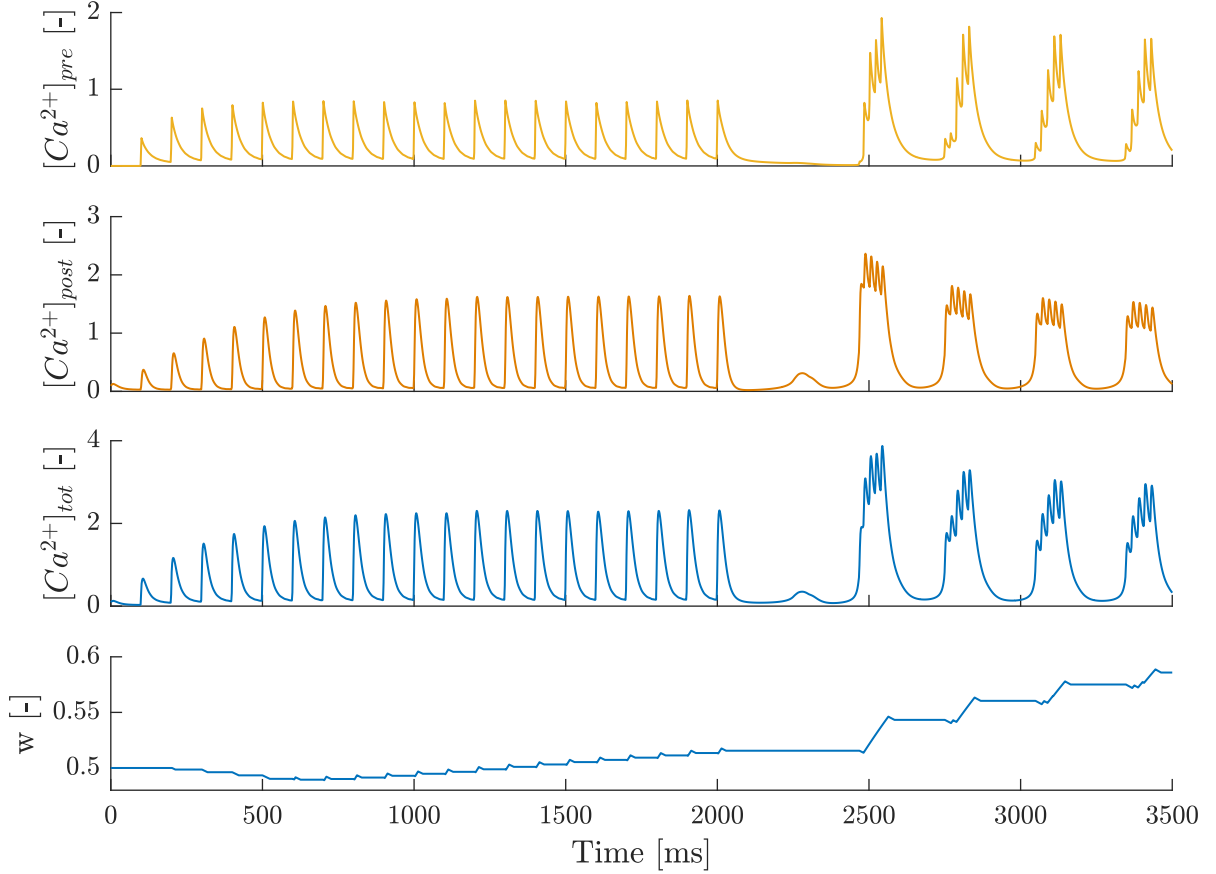
Figure 6.8 – Temporal evolution of the calcium concentration transients induced by the pre-($[Ca^{2+}]_{pre}$, in yellow) and post-synaptic ($[Ca^{2+}]_{post}$, in orange) spikes, the total calcium transient ($[Ca^{2+}]_{tot}$, in blue) and the synaptic weight change. Those Ca^{2+} concentrations evolution correspond to the voltage simulation presented in Figure 6.7.
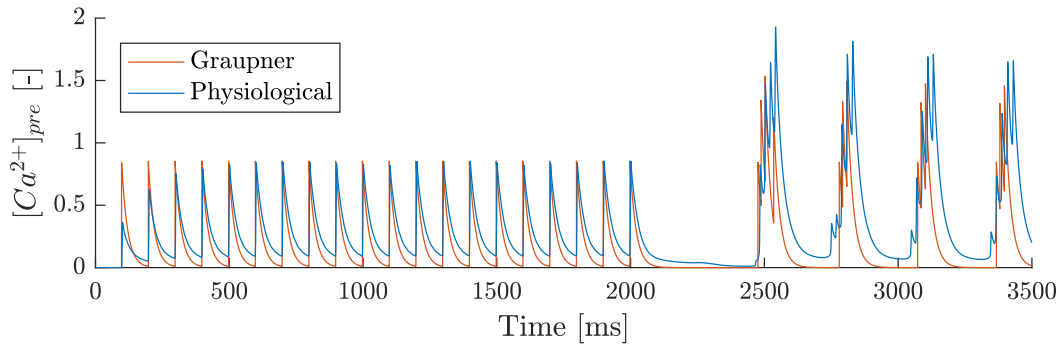

Figure 6.9 – Temporal evolution of the currents I_{NMDAR} (top) and I_{CaT} (bottom) corresponding to the voltage simulation presented in Figure 6.7.

The comparison between the model from Graupner et al. (2016) and the physiological one for the temporal evolution of the calcium concentration induced by the pre- and post-synaptic spikes is shown in Figures 6.10 and 6.11. Figures 6.12 and 6.13 compare the total post-synaptic Ca^{2+} concentration

and the induced changes in the synaptic weight for both the physiological and Graupner et al. models.

Figures 6.10 to 6.13 present the comparison of the calcium transients for both the calcium-based model from Graupner et al. (2016) and the physiological one. Because of the transitory phase in the calcium evolution at the beginning of the temporal simulation, the synaptic weight decreases with the physiological model in the first 700 ms. Then, the synaptic weight increases more than with the model from (Graupner et al., 2016), simply because the kinetics of the calcium ions from the NMDARs is slower so the total Ca^{2+} concentration decreases less rapidly.

In Figure 6.11, it is possible to observe that the calcium elevation in the bursting phase (after 2000ms of simulation) due to the post-synaptic spike is lower with the physiological model than with the calcium-based model from Graupner et al. (2016). In Figure 6.10, one can see that the increase of calcium due to the pre-synaptic spike is slightly higher with the physiological model. This counter-balances the observation made in Figure 6.11 and the total calcium concentration peaks have almost the same height for both models. However, still because of the fact that the physiological dynamics is slower, the total Ca^{2+} concentration takes more time to decrease so the synaptic weight increases more with the physiological model.
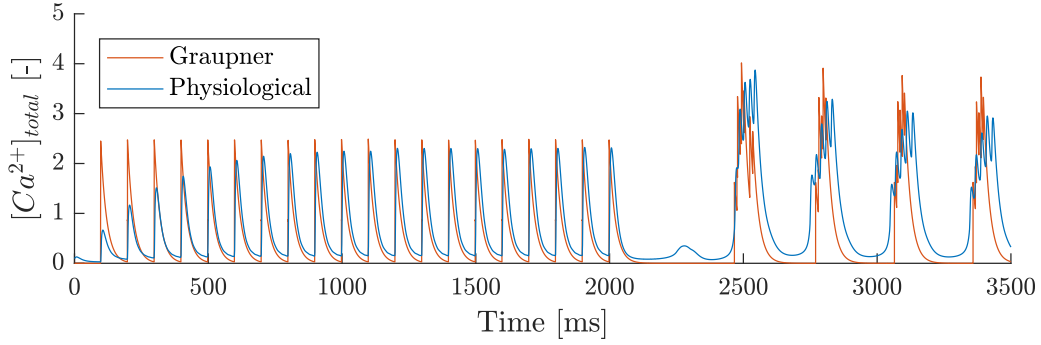

Figure 6.10 – Temporal evolution of the post-synaptic calcium concentration induced by the pre-synaptic spike C_{pre}. For the physiological concentration evolution, it corresponds to the Ca^{2+} entering the post-synaptic neuron through NMDARs. The simulation corresponds to one presented in Figure 6.7.
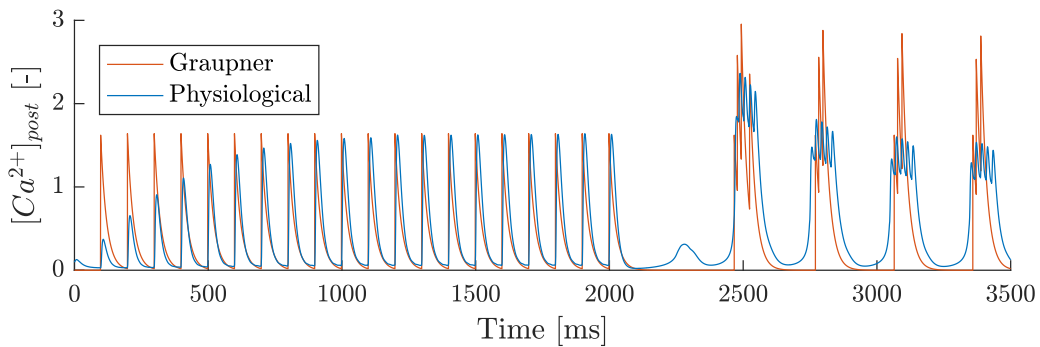
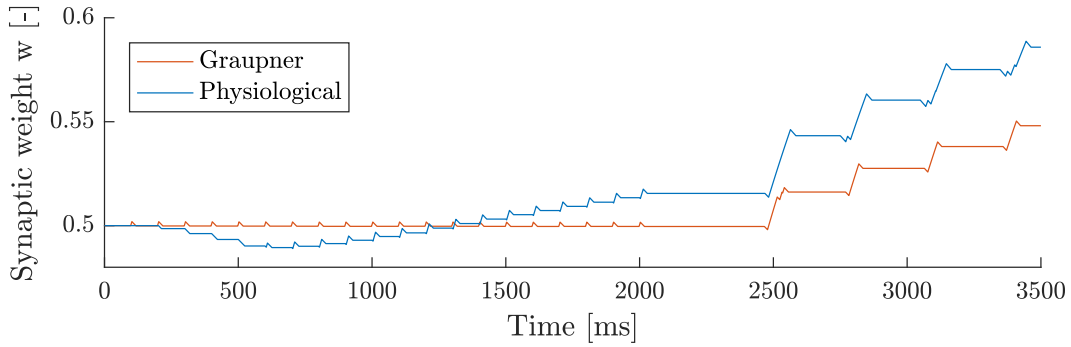**Figure 6.11** – Temporal evolution of the post-synaptic calcium concentration induced by the post-synaptic spike C_{post}. For the physiological concentration evolution, it corresponds to the Ca^{2+} entering the post-synaptic neuron through VDCCs, in particular the T-type calcium channels. The voltage simulation corresponds to one presented in Figure 6.7.

One thing that was also noticed while searching for the parameter values is the fact that the peak value of the Ca^{2+} concentration induced by the pre- and post-synaptic spike is oscillating. Those oscillations can also be noticed in the currents I_{NMDA} and I_{CaT} (see Figure 6.9). This is simply due to the fact that the membrane potential of both the pre- and post-synaptic neurons directly influences

Figure 6.12 – Temporal evolution of the total post-synaptic calcium concentration induced by the pre- and the post-synaptic spikes, *i.e.* $c(t) = C_{pre}(t) + C_{post}(t)$. The voltage simulation corresponds to one presented in Figure 6.7.


Figure 6.13 – Temporal evolution of the synaptic weight due to the total calcium transients in the post-synaptic neuron. The voltage simulation corresponds to one presented in Figure 6.7.

the current of ions passing through the membrane. Since the Ca^{2+} concentrations depend directly on those currents, the oscillations of the currents are reflected in the concentration evolution.

For low frequency values, it is more difficult to observe those observations. However, at higher frequencies, it can be easily observed, as shown in Figure 6.14, where $f = 40Hz$. In this Figure, only the oscillations for the calcium peaks induced by the pre-synaptic spike are highlighted. The same phenomenon occurs for the calcium transients induced by the post-synaptic spike but the effects are less visible. This way, the parameter values were fitted on one concentration peak but it is important to know that the Ca^{2+} concentration peak values can vary, in general in an interval of $\pm 2.5\%$.

While Graupner et al. (2016) described a Ca^{2+} concentration evolution that is regular and precise, here the concentration peaks are thus oscillating. This is not a problem a priori since the model is supposed to be physiological and the calcium fluctuations are probably not that regular in real conditions.
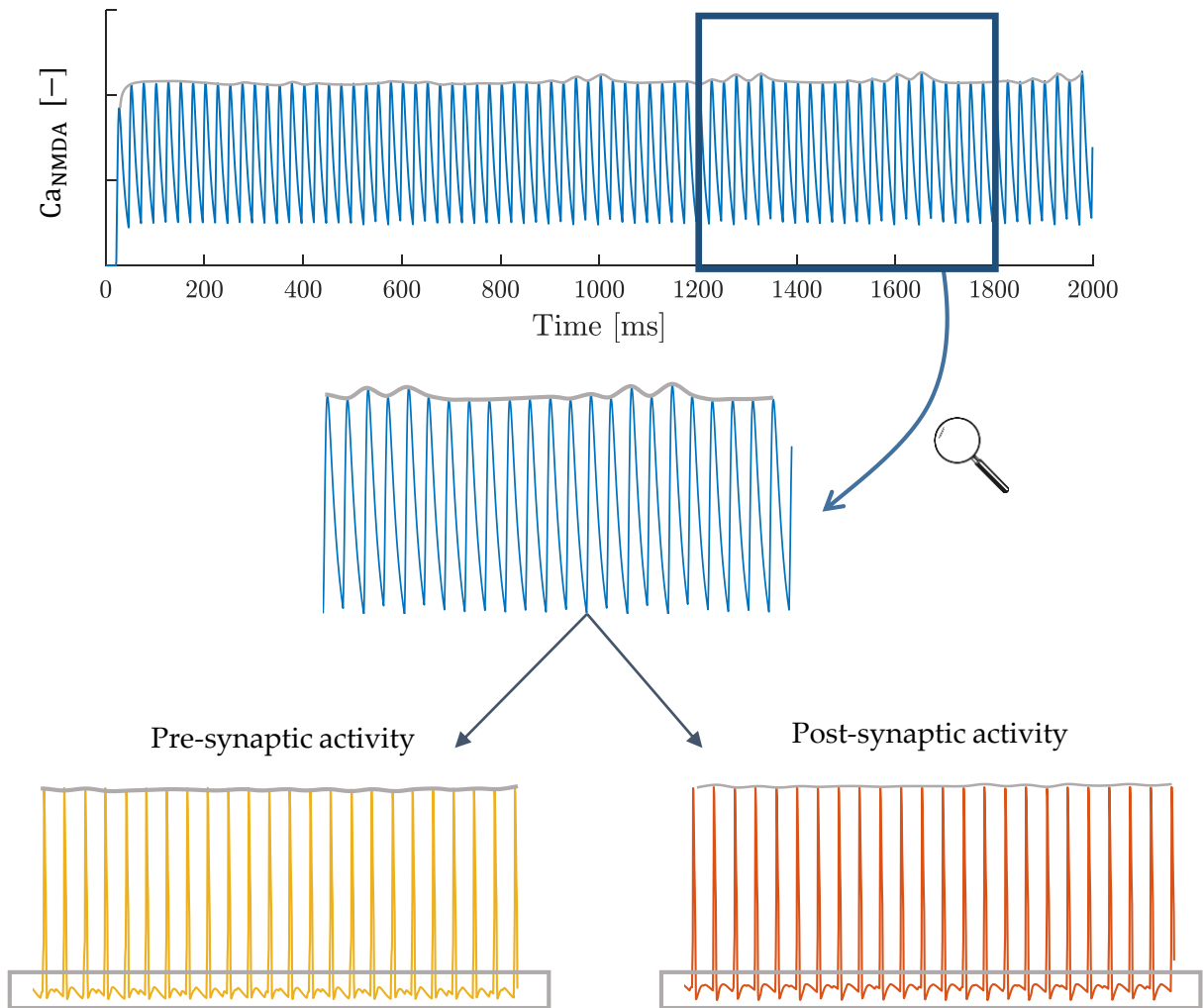
Figure 6.14 – Illustration of the influence of the pre- and post-synaptic activities on the calcium through NMDARs, with a frequency of 40Hz and $\Delta t = 10ms$. Small oscillations in the membrane potential lead to larger oscillations on the currents of ions passing through the membrane, which directly impacts the calcium concentration evolution.

6.2.1 Influence of the NMDAR magnesium blockade equations

Another term that influences the calcium concentration transients induced by the pre-synaptic spikes is the dependence of the Mg^{2+} blockade on the Ca^{2+} influx through NMDARs. In the literature, there exist different forms of the equation that describes the term $MgB(V)$.

Evans et al. (2012) defines this dependence by the following equation, where the parameter B depends on the considered subunit of the NMDAR channel:

$$\frac{1}{1 + [Mg^{2+}] \cdot exp\left(\frac{-V_{post}}{B}\right)} \tag{6.11}$$

To have an idea of the impact of changing this equation describing the Mg^{2+} blockade dynamics, two different equations have been tested:

$$MgB(V) = \frac{1}{1 + \frac{[Mg]_o exp(-0.08V)}{3.57}} \tag{6.12}$$

$$MgB(V) = \frac{1}{1 + \frac{[Mg]_o exp(-0.062V)}{3.57}} \tag{6.13}$$

The difference between the equations (6.12) and (6.13) is the value of the exponential decay, as shown in Figure 6.15 (left). Indeed, eq. (6.12) leads to a faster increase of the value of MgB, for the same variation of the potential. It thus reflects the fact that the Mg^{2+} blockade will be removed faster than the eq. (6.13).

The temporal evolution of C_{pre} is shown in Figure 6.15 (right) for both equations (6.12) and (6.13). As expected, the kinetics of the calcium concentration induced by the pre-synaptic spike is faster with eq. (6.12). It is due to the fact that the Mg^{2+} blockade is removed more rapidly when the post-synaptic potential increases and is also put back on more rapidly when the potential decreases.
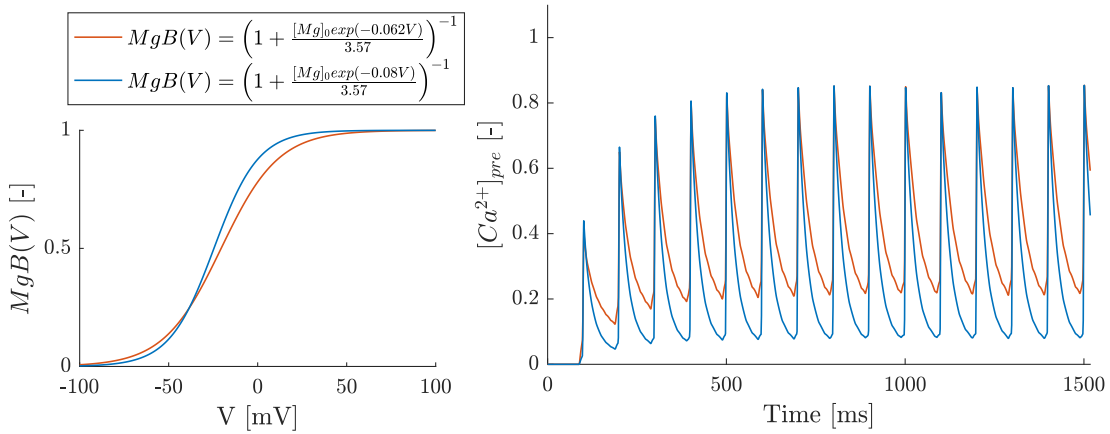
Figure 6.15 − Effects of the equation describing the dependence of the Mg^{2+} blockade on the post-synaptic potential. **Left:** Comparison of the different curves describing $MgB(V)$. **Right:** comparison of the calcium concentration transients induced by pre-synaptic spikes for two different equations describing $MgB(V)$.

The parameter B is thus a parameter that can shift the $MgB(V)$ curve and in consequence the rate of removal of the Mg^{2+} blockade.

In the context of this Master's thesis, the equation (6.12) was used.

6.3 Reproducing the $\Delta w(f)$ curve from Graupner et al. (2016)

Once the concentrations were adapted in a more physiological way, the next step was to try to reproduce the $\Delta w(f)$ curve that Graupner et al. (2016) obtained (see Figure 6.4), based on experimental data. To reproduce this curve, the protocol from Sjöström et al. (2001) was followed. It consists in presenting 75 spike pairs with a given frequency and a given time lag between the pre- and post-synaptic spikes, as represented in Figure 6.16. Sjöström et al. observed experimentally at small frequencies that the synaptic weight does not change with $\Delta t > 0$ while there is a depression with $\Delta t < 0$. For higher frequencies, the synaptic weight increases in both cases, there is potentiation.
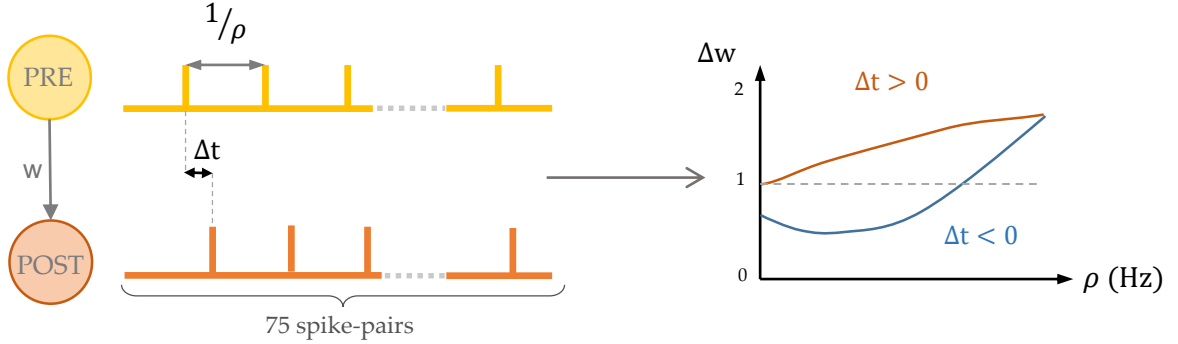
Figure 6.16 – Illustration of the protocol from Sjöström et al. (2001) adapted by Graupner et al. (2016). For a given frequency ρ and time lag between the pre- and post-synaptic spikes Δt, 75 spike-pairs are presented (right). Sjöström et al. observed that a $\Delta t > 0$ leads to no changes at low frequencies and potentiation at high frequencies. A value of $\Delta t < 0$ leads to a depression for low frequencies and potentiation at high frequencies (left).

6.3.1 Experiment 1: Directly from the physiological equations

**Protocol followed to reproduce Sjöström et al. (2001)**

The first naive method that is used to try to get the $\Delta w(f)$ curve directly by reproducing the experimental protocol from Sjöström et al. (2001) with the physiological model described in Section 6.2. For this physiological model, it is needed to consider the fact that the concentration transients induced by the pre- and post-synaptic spikes take some time to stabilize (see Figures 6.10 and 6.11). To take into account this transitory phase for the construction of the $\Delta w(f)$ curve, the evolution of $\Delta w = w/w_0$ is not changed until 15 spikes pairs after the beginning of the temporal simulation.

Results

The Figure 6.17 presents the $\Delta w(f)$ curves for $\Delta t = 10ms$ (red) and $\Delta t = -10ms$ (blue) for the parameters from Table 6.1. It is possible to observe that, compared to what Graupner et al. (2016) obtained (see Figure 6.4), the global shape is incorrect for both curves. Indeed, for small frequencies, there is only potentiation for both values of Δt while there was supposed to be depression for $\Delta t = -10ms$ and no changes of w for $\Delta = 10ms$, according to Sjöström et al. (2001). For higher frequencies, both curves represent potentiation but the synaptic weight changes are smaller than what is observed with experimental data.

Issues

It was noticed that changing the time lag Δt between the pre- and post-synaptic spikes changes the shape of the calcium concentration induced by the pre- and post-synaptic spikes, as can be observed in Figures 6.18 and 6.19. It is due to the fact that Graupner et al. (2016) neglected the influence of the post-synaptic potential on the Mg^{2+} blockade, which affects the NMDARs kinetics.
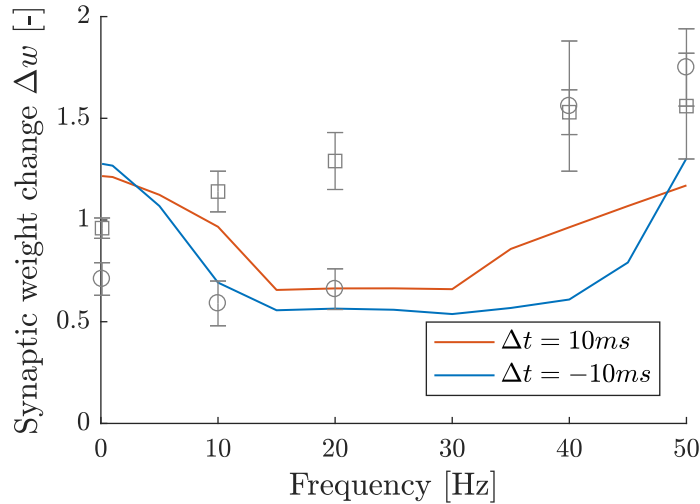
Figure 6.17 – Experiment 1. Synaptic weight change $\Delta w = w/w_0$ as function of the firing rate of the pre- and post-synaptic spikes for a physiological calcium dynamics. Δt is the time lag between the pre- and post-synaptic spikes. The experimental data from Sjöström et al. (2001) is represented in grey (square: $\Delta t = 10ms$, circle: $\Delta t = -10ms$).

Indeed, a pre-synaptic spike causes the release of glutamate which binds to the NMDARs, allowing their activation and thus the entry of Na^+ ions into the post-synaptic neuron. This entry of positive ions increases the post-synaptic membrane potential V_{post}, reflected by eq. (6.9). This increase of V_{post} directly has an impact on the calcium concentration in the post-synaptic neuron since it allows the flow of Ca^{2+} ions into it through T-type Ca^{2+} channels. This explains what is observed in Figure 6.19.

The increase of V_{post} due to the activation of NMDARs after the pre-synaptic spike (reflected by the $s_{NMDA}(t)$ term in eq. (6.9)) removes the Mg^{2+} blockade from the NMDARs. Ca^{2+} ions can then enter inside the post-synaptic neuron through NMDARs. This explains the small and slow increase of the calcium concentration caused by the pre-synaptic spike seen in Figure 6.19. Then, a post-synaptic spike follows the pre-synaptic one, it increases the membrane potential of the post-synaptic neuron. This elevation also results in the removal of the Mg^{2+} blockade and can Ca^{2+} enter the post-synaptic spine. The depolarization induced by the post-synaptic spike is larger than the one induced by the flow of Na^+ ions into the neuron. This explains how a larger peak of calcium follows a smaller one in Figure 6.19.

This impact of the post-synaptic potential of the NMDARs kinetics could not be clearly observed when the equations of the evolution of the physiological Ca^{2+} concentration were first introduced (see Figure 6.10). This was due to the fact that the temporal simulations were conducted with a time lag between the pre- and post-synaptic spikes set at 10 ms. This way, considering the delay D that Graupner et al. used in their model to reflect the waiting time of the pre-synaptic spike to impact the NMDARs dynamics, the pre- and post- spikes were temporally close to each other. The peaks of Ca^{2+} concentration elevation in the post-synaptic spine were thus superimposed and mistaken as a single peak.

Note that one can also observe on Figure 6.18 that there exist small oscillations of the calcium concentration through NMDARs, in the ascending phase due to the pre-synaptic spikes. Those are due to the oscillations of the potential values of the pre- and post-synaptic neurons since the NMDARs kinetics depends on both neuron potential.

Solution

In order to get an appearance of the calcium concentration induced by the pre-synaptic spike similar to what Graupner et al. (2016) obtained (see Figure 6.3), it was decided to consider that the fraction of NMDARs bereft of the Mg^{2+} blockade was constant, *i.e.* $Mg(V) = cst \; \forall \; V$.
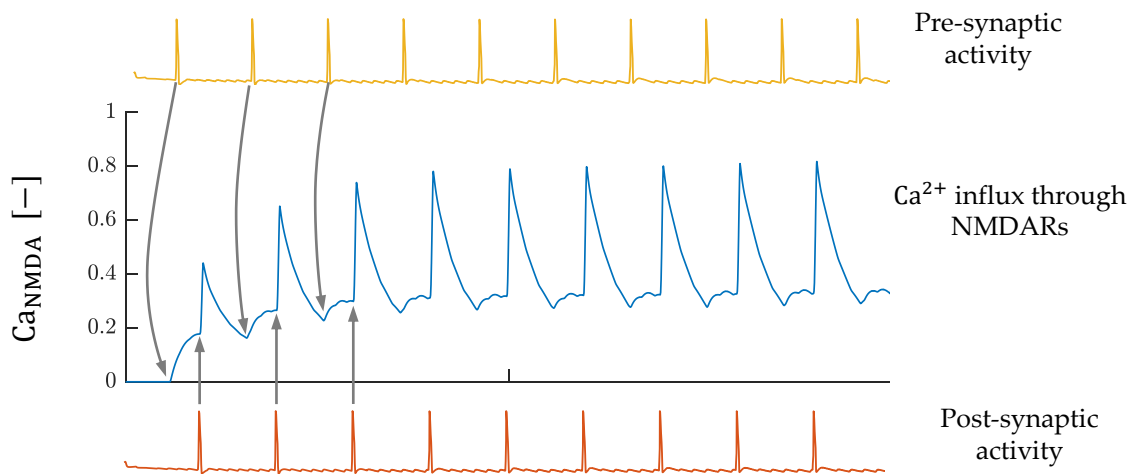
Figure 6.18 – Effect of the pre-synaptic (top) and post-synaptic (bottom) activities on the Ca^{2+} entry through NMDARs (Ca_{NMDA}, middle figure). The first small and slow increase of Ca_{NMDA} is due to the pre-synaptic spike that activates the NMDARs and slowly removes the Mg^{2+} blockade from them. The second larger peak of Ca_{NMDA} is due to the post-synaptic spike which increases the post-synaptic potential, leading to the removal of Mg^{2+} blockades and thus the flow of Ca^{2+} ions through NMDARs.
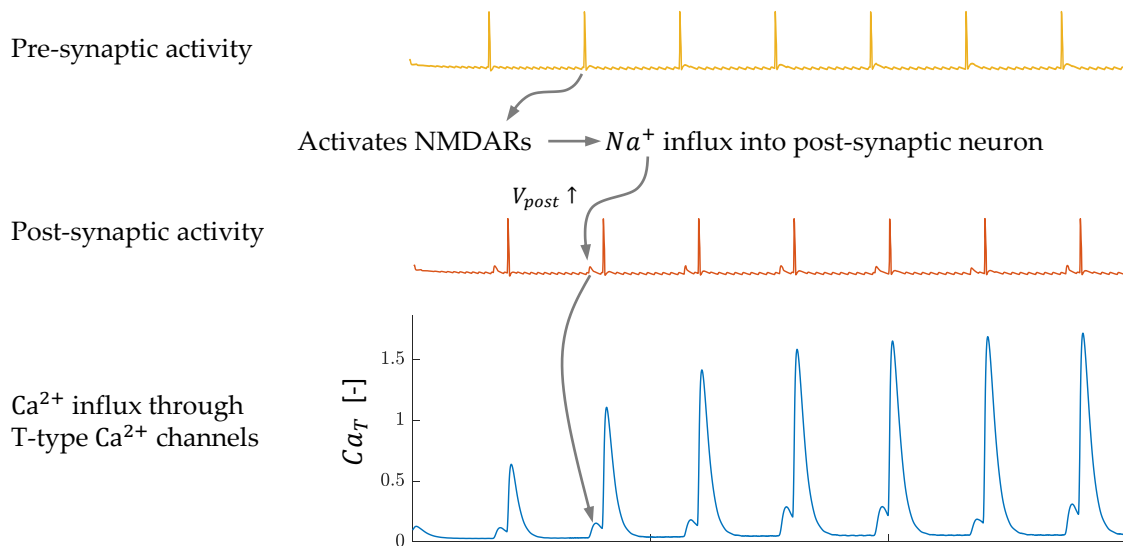
Figure 6.19 – Effect of the pre-synaptic spike on the post-synaptic membrane potential, through the activation of NMDARs. The pre-synaptic spike (top) triggers the release of glutamate from synaptic vesicles. Glutamate binds to NMDARs, which triggers their activation and Na^+ ions enter in the post-synaptic neuron. This flow of positive ions increases the post-synaptic membrane potential (middle), resulting in a flow of Ca^{2+} ions through T-type Ca^{2+} channels, increasing the post-synaptic Ca^{2+} concentration (bottom).

Two equations were modified: (6.5) and (6.9). It was considered that all the Mg^{2+} blockades were removed from the NMDARs, *i.e.* $MgB(V) = 1 \ \forall \ V$. This way, the NMDARs kinetics only depends on their activation due to the pre-synaptic activity.

Moreover, the equation (6.9) has been removed from the physiological model since Graupner et al. (2016) did not consider the fact that the NMDARs kinetics impacts the post-synaptic potential.

To summarize: Experiment 1: compute directly the Δw(f) curve with the physiological model

    ➢ Issue: Δw(f) curve not consistent with experimental data from Sjöström et al. (2001)

    ➢ Why? Mg^{2+} blockade dynamics not taken into account by Graupner et al. (2016)

    ➡ *Solution?* Remove the influence of the Mg^{2+} blockade on the NMDARs kinetics

---

6.3.2 Experiment 2: Fitting on the concentration peak values at 1Hz

Assumption

The Mg^{2+} blockade dynamics is not considered.

Protocol followed to get the parameter values of the physiological calcium model

The parameters were determined according to the Ca^{2+} concentration peak values from Graupner et al. model for a frequency of 1Hz (see Table 6.2). The parameter values were tuned by **visual inspection** Since only the equations describing the NMDARs kinetics were changed, only the value of $\zeta_{Ca,NMDA}$ was changed and the value of $\tau_{Ca,NMDA}$ did not change to respect physiological values found in the literature. The parameter values are presented in Table 6.3.

| $[\mathbf{Ca^{2+}}]_{\mathbf{pre}}$	$[\mathbf{Ca^{2+}}]_{\mathbf{post}}$
0.84410	1.62138

Table 6.2 – Concentration peak values for the calcium concentration transients induced by the pre- and post-synaptic spikes obtained from Graupner et al. (2016) with a frequency of 1Hz.

Parameter	**Unit**	**Value**
$\tau_{Ca,ICaT}$	ms	10
$\zeta_{Ca,ICaT}$		0.16793
$\tau_{Ca,NMDA}$	ms	25
$\zeta_{Ca,NMDA}$		0.39663

Table 6.3 – Values of the parameters used in the equations describing the physiological calcium concentration evolution, considering that all the Mg^{2+} blockade are removed. The current-to-concentration factors ζ were determined by fitting visually the calcium concentration peaks from Graupner et al. (2016) with a frequency of 1 Hz and the time constants τ were kept consistent with what is found in the literature (Kuo et al. (2011), Rossier (2016), Perez-Reyes (2003), Evans et al. (2012)).

Results

Figure 6.20 presents the temporal evolution of a single calcium concentration transient induced by the pre- and post-synaptic spikes and the total calcium transient. It compares what Graupner et al. (2016) could obtain and what is obtained with the physiological model.
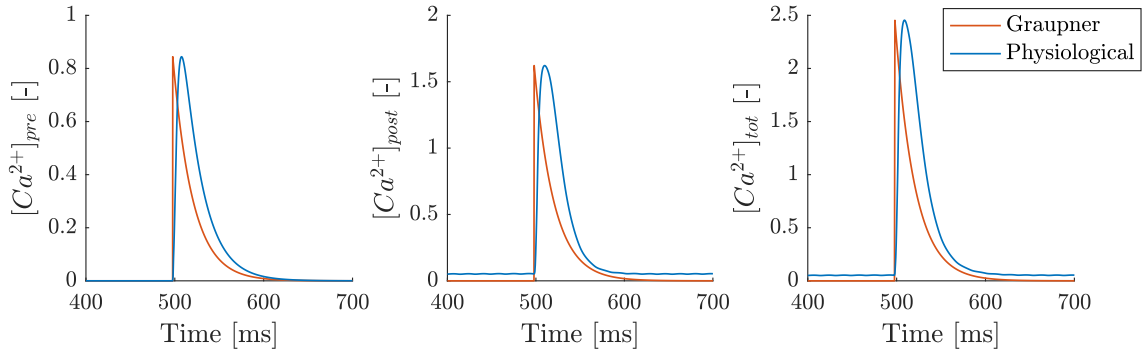
Figure 6.20 – Comparison of the calcium concentrations (C_{pre}, C_{post} and $C_{tot} = C_{pre} + C_{post}$) obtained with the model from Graupner et al. (2016) and the physiological model, considering that $MgB(V) = 1$, *i.e.* all the Mg^{2+} blockades are removed from the NMDARs.

One can observe that for both $[Ca^{2+}]_{pre}$ and $[Ca^{2+}]_{post}$ the calcium concentration peaks of the physiological model are a bit delayed with the ones from Graupner et al. (2016). It is due to the fact that they considered a simple exponential equation to describe the calcium transients while the physiological model also takes into account other factors, such as the activation of the NMDARs. For the Ca^{2+} transient induced by the pre-synaptic spike, the decreasing phase looks almost the same for both models since the parameter $\tau_{Ca,NMDA}$ was chosen to be equal to 25ms, which is close to what Graupner et al. (2016) chose in their calcium-based model (22.27212 ms).

However, for the calcium transient induced by the post-synaptic spike, one can see that the decreasing phase is a bit faster for the physiological model. It is due to the fact that Graupner et al. (2016) kept the same time constant for both types of induced calcium transients (22.27212 ms). In the physiological model, the time decay of the calcium through T-type Ca^{2+} channels has been chosen according to literature (10 ms).

Note that one can notice in Figure 6.20 that the Ca^{2+} concentration induced by the post-synaptic spike (middle graph) does not converge completely to 0 but to 0.0439. It is due to the fact that the value of I_{CaT} does not converge to 0 and the calcium concentration directly depends on it (see eq. (6.10)).

Issues

One issue was noticed when the firing rate of the pre- and post-synaptic spikes was changed. Indeed, since the parameters fitting was performed on the calcium concentration peaks that Graupner et al. (2016) for a frequency of 1 Hz, when increasing this firing rate, the values of the concentration peaks were not the same as Graupner et al. had. Figure 6.21 presents a temporal simulation of two neurons that are firing in a tonic mode with a frequency of 20 Hz. One can now clearly observe the difference of the concentration peak values for different firing rates.

Reproducing the curve $\Delta w(f)$ that Graupner et al. (2016) obtained (see Figure 6.4) was thus impossible, as shown in Figure 6.22. Referring to what Sjöström et al. (2001) observed experimentally, the curves are inverted regarding the time lag between the pre- and post-synaptic spikes. Indeed, at small frequencies, the pre-post stimulation is supposed to induce no changes in the synaptic weight w while the post-pre stimulation is supposed to induce depression, *i.e.* $\Delta w < 1$. However, for higher frequencies, both curves converge to a $\Delta w > 1$ and Sjöström et al. (2001) made the same observation experimentally.

Solution

To solve this issue, it was thought to find the parameter values of the physiological model $\tau_{Ca,NMDA}$, $\tau_{Ca,ICaT}$, $\zeta_{Ca,NMDA}$ and $\zeta_{Ca,ICaT}$ to get the same concentration peak variation for a given variation of the frequency as Graupner et al. (2016) obtained. Moreover, the two factors appearing in the equation
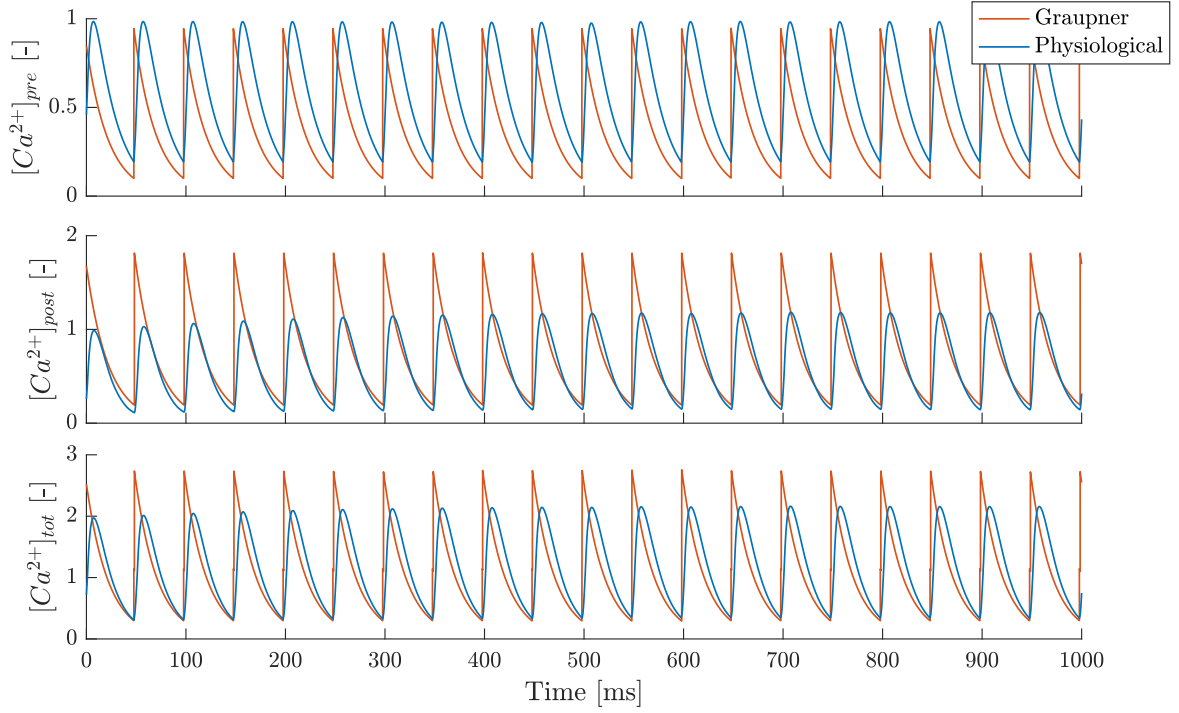
Figure 6.21 – Comparison of the calcium concentrations (C_{pre}, C_{post} and $C_{tot} = C_{pre} + C_{post}$) obtained with the model from Graupner et al. (2016) and the physiological model for a frequency of 20Hz. It is considered that $MgB(V) = 1$, *i.e.* all the Mg^{2+} blockades are removed from the NMDARs.
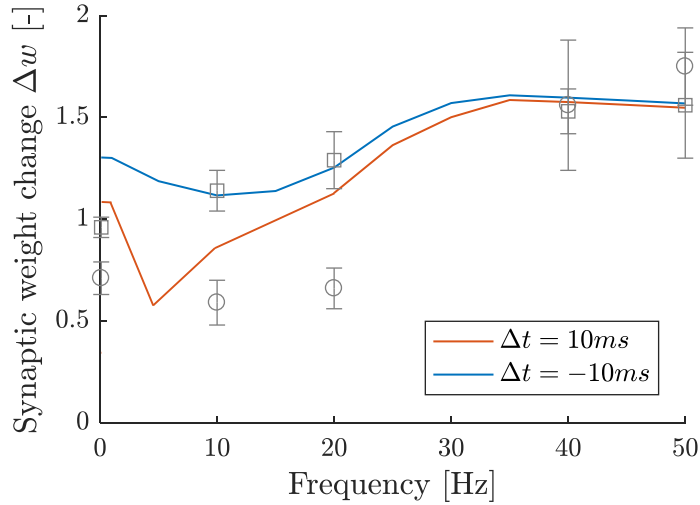
Figure 6.22 – Experiment 2. Synaptic weight changes as function of the firing rate of the spike-pairs. Δt is the time lag between the pre- and post-synaptic spikes. The experimental data from Sjöström et al. (2001) is represented in grey (square: $\Delta t = 10ms$, circle: $\Delta t = -10ms$). The plot is drawn based on the parameter values found by fitting the concentrations peak values at a frequency of 1Hz.

describing the NMDARs activation were changed (see eq. (6.6)). The parameters p_1 and p_2 were defined in the following way:

$$\dot{s}_{NMDA}(V_{pre}) = p_1 \cdot Tm(V_{pre}) \cdot (1 - s_{NMDA}) - p_2 \cdot s_{NMDA} \tag{6.14}$$

The fact that all the Mg^{2+} blockades were removed from the NMDARs (*i.e.* $MgB(V) = 1$) was still considered.

To summarize:

- ➢ Assumption: Mg^{2+} not taken into account
- ➢ Issue: Δw(f) curve not consistent with experimental data from Sjöström et al. (2001)
- ➢ Why? Overfitting of the parameters on $[Ca^{2+}]$ peak values @ 1Hz

➡ *Solution?* Find the parameters of the physiological model for at least 2 frequency values

6.3.3 Experiment 3: Fitting on the concentration peak values at 1Hz and 10Hz

Assumption

The Mg^{2+} blockade dynamics is neglected.

Protocol followed to find the parameter values of the physiological calcium model

The first used method was to find the combination of parameters that gives the correct variation of the peak concentration values for a frequency variation of 10Hz. The frequency values that were considered were 1 and 10 Hz. Referring to Graupner et al. (2016), the concentration peak has varied of 1.16% for $[Ca^{2+}]_{pre}$ and 1.15% for $[Ca^{2+}]_{post}$, from 1Hz to 10 Hz (see Table 6.4). It is also considered that the concentration peaks must be close to the ones that Graupner et al. obtained for 1 and 10Hz. The parameter fitting was performed by **essays and trials**.

Frequency [Hz]	$[Ca^{2+}]_{pre}$ [−]	$[Ca^{2+}]_{post}$ [−]
1	0.84410	1.62138
10	0.85382	1.64002

Table 6.4 − Concentration peak values obtained by Graupner et al. (2016) at 1 and 10Hz.

Results

The combination of parameter values that were found with this method is given in Table 6.5. One can observe that the value of $\tau_{Ca,NMDA}$ is lower than what is found in the literature since Evans et al. (2012) reported that the time decay constant for the calcium through NMDARs was $25ms$. For the time constant $\tau_{Ca,ICaT}$, it is still consistent with what is found in the literature since the range of values changes between 10 and 100 ms, depending on the paper. There is still no consensus in the literature about a unique value of the calcium time decay through T-type calcium channels.

Once the parameters were fixed, the curve describing the relationship $\Delta w(f)$ was drawn. It is presented in Figure 6.23. One can observe that this combination of parameter values still did not give the same curves as Graupner et al. (2016) obtained based on experimental data (Sjöström et al., 2001). Indeed, the curves are still "inverted": the curve corresponding to $\Delta t = 10ms$ should encounter no changes at low frequencies while the curve corresponding to $\Delta t = -10ms$ should encounter depression at low frequencies.

Issues

The incorrect shape of the $\Delta w(f)$ curves is due to the fact that the parameters fitting was performed on only two frequency values. For other frequencies than 1 and 10 Hz, the concentration peak values were not the same as Graupner et al. (2016).

Parameter	Units	Value
$\tau_{Ca,NMDA}$	ms	19
$\zeta_{Ca,NMDA}$		0.27
$\tau_{Ca,ICaT}$	ms	40.75
$\zeta_{Ca,ICaT}$		0.329467
p_1		10
p_2		1

Table 6.5 – Values of the parameters from the physiological model (with $MgB(V) = 1$) obtained by fitting Graupner et al. concentration peaks variation between 1Hz and 10Hz. The parameters values were determined by visual inspection of the calcium concentration evolution. The fact that the same variation of frequency gives the same concentration peak variation as Graupner et al. (2016) was also verified.
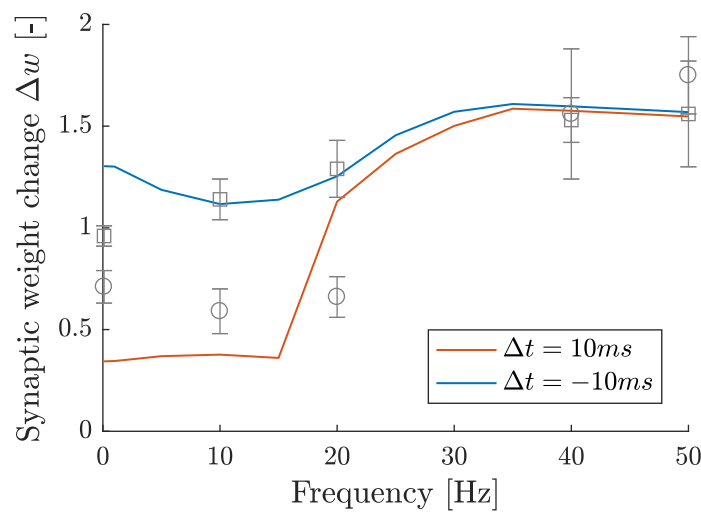
Figure 6.23 – **Experiment 3.** Curves $\Delta w(f) = w/w_0$ obtained by fitting the parameter values of the physiological models at two frequency values: 1 and 10 Hz. Δt is the time lag between the pre- and post-synaptic spikes. The experimental data from Sjöström et al. (2001) is represented in grey (square: $\Delta t = 10ms$, circle: $\Delta t = -10ms$).

Solution

A better approach would thus be to find the combination of parameters that fit the overall calcium concentration peak variation for all frequency values. This is done in the next experiment.

To summarize: Experiment 3: *fitting parameters on $[Ca^{2+}]$ peak values @ 1Hz and 10Hz*

➤ Assumption: Mg^{2+} not taken into account

➤ Issue: Δw(f) curve not consistent with experimental data from Sjöström et al. (2001)

➤ Why? Overfitting of the parameters on $[Ca^{2+}]$ peak values @ 1Hz and 10Hz

    ➡ *Solution?* Find the parameters of the physiological model for 11 frequency values

6.3.4 Experiment 4: Fitting on the concentration peak values for all frequencies

Assumption

The Mg^{2+} blockade is neglected.

Protocol followed to find the parameter values of the physiological calcium model

The idea is to try to find the parameters that fit at best the concentration peak values from Graupner et al. model for 11 frequency values. Indeed, it is better to have small errors on all frequencies than having no error on two frequency values and large errors on the remaining ones. The frequency values and the corresponding Ca^{2+} peak values from Graupner et al. (2016) are reported in Table 6.6. The parameters research is performed based on those 11 concentration peaks from Graupner et al. model.

Frequency [Hz]	$[Ca^{2+}]_{pre}$ peak value [−]	$[Ca^{2+}]_{post}$ peak value [−]
1	0.84410	1.62138
5	0.84420	1.62158
10	0.85382	1.64002
15	0.88932	1.70837
20	0.94608	1.81634
25	1.01443	1.94888
30	1.09321	2.09957
35	1.17284	2.25590
40	1.26213	2.42136
45	1.34724	2.58845
50	1.43212	2.75253

Table 6.6 − Values of the concentrations peak values from Graupner et al. (2016) for different frequencies.
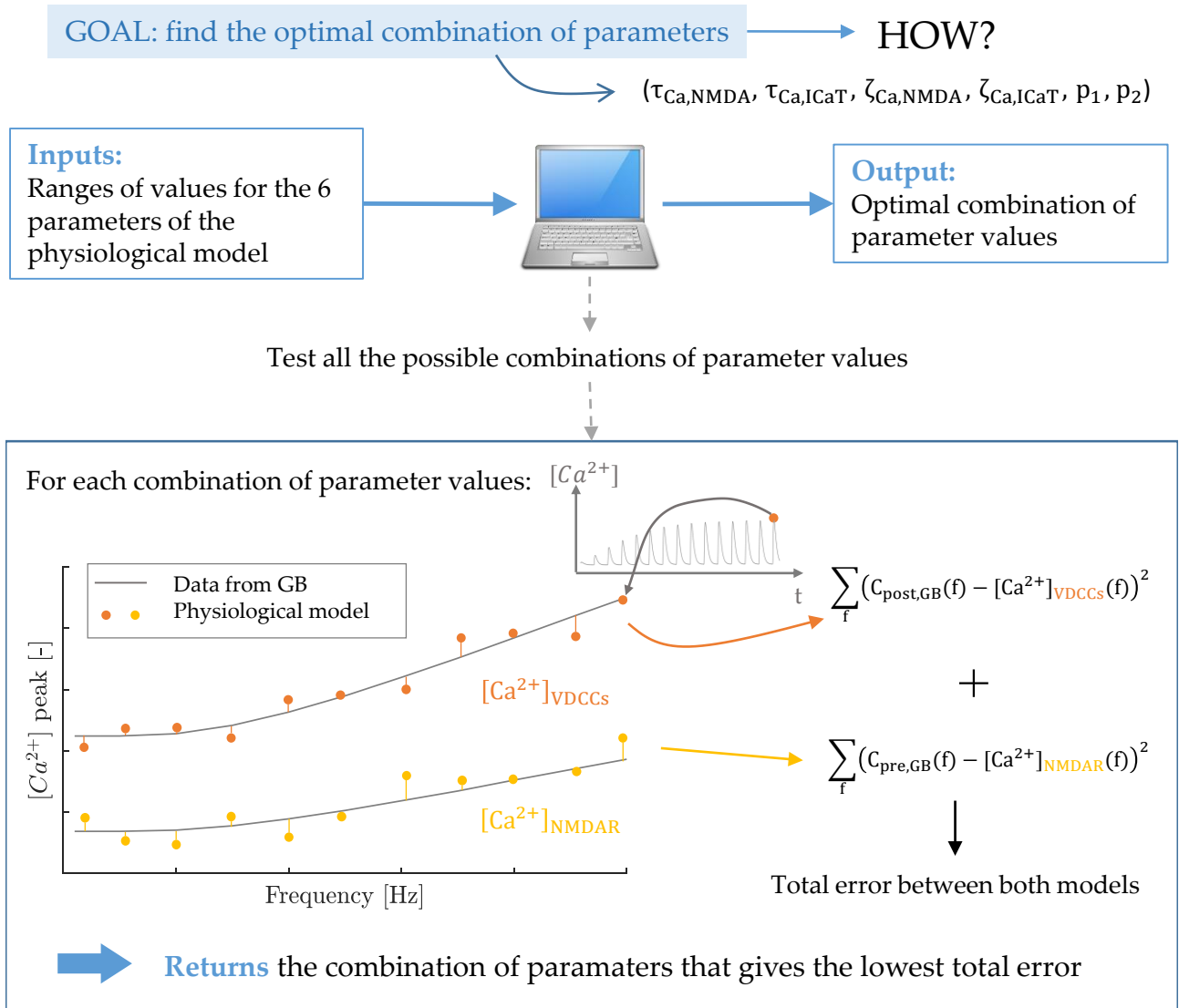
To get the optimal combination of parameter values, an **algorithm** was implemented. The principle of this algorithm is shown in Figure 6.24. It consists in testing all the possible parameter combinations, each parameter being in a given range of values, (see Table 6.7). The ranges of the time constants $\tau_{Ca,NMDA}$ and $\tau_{Ca,ICaT}$ were chosen to stay consistent to what is found in the literature (Kuo et al. (2011), Rossier (2016), Perez-Reyes (2003), Evans et al. (2012)).

Parameter	Unit	Range of values
$\tau_{Ca,NMDA}$	ms	$[15; 40]$
$\zeta_{Ca,NMDA}$		$[0.01; 5]$
$\tau_{Ca,ICaT}$	ms	$[10; 100]$
$\zeta_{Ca,ICaT}$		$[0.01; 1]$
p_1		$[0; 10]$
p_2		$[0; 2]$

Table 6.7 − Range of values of the parameters involved in the equations of the calcium transients for the physiological model. The Mg^{2+} blockades are still considered removed ($MgB(V) = 1$).

For each possible combination of parameter values, the square error was computed for each frequency value in order to get the total square error over all frequencies. The considered frequency values are in a range between 1 and 50Hz (see the first column of Table 6.6). Moreover, the algorithm was performed for both $\Delta t = 10ms$ and $\Delta t = -10ms$ and the errors were summed to get the parameter values that are suited for both curves.

The algorithm returns the optimal combination of parameters, *i.e.* the one that gives the lowest total square error between the Ca^{2+} concentration peak values from Graupner et al. model and the physiological model.

Figure 6.24 – Computational methodology to find the optimal combination of parameter values. The algorithm receives the range of values for each of the 6 parameters from the physiological model. It tests all the possible combination of parameter values. For each one of them, the total error between concentration peak value from Graupner et al. (2016) and the concentration peak computed with the given combination of parameter values. The algorithm returns the optimal combination of parameter values, *i.e.* the one that gives the lowest total error between the concentration peak values from Graupner et al. model and the physiological model.

Results

The best combination of parameter values obtained by implementing this algorithm is presented in Table 6.8. This combination gave a total square error of ≈ 0.00023 for the Ca^{2+} transient induced by the pre-synaptic spike and ≈ 0.01089 for the one induced by the post-synaptic spike. The values of the time constants $\tau_{Ca,NMDA}$ and $\tau_{Ca,ICaT}$ stay consistent with what is found in the literature.

Once the parameters were found, the curves $\Delta w(f)$ were drawn for $\Delta t = 10ms$ and $\Delta t = -10ms$. Those are presented in Figure 6.25. It is possible to observe that the curve corresponding to $\Delta t = 10ms$ is almost correct regarding experimental data from Sjöström et al. (2001). Indeed, it shows no changes in the synaptic weight for low frequencies (except for 0.1 and 5Hz) and then it increases as the frequency increases. However, the curve corresponding to $\Delta = -10ms$ is still incorrect because it shows potentiation ($\Delta w > 1$) at low frequencies whereas Sjöström et al. observed depression.

Parameter	Units	Value
$\tau_{Ca,NMDA}$	ms	20
$\zeta_{Ca,NMDA}$		0.275
$\tau_{Ca,ICaT}$	ms	36.45
$\zeta_{Ca,ICaT}$		0.3078
p_1		3.5
p_2		0.25

Table 6.8 – Values of the parameters from the physiological model (with $MgB(V) = 1$) obtained by fitting the concentration peak values from Graupner et al. (2016) for both $\Delta t = 10ms$ and $\Delta t = -10ms$. The Ca^{2+} concentration peak values correspond to the frequencies between 1 and 50 Hz.
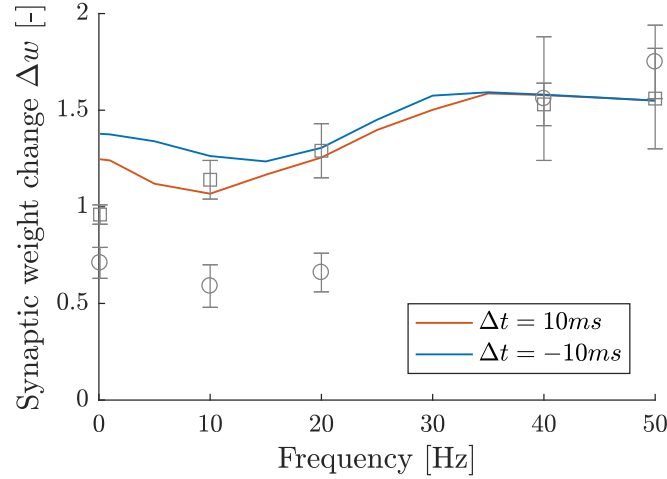
Figure 6.25 – **Experiment 4.** Curves $\Delta w(f) = w/w_0$ obtained by fitting the parameter values of the physiological models at 11 different frequency values. Δt is the time lag between the pre- and post-synaptic spikes. The experimental data from Sjöström et al. (2001) is represented in grey (square: $\Delta t = 10ms$, circle: $\Delta t = -10ms$).

Issues

The fact that there is potentiation instead of depression for a post-pre stimulation at low frequencies is actually due to the fact that the physiological equations describe a calcium dynamics which is too low.

Indeed, as can be observed in Figure 6.26, for $\Delta t = -10ms$, since the time constants found to fit the variation of concentration for all frequencies are too large, the dynamics is too slow. In consequence, the calcium concentration induced by the post-synaptic spike has not had the time to decrease yet that the calcium transient induced by the pre-synaptic spike is added to the total concentration (Figure 6.26.B). This results in the exceeding of the potentiation threshold.

Solution

Because of this low calcium dynamics, the next step is to try to find the time constant values that are more suitable with the calcium dynamics curves from Graupner et al. (2016), shown in Figure 6.26.A. However, the physiological aspect is taken into account since the time constants are decreased.

Note

After this experiment, another way to find the parameter values describing the Ca^{2+} concentration evolution from the physiological model was tried. Instead of computing the error based on the concentration values from Graupner et al. (2016), it is more convenient to try to find the parameters regarding experimental data from Sjöström et al. (2001). This way, the algorithm is adapted in the following
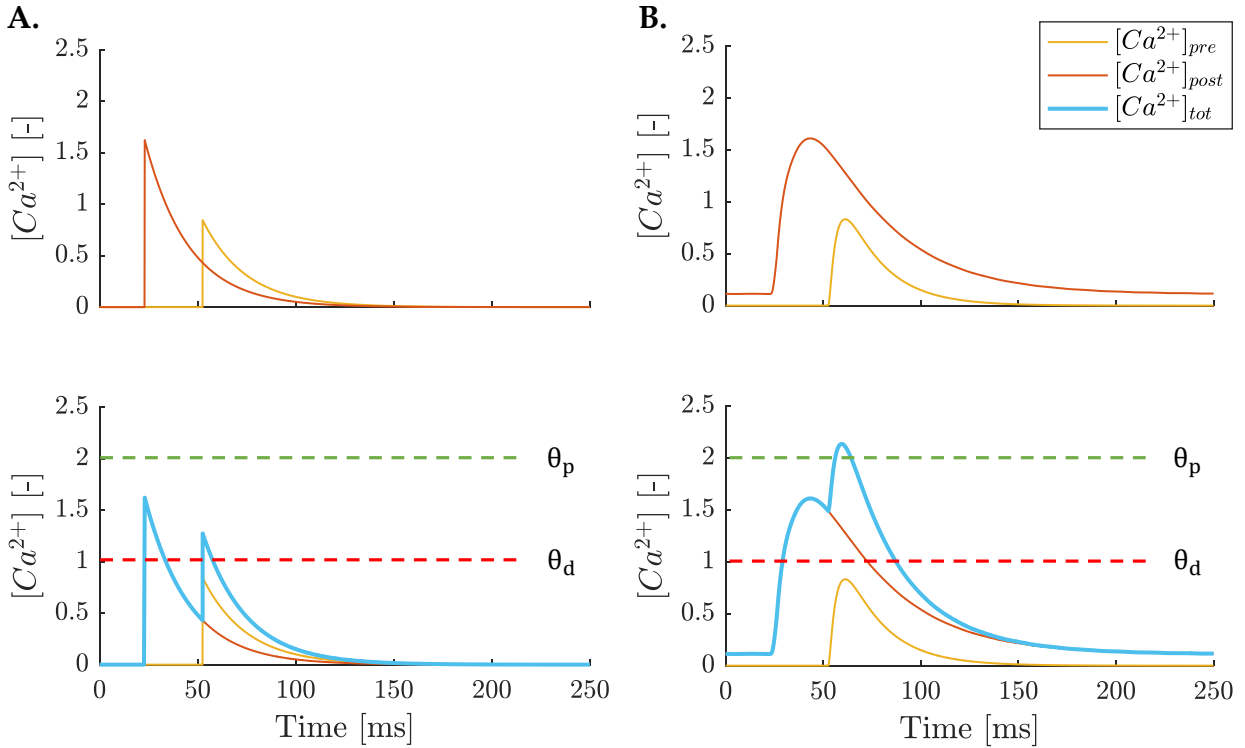
Figure 6.26 – Comparison of the calcium transients temporal evolution for the model from Graupner et al. (2016) (**A**) and the physiological model (**B**). The two top graphs show the individual calcium transients induced by the pre- and post-synaptic spikes, with $\Delta t = -10ms$. The two bottom graphs highlight the total calcium transient. The potentiation and depression thresholds are drawn in dotted lines. The physiological model parameters were determined by fitting 11 concentration values for 11 different frequency values and for both $\Delta t = \pm 10ms$.

To summarize: Experiment 4: *fitting parameters on $[Ca^{2+}]$ peak values on 11 frequency values $\in [1; 50]$ Hz and $\Delta t = \pm 10$ ms*

➢ Assumption: Mg^{2+} not taken into account

➢ Issue: $\Delta w(f)$ curve not consistent with experimental data from Sjöström et al. (2001)

  ➢ $\Delta t = 10ms \rightarrow \pm$ ok
  ➢ $\Delta t = -10ms \rightarrow$ ok for $f \gg$ but potentiation for $f \ll$

➢ Why? Physiological time constants too high $\rightarrow [Ca^{2+}]$ dynamics too slow
  $\rightarrow$ Depression threshold easily exceeded

➡ *Solution?* Reduce the time constants

---

way: for each combination of parameter values, the $\Delta w(f)$ curves are drawn for $\Delta t = \pm 10ms$. The square error is computed between the experimental data from Sjöström et al. (2001) and the $\Delta w(f)$ curve obtained for the given parameters combination. The best combination would thus be the one that gives the lowest total square error, just as for **Experiment 4**.

However, the execution time of this algorithm is huge and unfortunately, no results could be obtained. Indeed, there are 6 parameters to tune in the physiological calcium model: $\tau_{Ca,NMDA}$, $\tau_{Ca,ICaT}$, $\zeta_{Ca,NMDA}$, $\zeta_{Ca,ICaT}$, p_1 and p_2. Assuming that one wants to test 10 values for each one of them, this gives 10^6 combinations to test in total. For each combination, there are two $\Delta w(f)$ curves to compute, one for $\Delta t = 10ms$ and one for $\Delta t = -10ms$. It takes ~ 5 minutes to get those curves. It is thus not possible to implement this algorithm in the context of this thesis.

6.3.5 Experiment 5: Fitting on the calcium dynamics extracted from Graupner et al. (2016)

To resolve the issue of the slow calcium dynamics, the idea is to find the parameters of the physiological calcium-based model that fit more accurately the calcium dynamics from Graupner et al. (2016).

Protocol followed to find the parameter values of the physiological calcium model

The parameters have been chosen by **visual inspection** to find the best curve shape with respect to the Ca^{2+} concentration curve shape from Graupner et al. model.

Firstly, the individual curves of the calcium transients induced by both the pre- and post-synaptic spikes have been investigated (see Figure 6.27.A). The increasing phase of the calcium transients is slower with the physiological model because it takes into account additional physiological processes, such as the NMDARs and VDCCs activation. Graupner et al. did not consider this, their calcium transients are just described by an exponential. Moreover, for both pre- and post-synaptic spikes, the Ca^{2+} transients are characterized by the same time constant τ_{Ca} (see eq. (5.3) and (5.4)). To counteract this slower increase, the time constants from the physiological model have been changed and decreased in order to obtain roughly the same Ca^{2+} transient curves as Graupner et al..
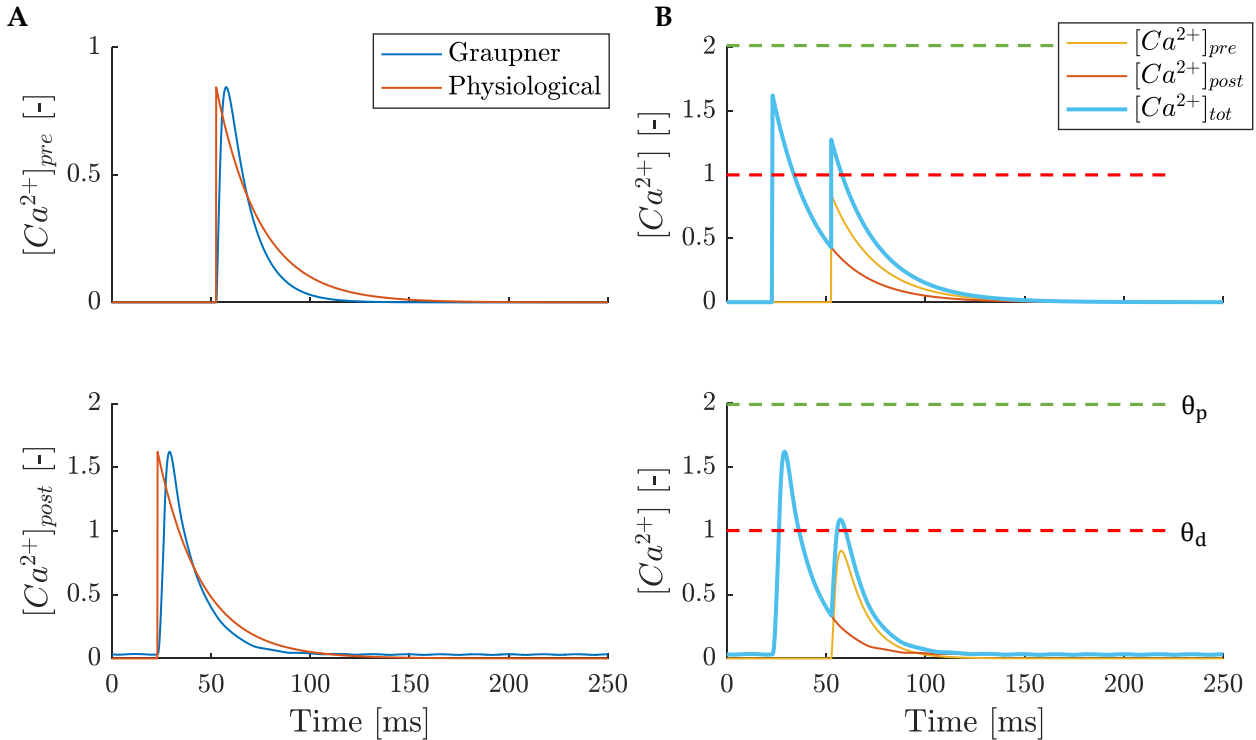
Figure 6.27 – Comparison between the physiological model and the one from Graupner et al. (2016). **A.** Comparison of the calcium transients induced by the pre- (top) and post-synaptic spikes (bottom) for the model from Graupner et al. (2016) and the physiological model. **B.** Comparison of the total Ca^{2+} concentration from Graupner et al. model (top) and the physiological one (bottom). The potentiation threshold θ_p is represented by the green dotted line and the depression threshold θ_d by the red dotted line. The physiological model implements a calcium dynamics with time constants values that are lower than what is found in the literature to fit as much as possible the Ca^{2+} curves from Graupner et al. (2016).

Once the parameter values gave a good approximation of the curves from Graupner et al., they were tested with different frequency values to verify if the concentration peak values suited the ones from Graupner et al. (2016). They were also tested with different values of Δt to observe the total Ca^{2+} concentration evolution. For example, for $\Delta t = -20ms$ (Figure 6.27.B), one can observe that the potentiation threshold is not exceeded as it was previously.

Results

Globally, the total square error was fairly small (≈ 0.02 for C_{pre} and ≈ 0.1 for C_{post}). The parameters are presented in Figure 6.9. One can notice that the time constants $\tau_{Ca,NMDA}$ and $\tau_{Ca,ICaT}$ are very low compared to what can be found in the literature about experimental data (Evans et al. (2012), Perez-Reyes (2003), Kuo et al. (2011), Rossier (2016)).

Parameter	Unit	Value
$\tau_{Ca,ICaT}$	ms	3
$\zeta_{Ca,ICaT}$		0.08122
$\tau_{Ca,NMDA}$	ms	12
$\zeta_{Ca,NMDA}$		0.2465
p_1		6
p_2		0.25

Table 6.9 – Values of the parameters used in the equations describing the physiological calcium concentration evolution, considering that all the Mg^{2+} blockade are removed. The parameters have been determined to fit as much as possible the calcium concentration from Graupner et al. (2016).

The curves $\Delta w(f)$ computed from the parameter values given in Table 6.9 are presented in Figure 6.28. One can see that the curves almost suit the ones that Graupner et al. obtained. However, regarding the experimental data from Sjöström et al. (2001), the curve corresponding to $\Delta t = -10ms$ does not fit the experimental data at frequency values of 10 and 20 Hz. Moreover, still at low frequencies, the pre-post stimulation is supposed to induce no changes and here there is potentiation.
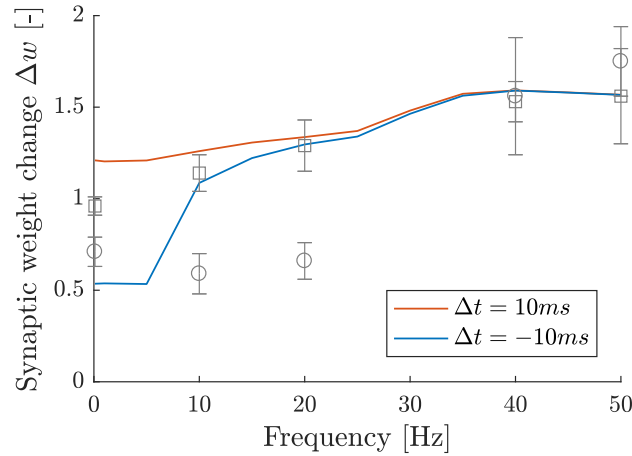
Figure 6.28 – Experiment 5. Curves $\Delta w(f) = w/w_0$ drawn with the parameters obtained by fitting the calcium transients from Graupner et al. (2016). Δt is the time lag between the pre- and post-synaptic spikes. The experimental data from Sjöström et al. (2001) is represented in grey (square: $\Delta t = 10ms$, circle: $\Delta t = -10ms$).

Issue

The main issue with this experiment is the fact that the time constant values are not consistent with experimental data (Perez-Reyes (2003), Kuo et al. (2011), Evans et al. (2012)).

However, it is still the only experiment that could give $\Delta w(f)$ curves that suit more or less experimental data from Sjöström et al. (2001).

To summarize:

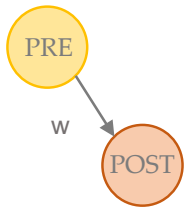➤ Assumptions: - Mg^{2+} not taken into account
                      - Time constants $\tau \ll$

➤ Result: Δw(f) curve $\pm$ correct

➤ Issue: Time constant values not consistent with experimental data

 Model not really physiological anymore

6.4   Summary

Graupner and Brunel (GB) abstract calcium-based model

Physiological calcium-based model with $\dot{w}([Ca^{2+}])$
from Graupner's model

$\dot{C}_{pre}$ (GB) $\Rightarrow [\dot{Ca^{2+}}]_{NMDARs}$ (calcium through NMDARs)

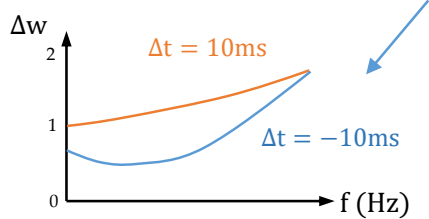$\longrightarrow \dot{C}_{pre} = f(C_{pre}, I_{Ca,NMDA})$

$f\left(s_{NMDA}(V_{pre}), V_{post}, MgB(V_{post})\right)$

$\dot{C}_{post}$ (GB) $\Rightarrow [\dot{Ca^{2+}}]_{ICaT}$ (calcium through VDCCs)

$\longrightarrow \dot{C}_{post} = f\left(C_{post}, ICaT(V_{post})\right)$
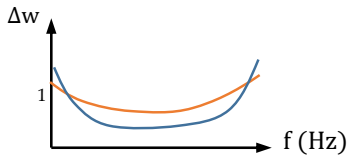
$f\left(s_{NMDA}(V_{pre}), V_{post}, MgB(V_{post})\right)$

PRE

w

POST

GOAL: Reproduce the $\Delta w(f)$ curves from GB with the physiological model

$\Delta t = 10ms$

$\Delta t = -10ms$

$\longrightarrow$ Based on experimental data from Sjöström (2001)

Starting point   Experiment 1: directly from physiological equations

$\longrightarrow$ Does not work because of the Mg^{2+} blockade dynamics

Conclusion?

Mg^{2+} influence on V_{pre}/V_{post} not considered by Graupner

Mg^{2+} blockade dynamics neglected

Experiment 2	Experiment 3	Experiment 4	Experiment 5
~~Mg^{2+}~~	~~Mg^{2+}~~	~~Mg^{2+}~~	~~Mg^{2+}~~, $\tau \ll$
Fitting parameters on $[Ca^{2+}]$ peak values at 1Hz	Fitting parameters on $[Ca^{2+}]$ peak values at 1, 10Hz	Fitting parameters on $[Ca^{2+}]$ peak values at 11 frequency values and $\Delta t = \pm 10ms$	Fitting parameters on $[Ca^{2+}]$ peak values at 1 Hz and $\neq \Delta t$ values
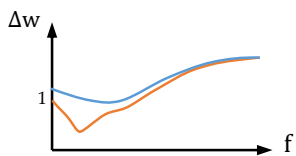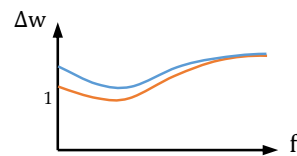
Overfitting on the frequencies values on which the parameters were fitted

$\tau_{Ca,NMDA}, \tau_{Ca,ICaT}$ must be $\ll$ (but not physiological)
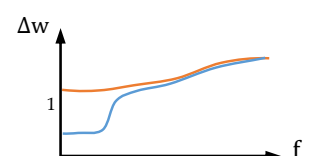
$\Delta w(f)$: $\pm ok$
But model not really physiological anymore...

$\Longrightarrow$ Too much approximations with Graupner's calcium-based model

Part III

Conclusion and perspectives

Chapter 7

Conclusion and perspectives

7.1 Summary

This thesis is dedicated to the implementation of calcium-induced synaptic plasticity models. For now, the majority of calcium-based synaptic plasticity models do not consider the calcium dynamics in detail. A lot of simplifications have been made in order to reproduce experimental data. However, when it is desired to introduce a more detailed calcium dynamics into an existing plasticity model, this can be very difficult to do.

In this thesis, it is indeed shown that trying to introduce equations describing the calcium dynamics in a more detailed way can lead to issues linked to the simplification of the model.

Part I sets the theoretical notions that are necessary to understand the modeling of calcium-induced synaptic plasticity. It first puts in mind the basic concepts about the neuron and its electrical modeling. Then, since synaptic plasticity has a great role in memory encoding and consolidation, especially during sleep, the basics of sleep are introduced. Finally, the most important chapter of this part concerns synaptic plasticity, in particular the role of calcium in its induction. The parallelism between synaptic plasticity and its computational modeling is also established.

Part II is devoted to the implementation of calcium-based synaptic plasticity models. Five models are described in details: Graupner et al. (2016), Shouval et al. (2002), Standage et al. (2014), Honnuraiah and Narayanan (2013) and Olcese et al. (2010). Those models are compared in Table 5.2. All of them have implemented their calcium-dependent synaptic weight rule as a function of the calcium concentration in the post-synaptic neuron. Except for Graupner et al. (2016), who also considered the VDCCs as a source of Ca^{2+}, they all consider that the source of Ca^{2+} is the NMDARs. The level of simplification of the calcium dynamics is quite variable. For example, Honnuraiah and Narayanan (2013) considered a detailed modeling of the NMDARs that characterizes the flow of Ca^{2+} but also Na^+ and K^+ ions through them. In contrast, Graupner et al. (2016) has made a very simple and abstractive modeling of the calcium dynamics but they fitted their parameters on experimental data.

Then, the calcium-based plasticity model from Graupner et al. (2016) is integrated into the conductance-based model from Drion et al. (2018). This allows using physiological values of the membrane potential instead of just having a fixed train of spiking events, as Graupner et al. (2016) implemented. Moreover, using the conductance-based model allows switching from a tonic mode to a bursting mode to observe the consequences of this switch on the calcium concentration. The results from Graupner et al. (2016) were successfully obtained.

Finally, the calcium-based synaptic plasticity rule from Graupner et al. (2016) is adapted in order to integrate the equations of a detailed calcium dynamics. However, this thesis shows that Graupner et al. have made a great number of assumptions, such as the influence of the Mg^{2+} blockade on both the pre- and post-synaptic membrane potential. Moreover, their simplified equations describing a sum of exponential functions do not take into account the physiological phenomena leading to the flow of Ca^{2+} ions into the post-synaptic neuron.

The main contribution of this thesis is thus to show that starting from an abstract model, in which the calcium dynamics has been greatly simplified, and then integrating equations of a detailed calcium dynamics is very challenging. Indeed, the final result presented in this thesis almost succeeds in reproducing experimental data based on the parameter values that Graupner et al. determined to describe their calcium-dependent plasticity rule. However, to achieve this result, the Mg^{2+} blockade impact on the pre- and post-synaptic potential has been omitted. The ranges of time constant values to describe the calcium concentration evolution have also been considerably decreased to obtain results similar to what Graupner et al. (2016) got. The time constant values do not correspond anymore to what can be found in the literature for experimental data.

7.2 Prospects

Improving the physiological calcium-based synaptic plasticity model

The next step would be to investigate the detailed physiological calcium-based synaptic plasticity models.

It would be more appropriate to start from equations describing a detailed calcium dynamics, *e.g.* the ones that have been described in Section 6.2. Then, it would be relevant to adapt the parameters from the equations describing synaptic weight evolution, *e.g.* from Graupner et al. model (*i.e.* τ_{cb}, θ_p, θ_d, γ_p, γ_d, see eq. (5.1)). Indeed, it would be more convenient to adapt the potentiation/depression thresholds that determine the synaptic weight changes while keeping the range of physiological Ca^{2+} concentration values from the physiological model. The parameter values would be suited on experimental data, just as Graupner et al. (2016) did by reproducing the protocol from Sjöström et al. (2001). The calcium-dependent synaptic plasticity rule does not necessarily need to follow the one from Graupner et al., one can decide to use another rule. For example, the $\dot{w}([Ca])$ rule from Shouval et al. (2002) (see eq. (5.10)) can be followed and the parameters describing the functions $\tau([Ca])$ and $\Omega([Ca])$ would be adapted according to physiological Ca^{2+} concentration.

Investigation of the link between sleep and calcium-induced synaptic plasticity

It would be interesting to explore how the switch from the awake to the asleep state affects those calcium-induced synaptic weight changes between neurons. Indeed, the role of calcium has been proven in the implication of the ability of (thalamic) neurons to switch from a tonic firing pattern to a bursting mode. This intrinsic neuronal ability is due to the presence of VDCCs on the membrane of the neuron. Moreover, experiments on rodents show that calcium concentration in neocortical dendrites is increased during oscillations of sleep spindles. Calcium concentration oscillations are also synchronized with the oscillations of the spindles (Seibt et al. (2017), Niethard et al. (2018)).

Massimini and Amzica (2001) also showed that the oscillations encountered during the slow-wave sleep are accompanied with extracellular $[Ca^{2+}]$ fluctuations up to $\sim 20\%$ the basal values. Those fluctuations impact directly the neurotransmitter release from the pre-synaptic neuron.

Integrating a calcium-based dynamics into the conductance-based model allows observing the effects of this tonic-bursting modes switch on calcium-induced synaptic plasticity. It would thus be even more interesting if the calcium-based model has been changed in order to consider the different biophysical pathways induced by Ca^{2+} that trigger synaptic plasticity.
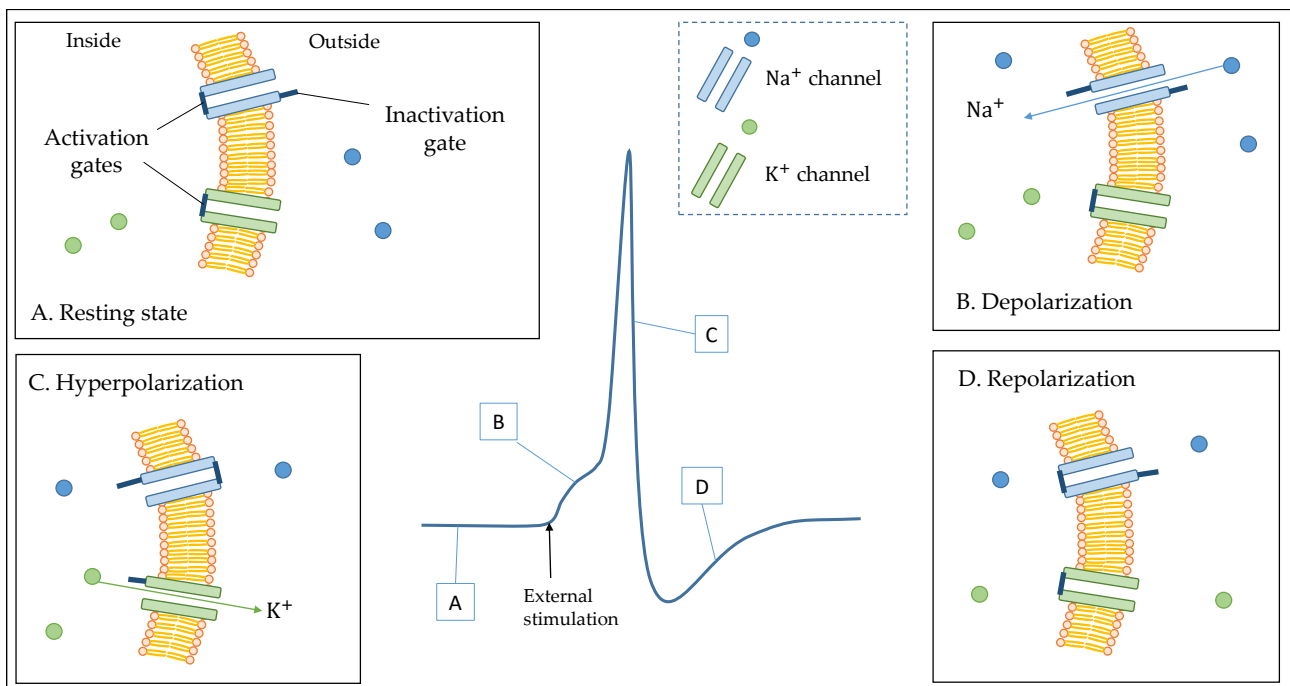
Appendices

Appendix A

Supplementary theoretical information

A.1 Action potential generation

Figure A.1 – Generation of an action potential. **A.** At rest, the membrane potential V_m is equal to $\simeq -70$ mV and the activation gates of both sodium Na^+ and potassium K^+ ions are closed while the inactivation gate of the sodium is open. The membrane is impermeable at this stage. **B.** The neuron is excited by a stimulus, it is depolarized. This depolarization induces the rapid opening of the Na^+ activation gate while the other gates do not move because they have slower kinetics. This allows the flow of Na^+ ions into the neuron, which depolarizes the neuron even more, until $V_m \simeq 40$ mV. **C.** After a few hundreds of milliseconds, the sodium inactivation gate starts to close while the potassium activation gate starts to open. This is due to the high level of depolarization of the membrane. The Na^+ ions do not enter inside the cell anymore but the K^+ ions start to flow outside the cell, which hyperpolarizes progressively the membrane potential, until $V_m \simeq -90$ mV. **D.** The hyperpolarization of the cell membrane triggers the closing of the K^+ activation gate but also the closing of the Na^+ activation gate while the Na^+ inactivation gate opens. The membrane recovers its permeability and its resting potential. Adapted from (Drion, 2013).

A.2   Equilibrium ionic concentrations

Ion	[ion]$_{\text{in}}$ [mM]	[ion]$_{\text{out}}$ [mM]	Reversal potential [mV]
Na$^+$	18	145	56
K$^+$	135	3	-102
Cl$^-$	7	120	-76
Ca^{2+}	10^{-4}	1.2	125

Table A.1 − Equilibrium ionic intracellular and extracellular concentrations and the corresponding reversal potentials of those ions (computed from eq. (2.1)). Data from (Geris and Dauby, 2019)

A.3   Supplementary information to Hodgkin-Huxley (HH) model

To express the conductances depending on V_m and the time, they considered that a given ionic channel has 2 states: an open state (O) and a closed state (C), as can be seen in eq. (A.1), where $\alpha(V_m)$ and $\beta(V_m)$ are the reaction constants to go from one state to the other.

$$C \underset{\beta(V_m)}{\overset{\alpha(V_m)}{\rightleftharpoons}} O \tag{A.1}$$

In other words, the ionic channels can be seen as gates that open and close to regulate the opening of the channels.

Hodgkin and Huxley considered that, for each ion, the maximum value of the conductance $\bar{g}_{ion}$ is attained only if all the channels are open. This way, the value $\bar{g}_{ion}$ is defined by the density of channels on the membrane and is considered constant for a given neuron.

The fraction of open channels is defined by $n(V_m, t)$ and we have that $g_{ion} = \bar{g}_{ion} n(V_m, t)$. The variation of $n(V_m, t)$ per unit of time can be defined by (law of mass action):

$$\dot{n}(V_m, t) = \alpha(V_m)(1 - n(V_m, t)) - \beta(V_m) n(V_m, t)$$
$$= -(\alpha(V_m) + \beta(V_m))\left(n(V_m, t) - \frac{\alpha(V_m)}{(\alpha(V_m) + \beta(V_m))}\right) \tag{A.2}$$

Defining $\tau(V_m) = \frac{1}{\alpha(V_m) + \beta(V_m)}$ the constant of activation/inactivation of the ionic channels, and $n_\infty(V_m) = \frac{\alpha(V_m)}{\alpha(V_m) + \beta(V_m)}$ the equilibrium fraction of open channels for a given V_m, eq. (A.2 becomes:

$$\dot{n}(V_m, t) = \frac{-(n(V_m, t) - n_\infty(V_m))}{\tau(V_m)} \tag{A.3}$$

In the particular case of the giant quid axon, Hodgkin and Huxley described the potassium and sodium conductances by the following equations:

$$g_{Na}(V_m, t) = \bar{g}_{Na} m(V_m, t)^3 h(V_m, t)$$
$$g_k(V_m, t) = \bar{g}_K n(V_m, t)^4 \tag{A.4}$$

Where $m(V_m, t)$ and $h(V_m, t)$ are the sodium activation and inactivation variables for the sodium and $n(V_m, t)$ is the activation variable of the potassium. During the membrane depolarization, $m(V_m, t)$ is activated while $h(V_m, t)$ is inactivated.

A.4 T-type calcium channel: how does it work?

The T-type calcium current is due to a calcium channel that has an activation gate and an inactivation gate. On the one hand, the activation gate opens when there is a depolarization and closes when there is a hyperpolarization. On the other hand, the inactivation gate opens when the cell is hyperpolarized and closes when there is a depolarization. The dynamics is different for both gates: the activation gate opens and closes much more rapidly than the inactivation gate. This difference in the gates dynamics allows the entry of Ca^{2+} ions inside the neuron after a depolarization, as explained in Figure A.2. This Ca^{2+} entry allows to exceed the excitability threshold on the neuron and thus the generation of action potentials when the neuron is excited (with the participation of K^+ and Na^+ ions): the neuron is bursting.
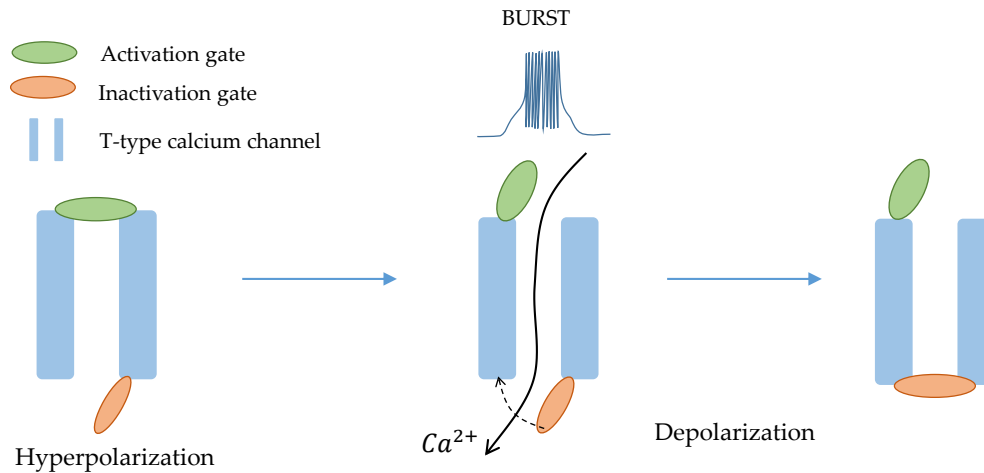
Figure A.2 – T-type calcium channel: activation and inactivation gate. When the neuron is hyper-polarized, the inactivation gate is open but the activation gate is closed. When the neuron becomes depolarized, the activation gates rapidly opens while the inactivation gate slowly closes. During the time the inactivation gate closes (about 100 ms), the Ca^{2+} ions can enter into the neuron. This entry of Ca^{2+} ions allows the cell to reach the excitability threshold and thus allows the generation of a burst of action potentials when the neuron is excited (due to K^+ and Na^+ ions). Adapted from (Brain's explained)

There exists another current, a hyperpolarized-activated cation channel, abbreviated I_h. When the thalamo-cortical neurons are hyperpolarized, it slowly activates a mixed Na^+ and K^+ current that depolarizes the neuron.

Figure A.3.B shows the successions of I_T and I_h currents for a thalamo-cortical neuron. When the neuron is hyperpolarized, I_h is activated, which increases the membrane potential higher than -65 mV. This depolarization activates I_T. When the low-threshold calcium current I_T is activated, Ca^{2+} ions can enter inside the neuron, which depolarizes the neuron. This depolarization allows the generation of a burst of action potentials (with Na^+ and K^+ ions) until the T-type channel is completely closed ($\sim$ 100 ms) so the membrane potential goes back to its resting potential and there are no action potentials anymore. Since there is no Na^+/K^+ current anymore, the membrane potential continues to decrease and the neuron becomes hyperpolarized, which activates I_h. The cycle begins again.
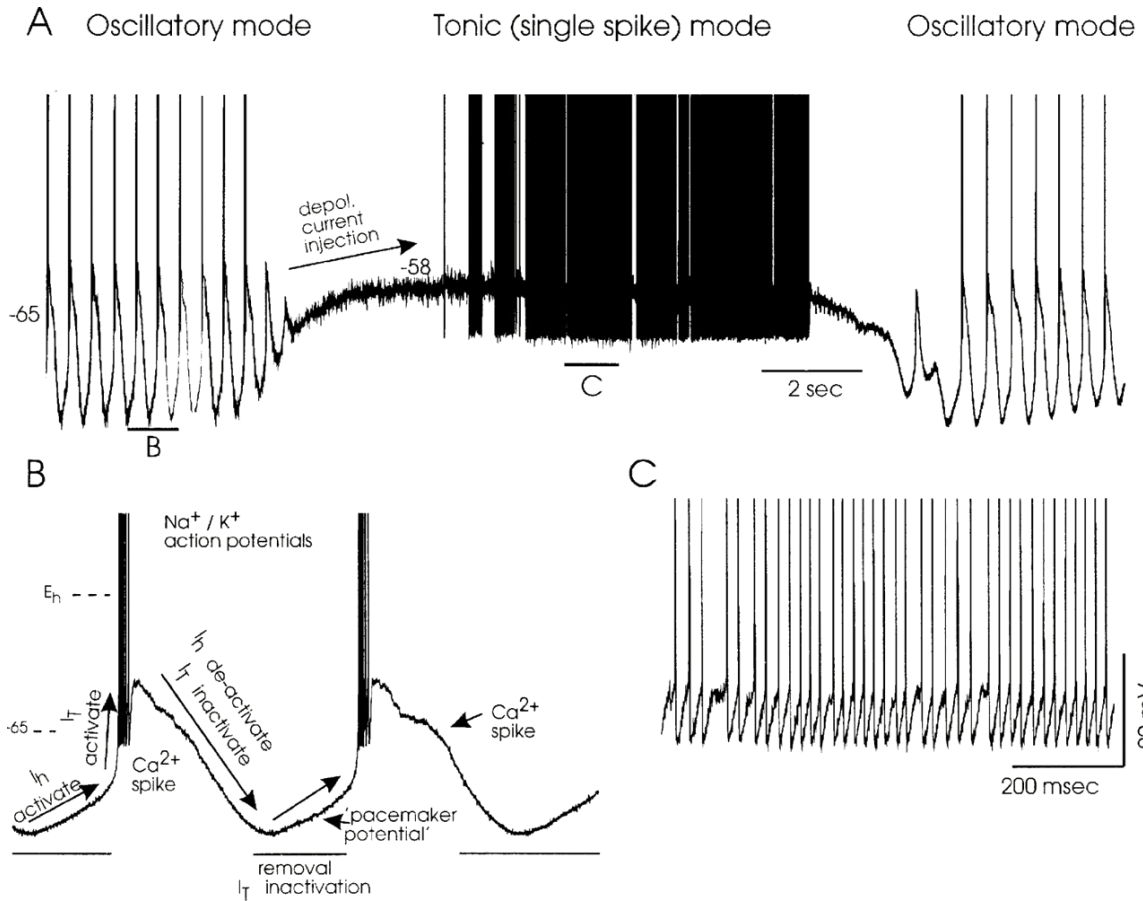
Figure A.3 – Thalamocortical neurons generate two distinct patterns of action potentials via the interaction of ionic currents.(McCormick and Bal, 1997) **A.** A cat dorsal lateral geniculate neuron (LGNd) generated rhythmic burst firing at a rate of about 2 Hz. The intracellular depolarization injection of a current led to a depolarization of the neuron ($V_m = -58$ mV). This depolarization led to the switch from the bursting mode to a tonic mode (*i.e.* single spike mode) due to the T-type calcium channel closing. Removal of the depolarization current lead to the retrieval of the bursting mode. **B.** Zoom on the oscillatory mode trace and the currents involved in the generation of action potentials in a bursting mode. **C.** Zoom on the tonic mode trace.

Appendix B

Modeling synaptic plasticity: supplementary information

B.1 Drion et al. (2018) model

In this model, the equation describing the membrane potential evolution is the following:

$$C_m \dot{V}_m = -I_{Na} - I_K - I_{CaT} - I_{K,Ca} - I_H - I_{\text{leak}} + I_{app} \tag{B.1}$$

Just as for the HH model, using Ohm's law for each ionic current leads to the following equation that describes the Drion et al. model:

$$\begin{aligned} C_m \dot{V}_m = &- \bar{g}_{Na} m_{Na}^3 h_{Na} \left(V_m - V_{Na}\right) - \bar{g}_{K,D} m_{K,D}^4 \left(V_m - V_K\right) - \bar{g}_{Ca,T} m_{Ca,T}^3 h_{Ca,T} \left(V_m - V_{Ca}\right) \\ &- \bar{g}_{K,Ca} m_{K,Ca\infty}([Ca]) \left(V_m - V_K\right) - \bar{g}_H m_H \left(V_m - V_H\right) - \bar{g}_{\text{leak}} \left(V_m - V_{\text{leak}}\right) + I_{app} \end{aligned} \tag{B.2}$$

The units of the different quantities appearing in eq. (B.2) are the following:

- Potentials: $[mV]$;
- Conductances: $[mS/cm^2]$;
- Currents: $[A/cm^2]$;
- Capacitances: $[\mu F/cm^2]$;
- Time: $[s]$.

In this model, the different parameter values are: $C = 1$, $V_{Na} = 50$, $V_K = -85$, $V_{Ca} = 120$, $V_l = -55$, $V_H = -20$, $g_l = 0.055$, $g_{Na} = 120$, $g_{Kd} = 30$, $K_d = 170$.

The gating variables describing the kinetics of the ionic currents are defined by the two following expressions:

$$m_{X,\infty} \text{ (or } h_{X,\infty}) = \frac{1}{1 + \exp((V + A)/B)} \tag{B.3}$$

$$\tau_X = A - \frac{B}{1 + \exp((V + D)/E)} \tag{B.4}$$

The different parameters appearing in equations (B.3) and (B.3) are presented in Table B.1.

This model considers that the neurons are connected via AMPA, $GABA_A$ and $GABA_B$ connections. The equations describing those connections

$$I_{AMPA} = \bar{g}_{AMPA} AMPA(V - 0) \tag{B.5}$$

$$I_{GABA,A} = \bar{g}_{GABA,A} GABAA (V - V_{Cl}) \tag{B.6}$$

Param.	A	B	Param.	A	B	D	E
$m_{Na,\infty}$	35.5	-5.29	$\tau_{m_{Na}}$	1.32	1.26	120.	-25.
$h_{Na,\infty}$	48.9	5.18	$\tau_{h_{Na}}$	$(0.67/(1{+}\exp((V{+}62.9)/{-}10.0)))*(1.5 + 1/(1{+}\exp((V{+}34.9)/3.6)))$			
$m_{Kd_{\infty}}$	12.3	-11.8	$\tau_{m_{Kd}}$	0.2	6.4	28.3	-19.2
$m_{CaT,\infty}$	67.1	-7.2	$\tau_{m_{CaT}}$	21.7	21.3	68.1	-20.5
$h_{CaT,\infty}$	80.1	5.5	$\tau_{h_{CaT}}$	410.	179.6	55.	-16.9
$m_{H,\infty}$	80.	6.	τ_{m_H}	272.	-1149	42.2	-8.73

Table B.1 – Parameter values used in the conductance-based model from Drion et al. (2018).

$$I_{GABA,B} = \bar{g}_{GABA,B} GABAB \left(V - V_K\right), \tag{B.7}$$

Where $AMPA$, $GABAA$ and $GABAB$ are variables that depend on the pre-synaptic membrane potential V_{pre} in the following way:

$$\dot{AMPA} = 1.1 T_m \left(V_{\text{pre}}\right)\left[1 - AMPA\right] - 0.19 AMPA \tag{B.8}$$

$$\dot{GABAA} = 0.53 T_m \left(V_{pre}\right)\left[1 - GABAA\right] - 0.19 GABAA \tag{B.9}$$

$$\dot{GABAB} = 0.016 T_m \left(V_{pre}\right)\left[1 - GABAB\right] - 0.0047 GABAB \tag{B.10}$$

Where $Tm(V_{pre})$ is an activation function described by:

$$Tm(V_{pre}) = \frac{1}{1 + exp\left(-\frac{V_{pre}-2}{5}\right)} \tag{B.11}$$

Bibliography

Arun Anirudhan and X Rishikesh Narayanan. Analogous Synaptic Plasticity Profiles Emerge from Disparate Channel Combinations. 35(11):4691–4705, 2015. doi: 10.1523/JNEUROSCI.4223-14.2015.

Simone Astori, Ralf D. Wimmer, and Anita Lüthi. Manipulating sleep spindles - expanding views on sleep, memory, and disease. *Trends in Neurosciences*, 36(12):738–748, 2013. ISSN 01662236. doi: 10.1016/j.tins.2013.10.001.

Maxim Bazhenov, Igor Timofeev, Mircea Steriade, and Terrence J Sejnowski. Model of thalamocortical slow-wave sleep oscillations and transitions to activated states. *Journal of neuroscience*, 22(19):8691–8704, 2002.

Paradiso Michael Bear Mark, Connors Barry. *Neuroscience: Exploring the brain, Third edition*. January 2007.

Jennifer Berry. What are neurotransmitters? https://www.medicalnewstoday.com/articles/326649, October 2019. [Accessed: 2021-05-14].

Aren J. Borgdorff and Daniel Choquet. Regulation of AMPA receptor lateral movements. *Nature*, 417 (6889):649–653, 2002. ISSN 00280836. doi: 10.1038/nature00780.

Joseph M Brader, Walter Senn, and Stefano Fusi. Learning real-world stimuli in a neural network with spike-driven synaptic dynamics. *Neural computation*, 19(11):2881–2912, 2007.

Brain's explained. The thalamus. https://www.youtube.com/watch?v=fki7AmLma_I&t=309s. [Accessed: 2021-04-23].

Paudel Hemant Zhu Hong-Jian Cheng Heung-Chin, Qi Robert Z. Regulation and function of protein kinases and phosphatases. *Enzyme Research*, 2011, 12 2011. doi: 10.4061/2011/794089.

Claudia Clopath. *Long Term Plasticity, Biophysical Models*, pages 1628–1640. Springer New York, 2015. doi: 10.1007/978-1-4614-6675-8_351.

Kathleen Coutisse. Sensitivity and robustness analysis of thalamic neuron models at the cellular and network levels. Master's thesis, University of Liège, 2018.

Alain Destexhe, Thierry Bal, David A McCormick, and Terrence J Sejnowski. Ionic mechanisms underlying synchronized oscillations and propagating waves in a model of ferret thalamic slices. *Journal of neurophysiology*, 76(3):2049–2070, 1996.

Guillaume Drion. *Regulation of Excitability, Pacemaking, and Bursting : Insights from Dopamine Neuron Electrophysiology*. PhD thesis, University of Liège, 2013.

Guillaume Drion, Julie Dethier, Alessio Franci, and Rodolphe Sepulchre. Switchable slow cellular conductances determine robustness and tunability of network states. *PLoS computational biology*, 14(4):e1006125, 2018.

Steve K Esser, Sean L Hill, and Giulio Tononi. Sleep homeostasis and cortical synchronization: I. modeling the effects of synaptic strength on sleep slow waves. *Sleep*, 30(12):1617–1630, 2007.

Rebekah C. Evans, Teresa Morera-Herreras, Yihui Cui, Kai Du, Tom Sheehan, Jeanette Hellgren Ko-taleski, Laurent Venance, and Kim T. Blackwell. The effects of nmda subunit composition on calcium influx and spike timing-dependent plasticity in striatal medium spiny neurons. *PLOS Computational Biology*, 8(4):1–13, 04 2012. doi: 10.1371/journal.pcbi.1002493.

Joana S. Ferreira, Thomas Papouin, Laurent Ladépêche, Andrea Yao, Valentin C. Langlais, Delphine Bouchet, Jérôme Dulong, Jean Pierre Mothet, Silvia Sacchi, Loredano Pollegioni, Pierre Paoletti, Stéphane Henri Richard Oliet, and Laurent Groc. Co-agonists differentially tune GluN2B-NMDA receptor trafficking at hippocampal synapses. *eLife*, 6:1–22, 2017. ISSN 2050084X. doi: 10.7554/eLife.25492.

Ilya A Fleidervish, A Friedman, and MJ Gutnick. Slow inactivation of na+ current and slow cumulative spike adaptation in mouse and guinea-pig neocortical neurones in slices. *The Journal of physiology*, 493(1):83–97, 1996.

Silvana Franceschetti, Ezia Guatteo, Ferruccio Panzica, Giulio Sancini, Enzo Wanke, and Giuliano Avanzini. Ionic mechanisms underlying burst firing in pyramidal neurons: intracellular study in rat sensorimotor cortex. *Brain Research*, 696(1):127–139, 1995. ISSN 0006-8993. doi: https://doi.org/10.1016/0006-8993(95)00807-3.

Liesbet Geris and Pierre Dauby. Modélisation des systèmes biologiques (lecture notes). University of Liège, Spring 2019.

Karl Peter Giese, Nikolai B Fedorov, Robert K Filipkowski, and Alcino J Silva. Autophosphorylation at thr286 of the α calcium-calmodulin kinase ii in ltp and learning. *Science*, 279(5352):870–873, 1998.

Daiane CF Golbert, Annie C Souza, Daniel G Almeida-Filho, and Sidarta Ribeiro. Sleep, synaptic plasticity, and memory. *Reference Module in Neuroscience and Biobehavioral Psychology*, 2017. doi: 10.1016/B978-0-12-809324-5.21118-8.

Michael Graupner. Synaptic plasticity : Spike-timing dependent plasticity (stdp). CNRS UMR 8003, Université de Paris, 9 2020. Saints-Pères Paris Institute for the Neurosciences, Université de Paris. URL https://biomedicale.u-paris.fr/~mgraupe/teaching.php.

Michael Graupner and Nicolas Brunel. STDP in a bistable synapse model based on CaMKII and associated signaling pathways. *PLoS Computational Biology*, 3(11):2299–2323, 2007. ISSN 1553734X. doi: 10.1371/journal.pcbi.0030221.

Michael Graupner and Nicolas Brunel. Calcium-based plasticity model explains sensitivity of synaptic changes to spike pattern, rate, and dendritic location. *Proceedings of the National Academy of Sciences of the United States of America*, 109(10):3991–3996, 2012. ISSN 10916490. doi: 10.1073/pnas.1109359109.

Michael Graupner, Pascal Wallisch, and Srdjan Ostojic. Natural firing patterns imply low sensitivity of synaptic plasticity to spike timing compared with firing rate. *Journal of Neuroscience*, 36(44):11238–11258, 2016. ISSN 15292401. doi: 10.1523/JNEUROSCI.0104-16.2016.

Ruth Heidelberger, Harel Shouval, Robert S. Zucker, and John H. Byrne. Synaptic Plasticity. *From Molecules to Networks: An Introduction to Cellular and Molecular Neuroscience: Third Edition*, pages 533–561, 2014. doi: 10.1016/B978-0-12-397179-1.00018-X.

Thomas D Helton, Weifeng Xu, and Diane Lipscombe. Neuronal l-type calcium channels open quickly and are inhibited slowly. *Journal of Neuroscience*, 25(44):10247–10251, 2005.

Sean Hill and Giulio Tononi. Modeling sleep and wakefulness in the thalamocortical system. *Journal of neurophysiology*, 93(3):1671–1698, 2005.

Suraj Honnuraiah and Rishikesh Narayanan. A calcium-dependent plasticity rule for hcn channels maintains activity homeostasis and stable synaptic learning. *PloS one*, 8(2), 2013.

Afsaneh Khetrapal. What is neuromodulation? https://www.news-medical.net/health/What-is-Neuromodulation.aspx, May 2021. [Accessed: 2021-05-22].

Ivana Y-T Kuo, Stephanie E Wölfle, and Caryl E Hill. T-type calcium channels and vascular function: the new kid on the block? *The Journal of physiology*, 589(4):783–795, 2011.

Sakmann B. Larkum ME, Zhu JJ. Dendritic mechanisms underlying the coupling of the dendritic with the axonal action potential initiation zone of adult rat layer 5 pyramidal neurons. *J Physiol*, 533: 447–466, 2001. doi: 10.1111/j.1469-7793.2001.0447a.x.

Nathalie Leresche and Régis C Lambert. T-type calcium channels in synaptic plasticity. *Channels*, 11 (2):121–139, 2017.

Diane Lipscombe, Thomas D Helton, and Weifeng Xu. L-type calcium channels: the low down. *Journal of neurophysiology*, 92(5):2633–2641, 2004.

Jie Luo, Trongha X. Phan, Yimei Yang, Michael G. Garelick, and Daniel R. Storm. Increases in cAMP, MAPK activity, and CREB phosphorylation during REM sleep: Implications for REM sleep and memory consolidation. *Journal of Neuroscience*, 33(15):6460–6468, 2013. ISSN 02706474. doi: 10.1523/JNEUROSCI.5018-12.2013.

Jeffrey C. Magee and Daniel Johnston. A synaptically controlled, associative signal for hebbian plasticity in hippocampal neurons. *Science*, 275(5297):209–213, 1997. ISSN 0036-8075. doi: 10.1126/science.275.5297.209.

Malinow R. Makino H. Ampa receptor incorporation into synapses during ltp: the role of lateral movement and exocytosis. *Neuron*, 64(3):381–390, 2009. doi: 10.1016/j.neuron.2009.08.035.

Marcello Massimini and Florin Amzica. Extracellular calcium fluctuations and intracellular potentials in the cortex during the slow sleep oscillation. *Journal of neurophysiology*, 85(3):1346–1350, 2001.

David A. McCormick and Thierry Bal. Sleep and arousal: Thalamocortical mechanisms. *Annual Review of Neuroscience*, 20(September 2014):185–215, 1997. ISSN 0147006X. doi: 10.1146/annurev.neuro.20.1.185.

Niels Niethard, Hong-Viet V Ngo, Ingrid Ehrlich, and Jan Born. Cortical circuit activity underlying sleep slow oscillations and spindles. *Proceedings of the National Academy of Sciences*, 115(39): E9220–E9229, 2018.

Umberto Olcese, Steve K. Esser, and Giulio Tononi. Sleep and synaptic renormalization: A computational study. *Journal of Neurophysiology*, 104(6):3476–3493, 2010. ISSN 00223077. doi: 10.1152/jn.00593.2010.

Edward Perez-Reyes. Molecular physiology of low-voltage-activated t-type calcium channels. *Physiological reviews*, 83(1):117–161, 2003.

Amiel Rosenkranz, Andreas Frick, and Daniel Johnston. Kinase-dependent modification of dendritic excitability after long-term potentiation. *The Journal of physiology*, 587(1):115–125, 2009.

Michel Rossier. T-type calcium channel: A privileged gate for calcium entry and control of adrenal steroidogenesis. *Frontiers in Endocrinology*, 7:43, 2016. ISSN 1664-2392. doi: 10.3389/fendo.2016.00043.

Julie Seibt, Clément J. Richard, Johanna Sigl-Glöckner, Naoya Takahashi, David I. Kaplan, Guy Doron, Denis De Limoges, Christina Bocklisch, and Matthew E. Larkum. Cortical dendritic activity correlates with spindle-rich oscillations during sleep in rodents. *Nature Communications*, 8(1):1–12, 2017. ISSN 20411723. doi: 10.1038/s41467-017-00735-w.

Gordana Sendic. Thalamic nuclei. https://www.kenhub.com/en/library/anatomy/thalamic-nuclei, 2021. [Accessed: 2021-04-22].

Harel Z. Shouval, Mark F. Bear, and Leon N. Cooper. A unified model of NMDA receptor-dependent bidirectional synaptic plasticity. *Proceedings of the National Academy of Sciences of the United States of America*, 99(16):10831–10836, 2002. ISSN 00278424. doi: 10.1073/pnas.152343099.

Blais BS Yeung LC Cooper LN Shouval HZ, Castellani GC. Converging evidence for a simplified biophysical model of synaptic plasticity. *Biol Cybern.*, 87((5-6)):383–91., Dec 2002. doi: 10.1007/s00422-002-0362-x.

David Goodsell Shuchismita Dutta. Calmodulin. August 2003. URL https://pdb101.rcsb.org/. [Accessed: 2021-05-11].

Per Jesper Sjöström, Gina G Turrigiano, and Sacha B Nelson. Rate, timing, and cooperativity jointly determine cortical synaptic plasticity. *Neuron*, 32(6):1149–1164, 2001. ISSN 0896-6273. doi: 10.1016/S0896-6273(01)00542-6.

Dominic Standage, Sajiya Jalil, and Thomas Trappenberg. Computational consequences of experimentally derived spike-time and weight dependent plasticity rules. *Biological cybernetics*, 96(6):615–623, 2007.

Dominic Standage, Thomas Trappenberg, and Gunnar Blohm. Calcium-Dependent Calcium Decay Explains STDP in a Dynamic Model of Hippocampal Synapses. 9(1), 2014. doi: 10.1371/journal.pone.0086248.

Mircea Steriade, David A. McCormick, and Terrence J. Sejnowski. Thalamocortical oscillations in the sleeping and aroused brain. *Science*, 262(5134):679–685, 1993. ISSN 00368075. doi: 10.1126/science.8235588.

David J Triggle. L-type calcium channels. *Current pharmaceutical design*, 12(4):443–457, 2006.

Gilles Vandewalle and Pierre Leprince. Introduction aux neurosciences cognitives (lecture notes). University of Liège, Spring 2019.

Yina Wei, Giri P Krishnan, and Maxim Bazhenov. Synaptic mechanisms of memory consolidation during sleep slow oscillations. *Journal of Neuroscience*, 36(15):4231–4247, 2016.

Atsushi Yamadori. Role of the spindles in the onset of sleep. *Kobe J Med Sci*, 17(3):97–111, 1971.

Luk Chong Yeung, Harel Z. Shouval, Brian S. Blais, and Leon N. Cooper. Synaptic homeostasis and input selectivity follow from a calcium-dependent plasticity model. *Proceedings of the National Academy of Sciences of the United States of America*, 101(41):14943–14948, 2004. ISSN 00278424. doi: 10.1073/pnas.0405555101.